IOWA STATE UNIVERSITY
Digital Repository

Retrospective Theses and Dissertations

Iowa State University Capstones, Theses and Dissertations

1985

A hybrid Patterson-superposition/direct-method approach to the X-ray phase problem, and in-lab EXAFS techniques

Sue-Lein Wang Lii
Iowa State University

Follow this and additional works at: https://lib.dr.iastate.edu/rtd

Part of the Physical Chemistry Commons

Recommended Citation

Lii, Sue-Lein Wang, "A hybrid Patterson-superposition/direct-method approach to the X-ray phase problem, and in-lab EXAFS techniques " (1985). *Retrospective Theses and Dissertations*. 8720.
https://lib.dr.iastate.edu/rtd/8720

This Dissertation is brought to you for free and open access by the Iowa State University Capstones, Theses and Dissertations at Iowa State University Digital Repository. It has been accepted for inclusion in Retrospective Theses and Dissertations by an authorized administrator of Iowa State University Digital Repository. For more information, please contact digirep@iastate.edu.

المنارة للاستشارات

www.manaraa.com

INFORMATION TO USERS

This reproduction was made from a copy of a manuscript sent to us for publication and microfilming. While the most advanced technology has been used to photograph and reproduce this manuscript, the quality of the reproduction is heavily dependent upon the quality of the material submitted. Pages in any manuscript may have indistinct print. In all cases the best available copy has been filmed.

The following explanation of techniques is provided to help clarify notations which may appear on this reproduction.

1. Manuscripts may not always be complete. When it is not possible to obtain missing pages, a note appears to indicate this.
2. When copyrighted materials are removed from the manuscript, a note appears to indicate this.
3. Oversize materials (maps, drawings, and charts) are photographed by sectioning the original, beginning at the upper left hand corner and continuing from left to right in equal sections with small overlaps. Each oversize page is also filmed as one exposure and is available, for an additional charge, as a standard 35mm slide or in black and white paper format.*
4. Most photographs reproduce acceptably on positive microfilm or microfiche but lack clarity on xerographic copies made from the microfilm. For an additional charge, all photographs are available in black and white standard 35mm slide format.*

***For more information about black and white slides or enlarged paper reproductions, please contact the Dissertations Customer Services Department.**

UMI University Microfilms International

8604490

Lii, Sue-Lein Wang

A HYBRID PATTERSON-SUPERPOSITION/DIRECT-METHOD APPROACH TO THE X-RAY PHASE PROBLEM, AND IN-LAB EXAFS TECHNIQUES

Iowa State University PH.D. 1985

University
Microfilms
International 300 N. Zeeb Road, Ann Arbor, MI 48106

PLEASE NOTE:

In all cases this material has been filmed in the best possible way from the available copy. Problems encountered with this document have been identified here with a check mark __✓__.

1. Glossy photographs or pages _____
2. Colored illustrations, paper or print _____
3. Photographs with dark background _____
4. Illustrations are poor copy _____
5. Pages with black marks, not original copy _____
6. Print shows through as there is text on both sides of page _____
7. Indistinct, broken or small print on several pages __✓__
8. Print exceeds margin requirements _____
9. Tightly bound copy with print lost in spine _____
10. Computer printout pages with indistinct print _____
11. Page(s) _____ lacking when material received, and not available from school or author.
12. Page(s) _____ seem to be missing in numbering only as text follows.
13. Two pages numbered _____. Text follows.
14. Curling and wrinkled pages _____
15. Dissertation contains pages with print at a slant, filmed as received _____
16. Other _____

University
Microfilms
International

A hybrid Patterson-superposition/direct-method approach to the X-ray phase problem, and in-lab EXAFS techniques

by

Sue-Lein Wang Lii

A Dissertation Submitted to the
Graduate Faculty in Partial Fulfillment of the
Requirements for the Degree of
DOCTOR OF PHILOSOPHY

Department: Chemistry
Major: Physical Chemistry

Approved:

Signature was redacted for privacy.

In Charge of Major Work

Signature was redacted for privacy.

For the Major Department

Signature was redacted for privacy.

For the Graduate College

Iowa State University
Ames, Iowa
1985

TABLE OF CONTENTS

IN-LAB EXAFS TECHNIQUES

GENERAL INTRODUCTION

Two X-ray methods, the single-crystal X-ray diffraction and the extended X-ray absorption fine-structure method, are studied in this thesis. The former method has long been a unique tool for the determination of crystal structures, while the latter method just became a powerful tool to determine the arrangement of atoms in any form of condensed matter in the last decade.

In X-ray diffraction, the crystal structure can be determined from a knowledge of the intensities and phases of the diffraction spectra. But only the intensities can be found experimentally. The absence of phase information has constituted the so-called "phase problem". This problem is usually tackled by two approaches. The first is Patterson manipulation methods. In this method, information about atomic positions can be obtained by translating the distribution of interatomic vectors in the Patterson function. From the early 1930s to the late 1960s, most crystal structures were solved using this approach. The second approach is that of direct methods. In these methods, phases are derived directly from structure-factor amplitudes. This approach has become prevailing and served an important role in the crystal structure analysis since 1970s.

Both approaches have advantages over each other. But, in general, neither of them is capable of solving all kinds of structures. Thus, in this research, a hybrid approach which combines advantages of the above two approaches has been developed and presented in the first part of this thesis. The validity of a new relation, the Σ_2-like relation, which is a result of our hybrid theory, will be investigated thoroughly. Theoretical developments of phase relationships among structure factors E and G (obtained from the Fourier transform of Patterson superposition functions) will also be studied. Finally, applications of this hybrid approach to four real structure solutions, both previously known and unknown, are presented and discussed in detail.

EXAFS techniques are quite new. Since the EXAFS phenomenon is usually weak (0.1-10% of the total absorption), a signal-to-noise ratio over 100 is usually required to obtained useful structural information. This requires the use of high X-ray fluxes and thus sophisticated detection systems.

In the second part of this thesis, EXAFS techniques which utilize a rotating anode X-ray source are presented. A general description of the EXAFS theory as well as considerations for EXAFS experimentation are given in the first two chapters. All the work which has been done with our in-lab EXAFS facility will be presented. This includes the spectrometer alignment, automation, improvement of spectrometer's energy resolution, and the investigation of the performance of the current detection systems.

SECTION A

A HYBRID PATTERSON-SUPERPOSITION/DIRECT METHOD APPROACH TO THE X-RAY PHASE PROBLEM

CHAPTER 1. INTRODUCTION

Among various methods proposed for analyzing vector distributions on the Patterson functions,[1] Patterson superposition (otherwise known as image-seeking or vector coincidence), suggested by Wrinch[2] in 1939, is the most logical and the one permitting systematic development. Much of such systematic development of image-seeking has taken place in the hands of Buerger[3] and it was he who turned this method into a convenient tool for crystal structure determination. To locate the coincident peaks on superimposed Patterson maps (displaced relative to each other) Buerger has proposed special image-seeking functions, maxima of which correspond to the possible atomic positions in the structure. The most effective is the minimum function

$$M_n(\vec{r}) = \min\{P(\vec{r}-\vec{r}_1);\ P(\vec{r}-\vec{r}_2);\ldots P(\vec{r}-\vec{r}_n)\}. \qquad (1.1)$$

The successful practical application of this method has been demonstrated by many analyses.[4,5,6]

The Patterson superposition method[7] is well-known by its easy start without exact knowledge of chemical composition or space group symmetry. However, this method has not become as popular and routinely used in crystal structure determination as direct methods which evolved from the Harker-Kasper inequalities[8] and has become the major method of phase problem solution beginning in the 1970s. The main reason which restricts the use of Patterson superposition methods lies in the difficulty of interpreting the results when multiple images appear together and some additional (false) maxima exist. It often requires considerable knowledge and effort to untangle these problems.

Many authors have tried to improve the use of this method. For example, Germain and Woolfson[9] suggested a procedure for deconvoluting the Patterson function by constructing $M_2(\vec{r})$ using an arbitrary Patterson vector. Depending on the multiplicity of the peak used, several structure images, displaced relative to each other, will be present in the function. Utilizing the fact that the Patterson superposition function gives a corresponding approximation to the Fourier coefficients of the electron distribution:

$$G_{\vec{h}}' = q \int M_n(\vec{r}) \exp[2\pi i \vec{h}.\vec{r}] dv, \qquad (1.2)$$

one may then take the Fourier coefficients for $M_2(\vec{r})$, raise them to the second power and calculate a new Patterson function
using $|G_{\vec{h}}'|^2$. In this new Patterson function the most powerful peaks will correspond to the vectors connecting different displaced structure images on $M_2(\vec{r})$. Simonov[10] adopted another approach. He has studied possible methods of automatic search for the displacement vectors necessary for the construction of the minimum function and suggested a superpositional synthesis procedure. Like Germain he also

calculated $G_{\vec{h}}'$. However, instead of using the value of $|G_{\vec{h}}'|$, the phases of $G_{\vec{h}}$ were assigned to the $|F_{obs}|$ to obtain the first approximation of the electron density distribution. His method was the first one which demonstrated the expediency of using the Fourier integral of the superposition function to calculate the phases of structure factor amplitudes.

Direct methods[11] are characterized by procedures which search for triple-phase relationships from a given set of reflections and derive phases from the amplitude of these reflections on the basis of probability and symmetry. These methods are very effective for structures containing equal and randomly distributed atoms to which the Patterson function-based methods would sometimes encounter difficulties. The prevalence of the use of direct methods is attributable in large part to several well-developed program packages such as MULTAN,[12] SHELX,[13] and DIRDIF,[14] etc., which require little effort or special crystallographic knowledge to use. But these methods, like the Patterson methods, fail for some structures. The problems occur when space group symmetry is too low, a center of symmetry is lacking, cell composition information is incomplete, pseudo-symmetry or an oriented structure exists, or when only moderate intensity data sets are measured. In these cases, one may turn to an alternative, e.g., the Patterson-based techniques.

Since the 1960s, there have been a series of studies which have combined Patterson or Patterson superposition and direct methods together to solve crystal structures. Hauptman and Karle[15] have derived a formula expressing the values of the structure invariants in terms of the Patterson function. Wismer and Jacobson[16] have suggested a procedure in which a superposition map is constructed from a so-called Σ_2-map and a regular Patterson map. Then the Fourier transform of the map, with negative regions set equal to zero, yields reliable phases for the larger $|E|$ values. These were then extended and refined by usual direct methods techniques. Recently, Allegra[17] has also proposed a theory which derives three-phase invariants from the Patterson functions.

In this research, a method which combines both Patterson superposition and direct methods has been developed. The basic assumption inherent in this new method is that the product of the Patterson superposition function and the electron density still resembles the electron density. The convolution of the Fourier coefficients of the $M_n(\vec{r})$ function, G, with the structure factors will therefore give the structure factors, and this leads to a Σ_2-like equation of the form

$$E_{\vec{h}} = \kappa < E_{\vec{k}} G_{\vec{h}-\vec{k}} >_{\vec{k}}$$

in which the angle brackets represent averaging over the complete set of triple-phase relationships and κ is a so-called phase efficiency constant. This Σ_2-like relation has been proven to be effective for both centro- and noncentrosymmetric crystals. It possesses dual characteristics which allow phase refinement to be carried out on both the real and false part of the electron density-like function introduced by the use of $M_n(\vec{r})$.

In the following chapters, the theory of this new hybrid method is developed and this is followed by a complete study of the statistical properties of G (the Fourier coefficients for the Patterson superposition function $M_n(\vec{r})$). The statistical theory of the triple-phase relationships involving the pseudo-normalized structure factors G is developed in Chapter 4. Phase refinements which make use of both the Σ_2-like relation (or the modified tangent formula (2.30)) and Sayre's Σ_2 relation (or tangent formula (2.28)) are discussed in Chapter 5. Since the structure factors G are closely related to the quality of Patterson superposition functions, an additional chapter (Chapter 6) is devoted to the discussion of possible ways to construct better minimum functions.

Most of the theoretical developments mentioned above have been tested using either model or real structures. Testing procedures, results and discussions are given in Chapter 7. Application of the hybrid approach to real structure solutions has also been carried out and is also described in this chapter. Finally, there is a summary in which an algorithm of the new hybrid method is described.

CHAPTER 2. THEORY

Introduction

Relations between the magnitudes and phases of structure factors have been derived by Harker and Kasper,[18] Karle and Hauptman[19] and Goedkoop.[20] All are based on the fact that the electron density in crystals is everywhere positive, and is approximately a superposition of spherically symmetric atoms of the same shape. An equality relation between structure factors derived by Sayre[21] has the form:

$$N^{-1/2}E_{\vec{h}} = \langle E_{\vec{k}} E_{\vec{h}-\vec{k}} \rangle_{\vec{k}}, \qquad (2.1)$$

where the angle bracket represents the averaging over a complete set of $\vec{k}$, and is based on the fact that when a crystal contains equal atoms which are resolved from one another, the operation of squaring the electron density leaves it unchanged in the sense that it is still composed of equal atoms in the same positions as before.

The equality of (2.1) is strictly restricted to the assumption of atomic resolution and equality of the atoms. For the weaker resolution assumption, Hughes[22] gave the result

$$N^{-1/2}E_{\vec{h}} \sim \langle E_{\vec{k}} E_{\vec{h}-\vec{k}} \rangle_{\vec{k}} \qquad (2.2)$$

and Karle and Hauptman[23] showed that

$$\sigma_2^{-3/2}\sigma_3 E_{\vec{h}} \sim \langle E_{\vec{k}} E_{\vec{h}-\vec{k}} \rangle_{\vec{k}} \qquad (2.3)$$

even when the assumption of equal atoms has been dropped and atoms are not completely resolved. Expressions (2.1) to (2.3) are generally referred to as Sayre's equation.

In this chapter, similar relations to (2.2) and (2.3) in which $E_{\vec{h}-\vec{k}}$ is replaced by $G_{\vec{h}-\vec{k}}$ (the Fourier coefficient for $M_n(\vec{r})$) shall be derived.

Physical Basis

The basic assumption in our method is that the product of the Patterson superposition function with the electron density is approximately the square of the electron density, i.e.,

$$\rho^2 \sim M_{ps} \cdot \rho \qquad (2.4)$$

where ρ represents the electron density function of a correctly positioned structure, and $M_{ps} = M_n(\vec{r})$. In practice, the minimum function, M_{ps}, could be a map which is obtained from one superposition (i.e., n = 2 in (1.1)), has an atom at the origin and is in general a triclinic representation of the structure; alternately it could be a map which has been shifted so its origin corresponds to the origin of a higher symmetry system. Indeed M_{ps} could even be a 0/1 representation as obtained from a superposition procedure or other route and where 0's are placed where there are no atoms in electron density space and ones where atoms could be located. In this case an equation which is very similar to (2.4), namely

$$\rho \sim M_{ps} \cdot \rho \qquad (2.5)$$

would be obtained. Note that it would not be necessary to have a completely accurate description in that ones could also be located in regions where no atoms exist.

In either case therefore, from the convolution theorem, the Fourier coefficients of ρ, that is the structure factors, will be given by the convolution of the Fourier coefficients of M_{ps} and ρ, i.e.,

$$F_{\vec{h}} \sim \frac{1}{V} \Sigma_{\vec{k}} F_{\vec{k}} G'_{\vec{h}-\vec{k}} \qquad (2.6)$$

where the F's are the structure factors and the G's are the Fourier coefficients of the M_{ps} function as given in equation (1.2).

Notation

We denote by $\vec{r}_j$ the position vector of the jth atom and by Z_j the atomic number. The quasi-normalized structure factor $E_{\vec{h}}$ is defined by means of

$$E_{\vec{h}} = \frac{1}{{\sigma_2}^{1/2}} \sum_{j=1}^{N} Z_j \exp[2\pi i\vec{h}.\vec{r}_j] \qquad (2.7.1)$$

$$= |E_{\vec{h}}| \exp(i\alpha_{\vec{h}}) \qquad (2.7.2)$$

where

$$\sigma_n = \sum_{j=1}^{N} Z_j^n \qquad (2.8)$$

and N is the number of atoms in the unit cell. The general form of the structure factor $F_{\vec{h}}$ is

$$F_{\vec{h}} = \sum_{j=1}^{N} f_j \exp[2\pi i\vec{h}.\vec{r}_j]\exp[-B_j(\sin\theta/\lambda)^2] \qquad (2.9)$$

where f_j is the atomic scattering factor and $\exp[-B_j(\sin/\lambda)^2]$ is the temperature factor correction for the jth atom. It is evident from (2.7) that the phase $\alpha_{\vec{h}}$ of the quasi-normalized structure factor $E_{\vec{h}}$ is the same as that of the crystal structure factor $F_{\vec{h}}$. The structure factor $V_{\vec{h}}$ of a squared structure is defined by means of

$$V_{\vec{h}} = \sigma_1^{-2} \sum_{j=1}^{N} Z_j^2 \exp[2\pi i\vec{h}.\vec{r}_j]. \qquad (2.10)$$

The Fourier coefficient for M_{ps}, $G_{\vec{h}}$, which shall be referred as pseudo-normalized structure factor, is defined by means of

$$G_{\vec{h}} = \frac{1}{(\sigma_2')^{1/2}} \sum_{j=1}^{M} Z_j \exp[2\pi i\vec{h}.\vec{r}_j] \qquad (2.11.1)$$

$$= |G_{\vec{h}}|\exp(i\gamma_{\vec{h}}) \qquad (2.11.2)$$

where

$$\sigma_n' = \sum_{j=1}^{M} Z_j^n \, . \qquad (2.12)$$

and M is the number of atoms which appear on the superposition map. Note that $G_{\vec{h}}$ is a point approximation of M_{ps} and $G_{\vec{h}}'$ (see (1.2)) which shall be named "pseudo" structure factor in order to be distinguishable from the normalized ones. M in general is regarded as a number greater than N due to false maxima in M_{ps}.

Derivation of the Σ_2-Like Relation

An expression corresponding to (2.6) will now be derived in detail using simple mathematical operations and in terms of normalized structure factors. Let us assume that a Patterson map has been calculated using intensities sharpened in the usual fashion,[24] and one or more superpositions have been carried out. After application of the temperature sharpening and with an appropriate scaling, the Fourier coefficient of M_{ps}, $G_{\vec{h}}$, assuming the equal atom case, becomes

$$G_{\vec{h}} = M^{-1/2} \sum_{j=1}^{M} \exp[2\pi i\vec{h}.\vec{r}_j] \qquad (2.13)$$

where $M^{-1/2}$ replaces $Z\ (\sigma_2')^{-1/2}$ in (2.11.1). Similarly (2.7.1) becomes

$$E_{\vec{h}} = N^{-1/2} \sum_{j=1}^{N} \exp[2\pi i\vec{h}.\vec{r}_j]. \qquad (2.14)$$

Now let us consider the product

$$E_{\vec{k}}\,G_{\vec{h}-\vec{k}} = [N^{-1/2}\sum_{j=1}^{N}\exp(2\pi i\vec{k}.\vec{r}_j)].[M^{-1/2}\sum_{j=1}^{M}\exp\{2\pi i(\vec{h}-\vec{k}).\vec{r}_j\}]$$

$$= (NM)^{-1/2}[\sum_{j=1}^{N}\exp(2\pi i\vec{k}.\vec{r}_j)].[\sum_{j=1}^{N}\exp\{2\pi i(\vec{h}-\vec{k}).\vec{r}_j\}$$

$$+ \sum_{j=N+1}^{M}\exp\{2\pi i(\vec{h}-\vec{k}).\vec{r}_j\}] \qquad (2.15)$$

where the summations over j's are independent of one another. After multiplication and combination we obtain

$$E_{\vec{k}}G_{\vec{h}-\vec{k}} = (NM)^{-1/2}[\sum_{j=1}^{N}\exp(2\pi i\vec{h}.\vec{r}_j) + \sum_{\substack{j=1\\ j\neq j'}}^{N}\sum_{j'=1}^{M}\exp(2\pi i\vec{h}.\vec{r}_j)$$

$$.\ \exp\{2\pi i\vec{k}.(\vec{r}_j - \vec{r}_{j'})\}]. \qquad (2.16)$$

If we now take averages over $\vec{k}$, the term $\exp\{2\pi i\vec{k}.(\vec{r}_j - \vec{r}_{j'})\}$ will average zero, and we obtain

$$< E_{\vec{k}}\ G_{\vec{h}-\vec{k}} >_{\vec{k}} \sim (NM)^{-1/2}\sum_{j=1}^{N}\exp(2\pi i\vec{h}.\vec{r}_j). \qquad (2.17)$$

Alternately one can write

$$M^{-1/2}\ E_{\vec{h}} \sim < E_{\vec{k}}\ G_{\vec{h}-\vec{k}} >_{\vec{k}}. \qquad (2.18.1)$$

Expression (2.18.1) bears a strong resemblance to the sigma two relation (2.2). Here, however, we know the phases and magnitudes of the G's, and as usual wish to determine the phases of the E's, knowing their magnitudes.

If atoms are not equal, equation (2.17) becomes

$$E_{\vec{k}} G_{\vec{h}-\vec{k}} \sim (\sigma_2 \sigma_2')^{-1/2} \sum_{j=1}^{N} Z_j^2 \exp(2\pi i \vec{h}.\vec{r}_j).$$

By using the definition of $V_{\vec{h}}$, we obtain

$$\frac{\sigma_1^2}{(\sigma_2 \sigma_2')^{1/2}} V_{\vec{h}} \sim \langle E_{\vec{k}} G_{\vec{h}-\vec{k}} \rangle_{\vec{k}}. \qquad (2.19)$$

Before any use can be made of (2.19), it is necessary to consider the relation between $E_{\vec{h}}$ and $V_{\vec{h}}$. When the atoms are equal $V_{\vec{h}} = N^{-3/2} E_{\vec{h}}$; when they are unequal the two are still closely correlated. According to Cochran and Woolfson's work,[25] we find

$$V_{\vec{h}} \simeq \frac{\sigma_3}{\sigma_1^2 \sigma_2^{1/2}} E_{\vec{h}}. \qquad (2.20)$$

Thus (2.19) becomes

$$\frac{\sigma_3}{\sigma_2 (\sigma_2')^{1/2}} E_{\vec{h}} \sim \langle E_{\vec{k}} G_{\vec{h}-\vec{k}} \rangle_{\vec{k}} \qquad (2.18.2)$$

which resembles the sigma-two relation (2.3) for unequal-atom structures.

Can we expect the Σ_2-like relations (2.18) to hold if we take a very limited subset of the E's, namely those that have the very largest magnitudes? For these very large E's, one can write the following equation, assuming the equal-atom case again,

$$E_{\vec{k}} = N^{-1/2} \sum_{j=1}^{N} \exp(2\pi i\vec{k}.\vec{r}_j) \sim N^{1/2} < \exp(2\pi i\vec{k}.\vec{r}_j)>_j . \qquad (2.21)$$

In this case, to obtain a very large value of E almost all the terms in the summation must have nearly the same value. If in this case one considers the product

$$E_{\vec{k}}\, G_{\vec{h}-\vec{k}} = N^{1/2} <\exp(2\pi i\vec{k}.\vec{r}_j>.M^{-1/2}[\sum_{j=1}^{N} \exp(2\pi i\vec{h}.\vec{r}_j)\exp(-2\pi i\vec{k}.\vec{r}_j)$$

$$+ \sum_{j=N+1}^{M} \exp(2\pi i\vec{h}.\vec{r}_j).\exp(-2\pi i\vec{k}.\vec{r}_j)]$$

and recognizing then that for the particular index $\vec{k}$, we can to a good approximation, substitute the average exponential for the N summation, then

$$E_{\vec{k}}\, G_{\vec{h}-\vec{k}} = (N/M)^{1/2}[\sum_{j=1}^{N} \exp(2\pi i\vec{h}.\vec{r}_j) + (\sum_{j=N+1}^{M} \exp\{2\pi i(\vec{h}-\vec{k}).\vec{r}_j\})$$

$$. <\exp(2\pi i\vec{k}.\vec{r}_j)>]. \qquad (2.22)$$

Thus if we have just a few terms that have large values of the $E_{\vec{k}}$'s, the first term on the right hand side for each would be identical and the second would vary depending on the particular interaction between the indicies and the extra atoms and hence would tend to cancel out when averaged over a reasonably small number of terms; i.e.,

$$NM^{-1/2}E_{\vec{h}} \sim \langle E_{\vec{k}} G_{\vec{h}-\vec{k}} \rangle_{\vec{k}}. \qquad (2.23)$$

One could extend this even further by inquiring about the situation when both $E_{\vec{k}}$ and $G_{\vec{h}-\vec{k}}$ are large in magnitude. Since this can only occur when all the individual phase contributions are approximately the same, one can write

$$E_{\vec{k}} G_{\vec{h}-\vec{k}} \sim N^{1/2}\langle \exp(2\pi\vec{k}.\vec{r}_j)\rangle_j . (M^{1/2})\langle \exp[2\pi i(\vec{h}-\vec{k}).\vec{r}_j]\rangle_j$$

$$\sim (NM)^{1/2}\langle \exp(2\pi i\vec{k}.\vec{r}_j)\rangle_j . \langle\exp(2\pi i\vec{h}.\vec{r}_j)\rangle_j . \langle\exp(-2\pi i\vec{k}.\vec{r}_j)\rangle_j$$

$$\sim (NM)^{1/2}\langle\exp(2\pi i\vec{h}.\vec{r}_j)\rangle_j . \qquad (2.24)$$

For large $E_{\vec{h}}$, we obtain

$$M^{1/2}E_{\vec{h}} \sim E_{\vec{k}} G_{\vec{h}-\vec{k}}. \qquad (2.25)$$

For centrosymmetric structures, equation (2.25) indicates the sign relationship

$$s_{\vec{h}} \sim s_{\vec{k}} . s_{\vec{h}-\vec{k}} \qquad (2.26)$$

holds, which is similar to the probabilistic triple-sign relationship given by Sayre[26] and Cochran.[27] Here, however the probability that (2.26) holds is expected to be determined by the product of $E_{\vec{h}}E_{\vec{k}}$ with $G_{\vec{h}-\vec{k}}$ instead of with $E_{\vec{h}-\vec{k}}$.

A Modified Tangent Formula

For noncentrosymmetric structures, the angle-dependent part of the Sayre's equations, (2.1)-(2.3), may be summarized as

$$\alpha_{\vec{h}} = \text{phase of } \Sigma_{\vec{k}} E_{\vec{k}} E_{\vec{h}-\vec{k}}, \qquad (2.27)$$

which is often expressed in the form of

$$\tan \alpha_{\vec{h}} = \frac{\Sigma_{\vec{k}} |E_{\vec{k}} E_{\vec{h}-\vec{k}}| \sin(\alpha_{\vec{k}} + \alpha_{\vec{h}-\vec{k}})}{\Sigma_{\vec{k}} |E_{\vec{k}} E_{\vec{h}-\vec{k}}| \cos(\alpha_{\vec{k}} + \alpha_{\vec{h}-\vec{k}})} . \qquad (2.28)$$

Equation (2.28) is the well-known "tangent formula" which was obtained by Karle and Hauptman[23] on the basis of statistical argument and emphasized that $\alpha_{\vec{h}}$ can be calculated from all the E's whose phases are known. In the same fashion, the angular portion of the Σ_2-like relation, (2.18.2) yields

$$\alpha_{\vec{h}} = \text{phase of } \Sigma_{\vec{k}} E_{\vec{k}} G_{\vec{h}-\vec{k}}. \qquad (2.29)$$

Equating real and imaginary parts of equation (2.18.2), and dividing, yields the tangent formula:

$$\tan \alpha_{\vec{h}} \equiv \frac{\Sigma_{\vec{k}} |E_{\vec{h}} G_{\vec{h}-\vec{k}}| \sin(\alpha_{\vec{h}} + \alpha_{\vec{h}-\vec{k}})}{\Sigma_{\vec{k}} |E_{\vec{h}} G_{\vec{h}-\vec{k}}| \cos(\alpha_{\vec{h}} + \alpha_{\vec{h}-\vec{k}})} . \qquad (2.30)$$

This formula, which represents phase-angle relationships among structure factors, $E_{\vec{h}}$, $E_{\vec{k}}$, and $G_{\vec{h}-\vec{k}}$, is termed a "modified tangent formula" in this thesis. It will allow the phases to be determined from the structure factors G, which in turn are determined by the Patterson superposition functions.

CHAPTER 3. STATISTICAL PROPERTIES OF G

Introduction

By substituting the pseudo-normalized structure factor G for one of the normalized structure factor E in the product, Sayre's equation becomes our Σ_2-like relation (equation 2.18). One important merit of this new relation is that the phase of G is a known quantity. Thus, via a special case of equation (2.25):

$$E_{\vec{h}} \sim E_{ooo} G_{\vec{h}} \qquad (3.1)$$

one would expect that the phases of the G's can be assigned to the E's for some large structure factor amplitudes.

Relations such as (2.26) or (3.1) are only approximate results. It is also evident that the minimum function M_{ps} gives only an approximation to the electron density distribution $\rho(\vec{r})$. The pseudo-normalized structure factors G will differ from the E's in magnitude as well as in phase to some extent, which will vary from one superposition map to another. Thus appropriate mathematical forms are needed to make it possible to define precisely how large E and G must be in order that valid sign relationships necessarily exist among them.

In this chapter, statistical properties of the pseudo-normalized structure factors G are studied and probability functions will be derived using the approach of the central limit theorem.[28] This theorem states that the sum of a sufficiently large number N of random variables ξ_j with mean values x_j and mean-square deviations α_j^2 is normally distributed about

$$X = \sum_{j=1}^{N} x_j \tag{3.2}$$

with mean-square deviation

$$A^2 = \sum_{j=1}^{N} \alpha_j^2, \tag{3.3}$$

whatever the distribution functions of the individual random variables.

All of the following studies are based on the idea that phase information provided by the Patterson superposition functions is more or less the same as that obtained from a heavy-atom case. In the latter case, we know the phase contribution from one or two of heavy atoms but not the whole. In the superposition case, we know the phase contribution from all the atoms including both the real and the false but not the part corresponding to just the real.

Fraction of Structure Factors Determined in Sign by G

Here, we shall examine the simpler problem of estimating how many structure factors in a given case can be expected to be determined in sign by contributions to the structure factors of a group of atoms which are composed not only of correct ones but also false ones. This deviation follows that of Sim's[29] which was applied to the case of heavy-atom structures.

For the sake of simplicity, and only in this section the notation G will stand for pseudo structure factors instead of the pseudo-normalized structure factors.

Suppose that in a centrosymmetric structure, the Patterson superposition function shows electron densities which can be identified as M discrete atom peaks among which N peaks belong to a desired image of the structure and the remaining (M-N) peaks occur at extraneous sites. Thus peaks can be divided into two groups. Let the contribution of the first N-atom group to the structure factor G be F_1 and the second (M-N) atom group be F_2. We can write

$$G = F_1 + F_2 \tag{3.4}$$

where

$$F_1 = \sum_{j=1}^{N/2} 2f_j\cos(\vec{h}.\vec{r}_j)$$

and

$$F_2 = \sum_{j=N/2+1}^{M/2} 2f_j\cos(\vec{h}.\vec{r}_j).$$

Since the atoms in the first group are considered real and complete, the structure factor F_1 can be replaced by F, the observed structure factor. F_2 is the structure factor from the contribution of the remaining (M-N) atoms (hereafter, these atoms shall be called "extraneous atoms").

Equation (3.4) can be rearranged as

$$F = G - F_2.$$

Now let s(F), s(G), and s(F_2) be the signs of F, G, and F_2, respectively. The conditions for s(F) to be "+" or "-" are considered separately in the following:

a) s(G)=(+), s(F_2)=(+) when $|G|>|F_2|$
(i) s(F)=(+) : b) s(G)=(+), s(F_2)=(-) (no condition)
or
c) s(G)=(-), s(F_2)=(-) when $|F_2|>|G|$

a) s(G)=(-), s(F_2)=(-) when $|G|>|F_2|$
(ii) s(F)=(-) : b) s(G)=(-), s(F_2)=(+) (no condition)
or
c) s(G)=(+), s(F_2)=(+) when $|F_2|>|G|$

It can be seen that whether the sign of F is "+" or "-", condition (c) in both (i) and (ii) cases violates the requirement that s(F) = s(G). Therefore it can be noted that F and G differ in sign only when G and F_2 have the same sign, and F_2 exceeds G in magnitude.

Let the mean and mean-square-deviation of F_2 be $\underline{M}$ and q^2, respectively, where

$$\underline{M} = \sum_{j=N/2+1}^{M/2} \langle 2f_j \cos(\vec{h}.\vec{r})\rangle = 0$$

and

$$q^2 = \sum_{j=N/2+1}^{M/2} \langle\{2f_j\cos(\vec{H}.\vec{r}_j)-\langle 2f_j\cos(\vec{H}.\vec{r}_j)\rangle\}^2\rangle = \sum_{j=N+1}^{M} f_j{}^2.$$

Since it is only necessary that $|F_2|$ be slightly greater than $|G|$ to obtain the result that $s(F) \neq s(G)$, we can then, using the central-limit theorem, write the probability of F_2 having the same sign as G but exceeding it in magnitude as

$$P = (2\pi q^2)^{-1/2}\int_G^\infty \exp(-G^2/2q^2)dG = 1/2 - \psi(G/q),$$

where $\psi(x)$ is the well-tabulated statistical integral

$$(2\pi)^{-1/2}\int_0^x \exp\{(-1/2)t^2\}dt.$$

Accordingly, the probability that G determines the sign of this structure factor is $(1 - P)$, i.e. $1/2 + \psi(G/q)$.

Now let the mean-square deviation of the structure factor G be p^2 where

$$p^2 = \sum_{j=1}^{M} f_j{}^2.$$

The probability that G lies between G and G+dG is given by

$$P(G)dG = (2\pi p^2)^{-1/2}\exp(-G^2/2p^2)dG.$$

Therefore the number of structure factors F (or E) which have their signs determined by the structure factors G, when expressed as a fraction of the total number of structure factors, is

$$N_f = (2\pi p^2)^{-1/2} \int_0^{-\infty} \{ \tfrac{1}{2} + \psi(G/q) \} \exp(-G^2/2p^2) dG.$$

On making the substitution $y=G/p$ and $r=p/q$, the expression becomes

$$N_f = (2/\sqrt{(2\pi)}) \int_0^{\infty} \{(1/2) + \psi(ry)\} \exp(-y^2/2) dy. \qquad (3.5)$$

This has been integrated numerically for a range of values of r and the results are listed in Table A-1.

It should be noted that the factor r is always greater than unity and will in general vary with the Bragg angle θ because of the differing relative variation of scattering factors with θ. Over a small range of θ, however, the factor r may be treated as a constant.

The values of N_f in Table A-1 enable one to predict the number of structure factors whose signs will be correctly determined by the pseudo structure factors G.

Sign Probability

For a particular structure factor, the probability that G determines its sign will be derived in terms of the normalized quantities G and E via a different approach, one which follows that used by Woolfson[30] in heavy-atom methods. Definitions of different structure factors and their mean-square deviations

Table A-1. Values of N_f as a function of r.

The fraction of true structure factors determined in sign by the pseudo structure factors G expressed in terms of the ratio of the root-mean-square contribution of the total atoms on the superposition map to that of the "extraneous" atoms

r	N_f	r	N_f
1.0000	0.500	1.8868	0.822
1.0198	0.563	2.0591	0.839
1.0770	0.621	2.2361	0.852
1.1662	0.672	2.6926	0.879
1.2806	0.715	3.1623	0.898
1.4142	0.750	3.6401	0.912
1.5620	0.779	4.1231	0.922
1.7205	0.803		

for PI and P1 structures are given in Table A-2.

According to the definitions in Table A-2, we obtain

$$E = gG - rE_2 \qquad (3.6)$$

For a particular structure factor E, its sign s(E) is unknown, but the sign of the corresponding structure factor G, let it be s_G, is known. Then (3.6) becomes

$$E_2 = s_G(|gG| - |E|)/r \text{ if GE is positive}$$

or

$$E_2 = s_G(|gG| + |E|)/r \text{ if GE is negative}$$

The ratio of the probability that GE is positive, $P_+(GE)$, divided by the probability that GE is negative, $P_-(GE)$, is then

$$\frac{P_+(GE)}{P_-(GE)} = \frac{\exp[-\frac{1}{2r^2}(|gG| - |E|)^2]}{\exp[-\frac{1}{2r^2}(|gG| + |E|)^2]}$$

Since

$$P_+ + P_- = 1,$$

we find

$$P_+ = \frac{1}{2} + \frac{1}{2}\tanh\left(\frac{|gG||E|}{r^2}\right) \qquad (3.7)$$

and

$$P_- = \frac{1}{2} - \frac{1}{2}\tanh\left(\frac{|gG||E|}{r^2}\right) \qquad (3.8)$$

Table A-2. Definitions of the structure factors and their mean-square-deviations

Structure Factor	m.s. deviation (centrosymmetric)	m.s. deviation (non-centrosymm.)
$G = \sum_{j=1}^{M} Z_j \exp(\vec{h}.\vec{r}_j)/p$	$p^2 = \sum_{j=1}^{M} Z_j^{2}$	$\frac{1}{2}\, p^2$
$E = \sum_{j=1}^{N} Z_j \exp(\vec{h}.\vec{r}_j)/(\sigma_2)^{1/2}$	$\sigma_2 = \sum_{j=1}^{N} Z_j^{2}$	$\frac{1}{2}\, \sigma_2$
$E_2 = \sum_{j=N+1}^{M} Z_j \exp(\vec{h}.\vec{r}_j)/q$	$q^2 = \sum_{j=N+1}^{M} Z_j^{2}$	$\frac{1}{2}\, q^2$
$g = (p_2 / \sigma_2)^{1/2}$;	$r = (p_2 / q_2)^{1/2}$	

where

$$\frac{|gG||E|}{r^2} = \frac{|pG||\sigma_2^{1/2}E|}{q^2}$$

Equations (3.7) and (3.8) give the probability that E has the same sign as and opposite sign to G, respectively.

Distribution of the Phase Angle in Non-Centrosymmetrical Structures

The expected distribution of the phase angles of the pseudo-normalized structure factors G about the phase angles of the structure factors E is derived in this section. This follows Sim's work[31] in which the calculation was done on structures containing heavy atoms.

Let us start with equation (3.6). This equation can be rewritten as

$$rE_2 = gG - E. \tag{3.9}$$

In this equation rE_2, gG and E are all complex numbers. For E we define:

$$E = X + iY$$
$$R = |E|; \quad R^2 = X^2 + Y^2,$$
$$X = R\cos\xi; \quad Y = R\sin\xi.$$

Since X and Y can be considered to be independent random variables and the mean-square-deviation is 1/2 for both the X and Y components, the distribution density for the real and imaginary parts of the structure factor are:

$$P(X) = \pi^{-1/2}\exp(-X^2),$$
$$P(Y) = \pi^{-1/2}\exp(-Y^2).$$

The probability that components of E are in the ranges X, X+dX and Y, Y+dY is

$$P(X,Y)dXdY = \pi^{-1}\exp[-(X^2 + Y^2)]. \qquad (3.10)$$

For the present problem, we consider the probability density for the structure factor $rE_2 = X_2 + iY_2$.

Equation (3.10) then becomes:

$$P(X_2,Y_2)dX_2dY_2 = (\pi r^2)^{-1}\exp[-(X_2{}^2 + Y_2{}^2)/r^2]dX_2dY_2. \quad (3.11)$$

Let us now consider the calculated quantity gG as a fixed number. For simplicity, we may assume that the calculated phase γ is zero (this may be achieved for any given reflection by an origin shift of the crystal axes); the corresponding situation is given in Fig. A-1: the quantity gG is now a real, positive number.

The probability density P(X,Y) of the vector $E = gG - rE_2 = X + iY$, given the value of gG, is now obtained by substituting $X_2 = g|G| - X$ and $Y_2 = -Y$ into the right-hand side of (3.11),

$$P(X,Y) = (\pi r^2)^{-1}\exp\{-[X^2 + Y^2 + |gG|^2 - 2X|gG|]/r^2\}.$$

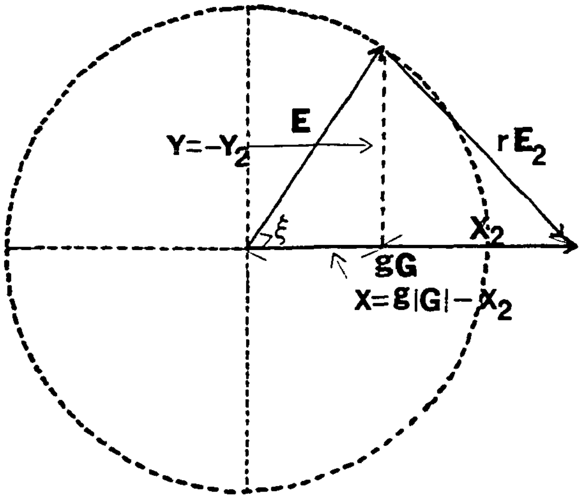

Fig. A-1. Vector diagram for $\gamma = 0$.

Transformation to polar coordinates, using (3.10) and $dXdY = RdRd\xi$, gives

$$P(|E|,\xi)d|E|d\xi = \frac{|E|}{\pi r^2} \exp\{ \frac{-(|E|^2 + |gG|^2)}{r^2} \}$$
$$\times \exp(\frac{2|gG||E|\cos\xi}{r^2} \quad d|E|d\xi. \qquad (3.12)$$

This is the joint probability of obtaining a normalized structure factor with amplitude between $|E|$ and $|E|+d|E|$ and with $(\alpha - \gamma)$ between ξ and $\xi+d\xi$ for fixed values of $|G|$ and γ, where α and γ are phase angles of E and G, respectively.

Integration over all angles gives the probability of obtaining a value of $|E|$ between $|E|$ and $|E|+d|E|$

$$P(|E|)d|E| = 2(|E|/r^2)\exp[-(|E|^2 + |gG|^2)/r^2]$$
$$\times I_0[2|gG||E|\cos\xi/r^2]d|E|,$$

where I_0 is the modified zero-order Bessel function. The probability of $(\alpha - \gamma)$ lying between ξ and $\xi+d\xi$ for a structure factor with fixed values of $|E|,|G|$ and γ is

$$P(\xi)d\xi = P(|E|,\xi)d|E|d\xi \;/\; P(|E|)d|E|,$$
$$= \exp(X\cos\xi)d\xi \;/\; 2\pi I_0(X), \qquad (3.13)$$

where

$$X = 2|E||gG|/r^2 = 2p\sigma_2{}^{1/2}|E||G|/q^2$$

$$= \frac{2(\sigma_2\sigma_2')^{1/2}}{\sigma_2' - \sigma_2} |E||G|. \qquad (3.14)$$

The probability that $(\alpha - \gamma)$ lies between the limits $\pm\xi$ is then given by

$$P(\xi) = \int_{-\xi}^{+\xi} P(\xi)\, d\xi. \qquad (3.15)$$

Values of $P(\xi)$ for various values of X and ξ are listed in Table A-3. The results indicate that the larger the value of X the more likely $|\alpha - \gamma|$ is to be small, and conversely the smaller the value of X the more likely $|\alpha - \gamma|$ is to be large.

Table A-3. Values of $P(\xi)$

				X			
		0	1	2	3	4	5
	0°	0.000	0.000	0.000	0.000	0.000	0.000
	20°	0.111	0.234	0.346	0.431	0.496	0.549
	40°	0.222	0.442	0.621	0.737	0.811	0.862
	60°	0.333	0.609	0.798	0.896	0.944	0.969
	80°	0.444	0.733	0.896	0.961	0.985	0.994
ξ	100°	0.556	0.821	0.946	0.985	0.996	0.999
	120°	0.667	0.883	0.971	0.994	0.999	0.999
	140°	0.778	0.930	0.984	0.997	0.999	1.000
	160°	0.889	0.967	0.993	0.999	1.000	1.000
	180°	1.000	1.000	1.000	1.000	1.000	1.000

CHAPTER 4. STATISTICAL THEORY OF THE TRIPLE-PHASE RELATIONSHIPS

Introduction

It is well known that for a centrosymmetric crystal the signs of structure factors $E_{\vec{h}}$, $E_{\vec{k}}$, and $E_{\vec{h}-\vec{k}}$ are related by the "sign relation"

$$s_{\vec{h}} \sim s_{\vec{k}} \cdot s_{\vec{h}-\vec{k}} . \tag{4.1}$$

When the crystal is not centrosymmetric, an analogous relation holds between the phase angles:

$$\alpha_{\vec{h}} \sim \alpha_{\vec{k}} + \alpha_{\vec{h}-\vec{k}} . \tag{4.2}$$

These triple-phase relationships are the most important phase-determining formulas. Their related probabilities have been developed by Cochran and Woolfson[25] for centrosymmetric and by Cochran[32] for noncentrosymmetric structures:

centrosymmetric case:

$$P_+(E_{\vec{h}} E_{\vec{k}} E_{\vec{h}-\vec{k}}) = \frac{1}{2} + \frac{1}{2} \tanh(\frac{X}{2}) \tag{4.3}$$

noncentrosymmetric case:

$$P(\alpha_{\vec{h}}) = \frac{\exp[\ \chi\cos\{\ \alpha_{\vec{k}} + \alpha_{\vec{h}-\vec{k}} - \alpha_{\vec{h}})\}]}{2\pi I_o(\chi)} \qquad (4.4)$$

where

$$\chi = 2\sigma_3\sigma_2^{-3/2}\ |E_{\vec{h}}E_{\vec{k}}E_{\vec{h}-\vec{k}}| \qquad (4.5)$$

and I_o is a modified Bessel function.

In this chapter, quantitative expressions for the probability that the triple-sign relationship such as (4.3) or (4.4) is true among the structure factors $E_{\vec{h}}$, $E_{\vec{k}}$, and $G_{\vec{h}-\vec{k}}$ shall be derived. Our derivations will follow the arguments of those given by Cochran and Woolfson.[25,32]

The Distribution of Values of $E_{\vec{k}}G_{\vec{h}-\vec{k}}$

Let us first consider the distribution of values of $E_{\vec{k}}\ G_{\vec{h}-\vec{k}}$ for a fixed value of $E_{\vec{h}}$ in PI structures. The pseudo normalized structure factors $G_{\vec{h}-\vec{k}}$ may be written as

$$G_{\vec{h}-\vec{k}} = \frac{2}{(\ \sigma_2{}')^{1/2}} \sum_{j=1}^{M/2} Z_j\cos(\vec{h}-\vec{k}).\vec{r}_j = \sum_{j=1}^{M/2} \xi_j + \sum_{j=1}^{M/2} \phi_j$$

where

$$\xi_j = 2\sigma_2{}'^{-1/2}Z_j\cos2\pi\vec{h}.\vec{r}_j\cos2\pi\vec{k}.\vec{r}_j$$

and

$$\phi_j = 2\sigma_2{}'^{-1/2}Z_j\sin2\pi\vec{h}.\vec{r}_j\sin2\pi\vec{k}.\vec{r}_j.$$

If $E_{\vec{h}}$ is fixed in value and index, and $E_{\vec{k}}$ is of fixed value, then

$$\langle\xi_j\rangle = \langle\, 2\sigma_2{}'^{-1/2} Z_j \cos 2\pi\vec{h}.\vec{r}_j \cos 2\pi\vec{k}.\vec{r}_j \,\rangle_{\vec{k}}$$
$$= 2(\sigma_2\ \sigma_2{}')^{-1/2}\ Z_j{}^2\ E_{\vec{k}}\ \cos 2\pi\vec{h}.\vec{r}_j$$

where the mean value of $\cos 2\pi\vec{k}.\vec{r}_j$ is $\sigma_2{}^{-1/2} Z_j\ E_{\vec{k}}$. The variance of ξ_j is $\alpha_j{}^2 = \langle\xi_j{}^2\rangle - \langle\xi_j\rangle^2$. If we ignore $\langle\xi_j\rangle^2$ (of order N^{-2}), then

$$\alpha_j{}^2 = \langle\, 4\sigma_2{}'^{-1} Z_j{}^2 \cos^2 2\pi\vec{h}.\vec{r}_j \cos^2 2\pi\vec{k}.\vec{r}_j \,\rangle_{\vec{k}}$$
$$= 2\sigma_2{}'^{-1} Z_j{}^2 \cos^2 2\pi\vec{h}.\vec{r}_j .$$

Similarly we find that ϕ_j has mean value $\langle\phi_j\rangle = 0$ and variance $\beta_j{}^2 = 2\sigma_2{}'^{-1} Z_j{}^2 \sin^2 2\pi\vec{h}.\vec{r}_j$.

If the variables ξ_j and ϕ_j are assumed to be independent, then the application of the central-limit theorem shows that $G_{\vec{h}-\vec{k}}$ has a Gaussian distribution about a mean value

$$\sum_{j=1}^{M/2} \langle\xi_j\rangle + \sum_{j=1}^{M/2} \langle\phi_j\rangle = (\sigma_2\sigma_2{}')^{-1/2} \sum_{j=1}^{M/2} 2Z_j{}^2 E_{\vec{k}} \cos 2\pi\vec{h}.\vec{r}_j$$
$$= \frac{\sigma_1{}^2}{(\sigma_2\ \sigma_2{}')^{-1/2}}\ (\,V_{\vec{h}} + \Delta V_{\vec{h}})\ E_{\vec{k}}$$

with variance

$$\sum_{j=1}^{M/2} \alpha_j^{\,2} + \sum_{j=1}^{M/2} \beta_j^{\,2} = 1$$

where $V_{\vec{h}}$ is defined in (2.10) and

$$\Delta V_{\vec{h}} = \sum_{j=\frac{N}{2}+1}^{M/2} (2Z_j^{\,2}/ \sigma_1^{\,2}) \cos 2\pi \vec{h}.\vec{r}_j .$$

The probability that $G_{\vec{h}-\vec{k}}$ lies between $G_{\vec{h}-\vec{k}}$ and $G_{\vec{h}-\vec{k}} + dG_{\vec{h}-\vec{k}}$ is then

$$P_1(G_{\vec{h}-\vec{k}})dG_{\vec{h}-\vec{k}}$$

$$= (2\pi)^{-1/2} \exp[-\{ G_{\vec{h}-\vec{k}} - K(V_{\vec{h}} + \Delta V_{\vec{h}})E_{\vec{k}}\}^2/2]dG_{\vec{h}-\vec{k}} \qquad (4.6)$$

where

$$K = \sigma_1^{\,2}/ (\sigma_2 \sigma_2')^{1/2}. \qquad (4.7)$$

Since we now wish to find the distribution of $E_{\vec{k}}\, G_{\vec{h}-\vec{k}}$ for a fixed $\vec{h}$, we may consider the problem in the following two stages:

(a) $E_{\vec{k}}$ may take all possible values and will have a distribution function

$$P_2(E_{\vec{k}}) = (2\pi\sigma_2)^{-1/2} \exp[- E_{\vec{k}}^{\,2}/ 2\sigma_2].$$

(b) For each $E_{\vec{k}}$ the associated $G_{\vec{h}-\vec{k}}$ will have a value governed by the distribution function (4.6).

If the product $E_{\vec{k}}\ G_{\vec{h}-\vec{k}}$ has a value between Z and Z+dZ where $X = E_{\vec{k}}\ G_{\vec{h}-\vec{k}}$, and $E_{\vec{k}}$ has a value between y and y+dy then $G_{\vec{h}-\vec{k}}$ has a value between Z/y and (Z+dZ)/y. The total probability of a value of $E_{\vec{k}}\ G_{\vec{h}-\vec{k}}$ lying between Z and Z+dZ is therefore

$$P(Z)dZ = 2 \int_0^\infty \frac{1}{y} P_2(y) P_1\left(\frac{Z}{y}\right) dy dZ$$

$$= (\pi^2\sigma_2)^{-1/2} \int_0^\infty \frac{1}{y} \exp(-y^2/2\sigma_2)$$

$$\times \quad \exp\left[-\left\{ \frac{Z}{y} - K(V_{\vec{h}} + \Delta V_{\vec{h}})y\right\}^2/2\right] dy dZ$$

$$= (\pi^2\sigma_2)^{-1/2} \exp[\ KZ(V_{\vec{h}} + \Delta V_{\vec{h}})\ ]$$

$$\times \int_0^\infty \frac{1}{y} \exp\left[\frac{Z^2}{2y^2} + y^2\{(2\sigma_2)^{-1/2} + \frac{K^2}{2}(V_{\vec{h}} + \Delta V_{\vec{h}})^2\right].$$

The probability that $E_{\vec{k}}G_{\vec{h}-\vec{k}}$ lies between $E_{\vec{k}}G_{\vec{h}-\vec{k}}$ and $E_{\vec{k}}G_{\vec{h}-\vec{k}}+dE_{\vec{k}}G_{\vec{h}-\vec{k}}$ is thus

$$P(\ E_{\vec{k}}\ G_{\vec{h}-\vec{k}})$$

$$= (\pi^2\sigma_2)^{-1/2}\exp[\ K\ E_{\vec{k}}\ G_{\vec{h}-\vec{k}}(V_{\vec{h}} + \Delta V_{\vec{h}})]\ I_o(\ldots.) \qquad (4.8)$$

in which K is defined in (4.7).

The Probability That $s_{\vec{h}} = s_{\vec{k}} \cdot s_{\vec{h}-\vec{k}}$

When only the value of $|E_{\vec{h}}|$ is known there are two possible forms of the distribution (4.8), the first having $V_{\vec{h}}$ positive and the second having $V_{\vec{h}}$ negative. For the first hypothesis, the probability of obtaining a certain definite value of $E_{\vec{k}}G_{\vec{h}-\vec{k}}$ is proportional to

$$(\pi^2\sigma_2)^{-1/2}\exp[\ K\ E_{\vec{k}}G_{\vec{h}-\vec{k}}(+|V_{\vec{h}}|+\Delta V_{\vec{h}})]\ I_o(\ldots.)$$

while for the second it is proportional to

$$(\pi^2\sigma_2)^{-1/2}\exp[\ K\ E_{\vec{k}}G_{\vec{h}-\vec{k}}(-|V_{\vec{h}}|+\Delta V_{\vec{h}})]\ I_o(\ldots.).$$

The ratio of the probability that $V_{\vec{h}}$ is positive, $P_+(V_{\vec{h}})$, divided by the probability that $V_{\vec{h}}$ is negative, $P_-(V_{\vec{h}})$, is then

$$\frac{P_+(V_{\vec{h}})}{P_-(V_{\vec{h}})} = \frac{\exp[\ KE_{\vec{k}}G_{\vec{h}-\vec{k}}(|V_{\vec{h}}| + \Delta V_{\vec{h}})]}{\exp[\ KE_{\vec{k}}G_{\vec{h}-\vec{k}}(-|V_{\vec{h}}| + \Delta V_{\vec{h}})]}$$

$$= \exp[2KV_{\vec{h}}E_{\vec{k}}G_{\vec{h}-\vec{k}}]. \qquad (4.9)$$

Since

$$P_+ + P_- = 1.$$

We find

$$P_+ = \frac{1}{2} + \frac{1}{2}\tanh[\frac{\sigma_1{}^2}{(\sigma_2\ \sigma_2{}')^{1/2}}|V_{\vec{h}}|E_{\vec{k}}G_{\vec{h}-\vec{k}}] \qquad (4.10)$$

and

$$P_- = \frac{1}{2} - \frac{1}{2}\tanh[\frac{\sigma_1{}^2}{(\sigma_2\ \sigma_2{}')^{1/2}}|V_{\vec{h}}|E_{\vec{k}}G_{\vec{h}-\vec{k}}]. \qquad (4.11)$$

Replacing $|V_{\vec{h}}|$ by $|E_{\vec{h}}|$ using equation (2.20), (4.10) becomes

$$P_+ = \frac{1}{2} + \frac{1}{2}\tanh[\frac{\sigma_3}{\sigma_2(\ \sigma_2{}')^{1/2}}|E_{\vec{h}}E_{\vec{k}}G_{\vec{h}-\vec{k}}|]. \qquad (4.12)$$

The Probability that $s_{\vec{h}} = s(\Sigma_{\vec{k}}E_{\vec{k}}G_{\vec{h}-\vec{k}})$

Suppose that two sign indications are available from the values of $E_{\vec{k}_1}G_{\vec{h}-\vec{k}_1}$ and of $E_{\vec{k}_2}G_{\vec{h}-\vec{k}_2}$. If $V_{\vec{h}}$ is positive, the probability of obtaining these two values is equal to the product of the probabilities of obtaining them separately, and is proportional to

$$\pi^2\sigma_2 \exp[\ K\ E_{\vec{k}_1} G_{\vec{h}-\vec{k}_1} (|V_{\vec{h}}|+\Delta V_{\vec{h}})]\ I_o(\ldots.)$$

$$\times \exp[\ K\ E_{\vec{k}_2} G_{\vec{h}-\vec{k}_2} (|V_{\vec{h}}|+\Delta V_{\vec{h}})]\ I_o(\ldots.)$$

while if $V_{\vec{h}}$ is negative, the probability is proportional to the same expression with $-|V_{\vec{h}}|$ replacing $+|V_{\vec{h}}|$. Therefore

$$\frac{P_+(V_{\vec{h}})}{P_-(V_{\vec{h}})} = \exp[2K|V_{\vec{h}}|(E_{\vec{k}_1} G_{\vec{h}-\vec{k}_1} + E_{\vec{k}_2} G_{\vec{h}-\vec{k}_2})]. \qquad (4.13)$$

Equation (4.13) can be extended to the case where any number of sign indications are available. The only effect is to replace $E_{\vec{k}_1} G_{\vec{h}-\vec{k}_1} + E_{\vec{k}_2} G_{\vec{h}-\vec{k}_2}$ by $\Sigma_{\vec{k}} E_{\vec{k}} G_{\vec{h}-\vec{k}}$, so that in general

$$P_+ = \frac{1}{2} + \frac{1}{2} \tanh[\ \frac{\sigma_1{}^2}{(\sigma_2\ \sigma_2{}')^{1/2}}\ |V_{\vec{h}}|\ \Sigma_{\vec{k}} E_{\vec{k}}\ G_{\vec{h}-\vec{k}}]. \qquad (4.14)$$

Again by using the relation (2.20), (4.14) becomes

$$P_+ = \frac{1}{2} + \frac{1}{2} \tanh[\ \frac{\sigma_3}{\sigma_2(\ \sigma_2{}')^{1/2}}\ |E_{\vec{h}} \Sigma_{\vec{k}} E_{\vec{k}} G_{\vec{h}-\vec{k}}|]. \qquad (4.15)$$

It can be seen that as the number of terms in the summation increases, the probability that

$$s_{\vec{h}} = s\,(\,\Sigma_{\vec{k}} E_{\vec{k}} G_{\vec{h}-\vec{k}}\,) \tag{4.16}$$

tends to certainty.

The Relation $\alpha_{\vec{h}} = \alpha_{\vec{k}} + \alpha_{\vec{h}-\vec{k}}$

It has been shown that $E_{\vec{h}} \sim M^{1/2} < E_{\vec{k}} G_{\vec{h}-\vec{k}} >_{\vec{k}}$ (equation (2.18.1)). Suppose now that $E_{\vec{k}} G_{\vec{h}-\vec{k}}$ is known for only one value of $\vec{k}$. We write

$$E_{\vec{h}} = (\text{the right-hand side of } (2.16)).$$

It then follows that the expected value of $E_{\vec{h}}$ is

$$<E_{\vec{h}}>_{\vec{h}} \sim M^{1/2} E_{\vec{k}} G_{\vec{h}-\vec{k}}. \tag{4.17}$$

For a crystal which lacks a center of symmetry, (4.17) relates complex numbers and thus it requires both

$$<|E_{\vec{h}}|> \sim M^{1/2} |E_{\vec{k}} G_{\vec{h}-\vec{k}}|$$

and

$$<\alpha_{\vec{h}}> \sim \alpha_{\vec{k}} + \alpha_{\vec{h}-\vec{k}}.$$

From procedures closely similar to those set out by Cochran[32] and the fact that the probability functions (4.3) and (4.12) have exactly the same form, we conclude that the probability function for $\alpha_{\vec{h}}$ distributed about $\langle\alpha_{\vec{h}}\rangle$ is the same as (4.4) except that

$$\chi = 2\sigma_3(\sigma_2{}^2\sigma_2{}')^{-1/2}|E_{\vec{h}}E_{\vec{k}}G_{\vec{h}-\vec{k}}| \tag{4.18}$$

when atoms are not equal.

Values of the function (4.4) are given in Table A-4. Note that the value of χ in (4.18) differs from that in (4.5) in the so-called "phase efficiency constant". This constant is characteristic of a structure since values of |E| (or |G| for a Patterson superposition structure)) of the same order of magnitude are to be expected whatever the complexity of the crystal structure.[33] In Sayre's Σ_2 relations, the efficiency of the phase relationship is governed by the quantity $\sigma_3\sigma_2{}^{-3/2}$ which varies approximately as $N^{-1/2}$, while in our Σ_2-like relations, the phase efficiency constant becomes $\sigma_3(\sigma_2{}^2\sigma_2{}')^{-1/2}$ which varies approximately as $M^{-1/2}$.

Table A-4. Values of $\dfrac{\exp[\chi\cos\{\alpha_{\vec{k}} + \alpha_{\vec{h}-\vec{k}} - \alpha_{\vec{h}}\}]}{2\pi I_o(\chi)}$

	$\{\alpha_{\vec{k}} + \alpha_{\vec{h}-\vec{k}} - \alpha_{\vec{h}}\}$									
	0°	20°	40°	60°	80°	100°	120°	140°	160°	180°
0	0.159	0.159	0.159	0.159	0.159	0.159	0.159	0.159	0.159	0.159
1	0.342	0.322	0.271	0.207	0.149	0.105	0.076	0.059	0.049	0.046
2	0.516	0.457	0.323	0.190	0.099	0.049	0.025	0.015	0.011	0.009
3	0.655	0.547	0.325	0.146	0.055	0.019	0.007	0.003	0.002	0.002
4	0.769	0.604	0.302	0.104	0.028	0.007	0.00			
χ 5	0.867	0.642	0.269	0.071	0.014	0.002				
↓ 6	0.965	0.673	0.237	0.048	0.007					
7	1.035	0.679	0.261	0.031	0.003					
8	1.110	0.686	0.171	0.020						
9	1.179	0.686	0.144	0.013						
10	1.245	0.682	0.120	0.008						
11	1.308	0.674	0.099	0.006						
12	1.367	0.664	0.083	0.003						

CHAPTER 5. PHASE REFINEMENT

Introduction

The phases of the structure factors G are distributed about values of the true phase of the structure factor E. If phase errors in the G's can be corrected, real structures can be obtained immediately.

Improvement of the phases can be carried out by solution of the tangent formula (equation 2.28) which was first suggested by Karle and Hauptman.[34] The suggestion was adopted in the mid-1960's and is now one of the major facets of direct methods. The technique is based upon the following iteration:

$$\text{phase of} < E_{\vec{k}}^{\,i} E_{\vec{h}-\vec{k}}^{\,i} >_{\vec{k}} = \alpha_{\vec{h}}^{\,i+1} \tag{5.1}$$

where the E^i are the structure factors phased with the results of the ith cycle, and the α^{i+1} are the results corresponding to the (i+1)st cycle. Acceptance or rejection of a phase produced by (5.1) is usually governed by rules which vary from one procedure to another.

It has been shown that our Σ_2-like relation yields a modified tangent formula (2.30). Thus phase refinement is expected to be achieved by employing the following iteration:

$$\text{phase of} < E_{\vec{k}}^{\,i} G_{\vec{h}-\vec{k}}^{\,i} >_{\vec{k}} = \alpha_{\vec{h}}^{\,i+1} . \tag{5.2}$$

There is a major difference between the phase refinements based on (5.1) and (5.2). In (5.1), phases of the E's in the product are only initially known for a limited set of reflections while in (5.2) the phases of the G's are known for all reflections.

Phases obtained from Patterson superposition functions are, in a sense, comparable with those obtained from partial structures. The capability of the tangent formula to yield the complete structure from a partial structure has already been thoroughly investigated by Karle.[35] One good example is the well-known "Karle recycling" procedure. If the phases of the G's are taken as those obtained from a partial structure (it actually exceeds a partial structure), they can be refined by the tangent formula (2.28) in which only the phases of the $|G|$'s are employed in phase refinement. This would be very similar to Karle's recycling procedure.

Our modified tangent formula phase refinement and Karle's recycling procedure are methods of directly finding correct phases for the E's. There is an indirect way to correct the phase error in the G's. This is to find the phase contribution due to the electron density which appears on the Patterson superposition function, but does not belong to the real structure. This approach is similar to Beurskens's DIRDIF procedure[14] in which tangent refinement takes place on the difference structure factors to yield phase information about the missing part of the original structure. In our case, the refinement can take place on the difference structures rE_2 (see equation (3.6)) to yield phases related to the extraneous part of the Patterson superposition structure.

In this chapter, three different approaches to phase refinement which are based on either our Σ_2-like relation or Sayre's Σ_2 relation will be developed for both centrosymmetric and noncentrosymmetric crystals.

Refinement Based on the Σ_2-like Relation

Phase-determining procedures involving the pseudo-normalized structure factors G are quite different from those of MULTAN.[12] First, no origin-defining procedure is required and also it is not necessary to define the enantiomorph for acentric structures. Second, two independent phase sets are employed in the phase-determining process, one containing the phases of G's, the other of E's. An initial phase set for the structure factors E are obtained from G's by a so-called "phase transferring procedure". The size of this initial phase set can be a variable depending on the statistical properties of G (c.f., Chapter 3). Third, phases are refined and expanded by the modified tangent formula, equation (2.30).

Centrosymmetric case

A weighted form of our Σ_2-like formula may be given as:

$$s(E_{\vec{h}}) \sim s\,(\Sigma_{\vec{k}}\, W_{\vec{k}}\, E_{\vec{k}} G_{\vec{h}-\vec{k}}) \qquad (5.3)$$

where $W_{\vec{k}}$ is the weight for $E_{\vec{k}}$. The summation is over all available terms. Since the sign of the structure factor $G_{\vec{h}-\vec{k}}$ is known, the weight for $G_{\vec{h}-\vec{k}}$ is unity and thus is neglected in (5.3). The initial weight to be assigned to the E's will be

$$W = 2P_+ - 1 \qquad (5.4)$$

where

$$P_+ = \frac{1}{2} + \frac{1}{2}\tanh\Big[\frac{(\sigma_2\sigma_2')^{1/2}}{\sigma_2' - \sigma_2}|E||G|\Big]. \qquad (5.5)$$

The value of W indicates how true the sign of the E is at the initial stage.

The probability for the phase obtained from (5.3) being correct will be

$$P_s = \frac{1}{2} + \frac{1}{2}\tanh[\,\kappa\, \Sigma_{\vec{k}} W_{\vec{k}} E_{\vec{h}} E_{\vec{k}} G_{\vec{h}-\vec{k}}] \qquad (5.6)$$

where

$$\kappa = \sigma_3(\sigma_2{}^2\sigma_2')^{-1/2}. \qquad (5.7)$$

The new weight, W_s for the $\vec{h}$ reflection will then be $2P_s - 1$. If W_s exceeds W, the new sign replaces the old sign, if different, and the weight of that reflection is replaced by the new weight.

Noncentrosymmetric case

For noncentrosymmetric structures new phases will be obtained by means of the modified tangent formula (equation (2.30)). A weighted form of this formula may be written as

$$\tan \alpha_{\vec{h}} = \frac{\Sigma_{\vec{k}} W_{\vec{k}} |E_{\vec{k}} G_{\vec{h}-\vec{k}}| \sin(\alpha_{\vec{k}} + \alpha_{\vec{h}-\vec{k}})}{\Sigma_{\vec{k}} W_{\vec{k}} |E_{\vec{k}} G_{\vec{h}-\vec{k}}| \cos(\alpha_{\vec{k}} + \alpha_{\vec{h}-\vec{k}})} = \frac{T_{\vec{h}}}{B_{\vec{h}}}. \qquad (5.8)$$

Since the initial phase angles of the E's are from those of the G's, the initial weight W to be assigned to the structure factor E should depend on the probable magnitude of the phase angle error $(\alpha - \gamma)$. It has shown in Chapter 3 that

$$P(\xi)d\xi = \exp(X\cos\xi)d\xi / \, 2\pi I_0(X) \qquad (3.13)$$

and

$$X = \frac{2(\sigma_2\sigma_2')^{1/2}}{(\sigma_2' - \sigma_2)} |E||G|. \qquad (3.14)$$

where $\xi = (\alpha - \gamma)$.

Following Blow and Crick,[36] it can be shown that appropriate weights are defined by

$$W = \int_{-\pi}^{+\pi} \cos\xi P(\xi)d\xi$$

and consequently

$$W = I_1(X)/I_0(X), \tag{5.9}$$

where I_0 and I_1 are modified Bessel functions of the zero and first orders, respectively. This equation can also be expressed as the polynomial

$$I_1(X)/I_0(X) \simeq 0.5658X - 0.1304X^2 + 0.0106X^3 \tag{5.10}$$

in the range of $0 \leq X \leq 6$; for $X > 6$ the value of the function is essentially unity.

The strength of the new phase indication obtained from (5.8) can be estimated from

$$\tau_{\vec{h}} = 2\ \kappa\ |E_{\vec{h}}|(T_{\vec{h}}^{\ 2} + B_{\vec{h}}^{\ 2})^{1/2}, \tag{5.11}$$

and κ is defined in equation (5.7). If there is only one contributor to the indication for the new phase then we write

$$\tau_{\vec{h}} = 2\ \kappa\ |E_{\vec{h}}E_{\vec{k}}G_{\vec{h}-\vec{k}}|. \tag{5.12}$$

There are two possible functions for the new weight W_s for the phase angle obtained from (5.8):

$$\text{(i) } W_s = \min\{1.0,\ 2\tau_{\vec{h}}\} \tag{5.13}$$

$$\text{(ii) } W_s = \tanh[\ \tfrac{1}{2}\ \tau_{\vec{h}}]. \tag{5.14}$$

New phases are accepted along with the new weights W_s as long as the value of W_s exceeds the original assigned value of W.

Refinement Based on the Σ_2 Relation

If only the phases of the pseudo-normalized structures G are to be used, phase refinement via Sayre's Σ_2 phase relationship (tangent formula, see equation (2.28)) will work the same way as mentioned in the above section except that one more weight is included. All the E's are now assigned a phase value corresponding to that of G. The E's used in phase calculations may be restricted to those whose magnitude are large. Phase refinement will then start with initial assigned phases and output optimized values.

Centrosymmetric case

A weighted Σ_2 sign relationship may be given as:

$$s(E_{\vec{h}}) \sim s\,(\Sigma_{\vec{k}}\; W_{\vec{k}} W_{\vec{h}-\vec{k}} E_{\vec{k}} E_{\vec{h}-\vec{k}}) \qquad (5.15)$$

where W's are the weights for the E's. The initial value of W can be estimated from (5.4). A new sign obtained from (5.15) being correct will have the probability

$$P_n = \frac{1}{2} + \frac{1}{2}\tanh[\lambda E_{\vec{h}} \Sigma_{\vec{k}} W_{\vec{k}} W_{\vec{h}-\vec{k}} E_{\vec{k}} E_{\vec{h}-\vec{k}}] \qquad (5.16)$$

and

$$\lambda = 2\sigma_3 \sigma_2^{-3/2}. \qquad (5.17)$$

Consequently, the new weight for the new sign indication is

$$W_n = (2P_n - 1). \tag{5.18}$$

The new sign will replace the old sign along with the new weight W_s if they are different and if the new weight is greater than the old one.

Noncentrosymmetric case

A weighted form of the tangent formula has been given by Germain et al.[37] as

$$\tan \alpha_{\vec{h}} = \frac{\Sigma_{\vec{k}} W_{\vec{k}} W_{\vec{h}-\vec{k}} |E_{\vec{k}} E_{\vec{h}-\vec{k}}| \sin(\alpha_{\vec{k}} + \alpha_{\vec{h}-\vec{k}})}{\Sigma_{\vec{k}} W_{\vec{k}} W_{\vec{h}-\vec{k}} |E_{\vec{k}} E_{\vec{h}-\vec{k}}| \cos(\alpha_{\vec{k}} + \alpha_{\vec{h}-\vec{k}})} = \frac{S_{\vec{h}}}{C_{\vec{h}}}. \tag{5.19}$$

Initial values of W's are obtained from equation (5.9). The reliability of new phase angle obtained from (5.19) can be computed from

$$\nu_{\vec{h}} = 2\,\lambda\,|E_{\vec{h}}|(S_{\vec{h}}^{\,2} + C_{\vec{h}}^{\,2})^{1/2}, \tag{5.20}$$

where λ is defined in equation (5.17). For only one contributor, (5.20) reduces to

$$\nu_{\vec{h}} = 2\,\lambda\,|E_{\vec{h}} E_{\vec{k}} E_{\vec{h}-\vec{k}}|. \tag{5.21}$$

The new weight for the new phase angle can be estimated from either one of the following functions:

$$\text{(i) } W_n = \min\{1.0,\ 2\nu_{\vec{h}}\} \tag{5.22}$$

$$\text{(ii) } W_n = \tanh[\,\tfrac{1}{2}\,\nu_{\vec{h}}\,]. \tag{5.23}$$

The new phase angle and weight will replace the old one as long as the value of W_n exceeds that of the old weight.

Refinement Based on the Σ_2 Relation Applied to Difference E's

The following derivations follow the same lines used by Gould et al.[38] and van den Hark et al.[39] who have developed the DIRDIF procedures for obtaining the phases of difference structure factors. The results of our derivation will lead to the difference structure factors for the (M-N) extraneous atoms.

Centrosymmetric case

Equation (3.6) can be written as

$$rE_2 = gG - E. \tag{5.24}$$

Two quantities, E_3 and E_4, may be defined as

$$E_3 = s_G(|gG| - |E|)$$
$$E_4 = s_G(|gG| + |E|)$$

where s_G represents the sign of the structure factor G. Since the sign of E is either the same as or opposite to that of the corresponding G, we obtain

$$rE_2 = E_3 \quad \text{when GE is "+"} \qquad (5.25)$$

and

$$rE_2 = E_4 \quad \text{when GE is "-".} \qquad (5.26)$$

If the probability that E_3 is correct, i.e., $E_3 = rE_2$, is defined by P_3, the probability that E_4 is correct is then $1 - P_3$. According to Woolfson[30] the probability P_3 has the form of

$$P_3 = \exp(-\tfrac{1}{2}E_3^2)/[\exp(-\tfrac{1}{2}E_3^2) + \exp(-\tfrac{1}{2}E_4^2)]$$

or

$$P_3 = P(|E_3|)/\{P(|E_3|) + P(|E_3|)\}.$$

Values of P_3 for dual rE_2 values, $|E_3|$ and $|E_4|$, are listed in Table A-5.

In the phase refinement, rE_2 is initially assigned the value of E_3 and the probability that GE = "+" is P_+ which is defined in equation (5.5). The aim of our procedure is to find reflections where E_4 is the correct value.

Now with the known quantities, s_G, $|G|$, and $|E|$ in (5.24), two categories of reflections may be distinguished as shown in Figure A-2.

(1) $|gG|>|E|$. In this case (see Fig. A-2.1) the sign of rE_2 is known to be the same as the sign of G, i.e. $s_G \cdot s_2$ = "+", where s_2 is the sign of rE_2. For reflections in this category, the weight shall be assigned as follows: (a) When $P_+ = 1$: This means that $rE_2 = E_3$. We let $W = 1$

Table A-5. Probability P_3 for dual rE_2 values.

	$\lvert E_4\rvert$=0.4	0.6	0.8	1.0	1.2	1.5	2.0	2.5	3.0	3.5	4.0
$\lvert E_3\rvert$=0.2	0.52	0.54	0.57	0.62	0.67	0.75	0.88	0.957	0.989	0.998	1.000
0.4	0.50	0.52	0.56	0.60	0.66	0.74	0.87	0.954	0.988	0.998	1.000
0.6		0.50	0.54	0.58	0.63	0.72	0.86	0.950	0.987	0.997	1.000
0.8			0.50	0.55	0.60	0.69	0.84	0.943	0.985	0.997	1.000
1.0				0.50	0.56	0.65	0.82	0.932	0.982	0.996	0.999
1.2					0.50	0.60	0.78	0.917	0.978	0.996	0.999
1.5						0.50	0.71	0.88	0.967	0.993	0.999
2.0							0.50	0.76	0.924	0.984	0.998
2.5								0.50	0.80	0.952	0.992
3.0									0.50	0.84	0.971
3.5										0.50	0.87
4.0											0.50

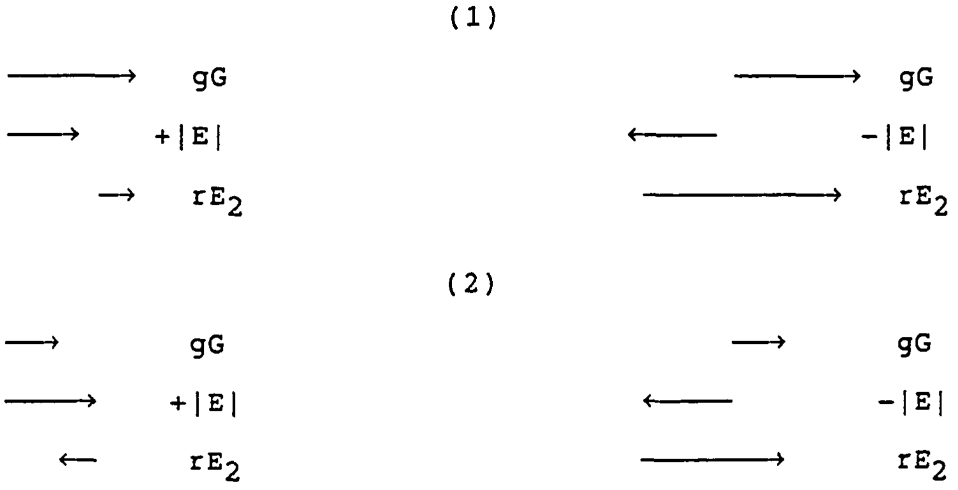

Fig. A-2. Two categories of reflections: (1) $|gG| > |E|$, (2) $|gG| < |E|$. Drawings for a given $|E|$ values. See text for detail.

for E_3 and $s_3 = s_G$.

(b) When $P_+ \neq 1$: This means that rE_2 may be either equal to E_3 or E_4. The probability for $rE_2 = E_3$ is now P_3. But we know $s_2 = s_G$, i.e., the signs of E_3 and E_4 are the same except the magnitude. We let $s_3 = s_G$ for the certainty of the sign and $W = (2P_3 - 1)$ for the uncertainty of the magnitude.

(2) $|gG|<|E|$. In this case (Fig. A-2), the sign of rE_2 is unknown relative to s_G but $s_E \cdot s_2$ ="-". Thus, for reflections in this category, the weight shall be assigned as:

(a) When $P_+ = 1$: In this case, $s_E = s_G$ and $rE_2 = E_3$. Since $s_E \cdot s_2$ = "-", we let $s_3 = -s_G$ and $W = 1$ for E_3.

(b) When $P_+ \neq 1$: In this case, we are not sure about the sign of E or rE_2 relative to s_G and neither of the magnitudes of rE_2 (it can be either E_3 or E_4). We let $W = (2P_3 - 1)^2$ for E_3 being equal to rE_2 in both sign ($s_3 = s_G$) and magnitude.

Reflections in categories (1.a) and (2.a) have values of $rE_2 = E_3$ and are in general very few in number; no attempt is made to find these reflections in the phase refinement. Reflections in category (1.b) are also of no interest because the sign of rE_2 is already known and the magnitude of rE_2 may be regarded as the same as E_3 with probability P_3 later in the E-map synthesis. Only reflections in category (2.b) which are large in magnitude for E_3 are of interest and are to be found in our phase refinement. The weighted Σ_2 formula may be given as:

$$s(E_{2\vec{h}}) \sim s\,(\Sigma_{\vec{k}}\, W_{\vec{k}} W_{\vec{h}-\vec{k}} E_{2\vec{k}} E_{2\vec{h}-\vec{k}}\,) \qquad (5.27)$$

where E_2's are rE_2 ($\equiv E_3$) and W's are weights for the corresponding reflections. The summation is over all available terms. The probability that the Σ_2 formula generates the correct result will be

$$P_w = \frac{1}{2} + \frac{1}{2}\tanh[Q\, E_{2\vec{h}} \Sigma_{\vec{k}} W_{\vec{k}} W_{\vec{h}-k}\, E_{2\vec{k}} E_{2\vec{h}-\vec{k}}\,] \qquad (5.28)$$

and

$$Q = 2q_3 q_2^{-3/2}. \qquad (5.29)$$

Thus, the new weight of the Σ_2 result is

$$W_w = (2P_w - 1)^2. \qquad (5.30)$$

Any resulting sign, $s(E_{\vec{h}})$, in (5.27) is compared with the sign of E_3, s_3, for the reflection $\vec{h}$. In case these signs are not equal, and if the new sign is more reliable (i.e. if $W_w > W$), then E_3 is replaced by E_4 for this reflection, and W_w is taken as its new weight.

Noncentrosymmetric case

For noncentrosymmetric structures phases are not restricted to 0 or π as in centrosymmetric structures. But the difference structure factors rE_2 in (5.24) can still have two extreme values E_3 and E_4 which are defined as

$$E_3 = (|gG| - |E|)\exp[i\gamma]$$
$$E_4 = (|gG| + |E|)\exp[i\gamma].$$

where γ is the phase of the structure factor G.

When E and G have the same phase, $rE_2 = E_3$. When E and G are completely out of phase, $rE_2 = E_4$. Note that

$$|E_3| \leq |rE_2| \leq |E_4|. \qquad (5.31)$$

In the following procedure use is made of those reflections where E_3 is far more probable than E_4, and E_3 is used as a first estimate of rE_2.

Analogous to the centrosymmetric case, we use P_3 as a measure for the relative probability of the phase of E_3:

$$P_3 = P(|E_3|)/\{P|E_3| + P(|E_4|)\}, \qquad (5.32)$$

where the distribution function for noncentrosymmetric reflections has the form of

$$P(|E|) = 2|E|\exp[-E^2]. \qquad (5.33)$$

According to van den Hark et al.[39] and Beurskens et al.,[40] the standard deviation δ_3 for the phase of E_3 can be calculated by the following equation:

$$\langle M \rangle = \int_{-\pi}^{+\pi} M \, P(\xi) d\xi \qquad (5.34)$$

where $M = \psi^2$, or $M = \cos\psi$ (ψ is the difference between the phases of rE_2 and G), or $M = |E_2|^2$; and $P(\xi)$ is defined in equation (3.13).

Since the distribution function (5.32) has a maximum at $|E| \simeq 0.7$, three distinct cases are to be considered (see Fig. A-3) for general noncentrosymmetric reflections. In Fig. A-3, it is seen that when $|E_3| < 0.7$, the value of $|E_3|$ is not the most probable value. The tangent formula cannot affect the phase of such a reflection. Thus, reflections belonging to cases (ii) and (iii) will not be considered in phase refinement. For case (i) both $|E_3|$ and $|E_4|$ are greater than 0.7. Many reflections fall in this category and $|E_3|$ is the more probable value. Therefore, we shall only concentrate on case (i).

The first estimate of $|rE_2|$ is E_3 with a probability P_3. The weight for this estimate is then $2P_3 - 1$. The weight of the phase of E_3 can be calculated by (5.34) with $M = \cos\psi$. Thus, the value of initial weight assigned to E_3 is

$$W = (2P_3 - 1) \langle \cos\psi \rangle \qquad (5.35)$$

where $\langle \cos\psi \rangle$ is the expectation value for $\cos\psi$. If the value of $\langle \cos\psi \rangle$ is not available, one can also use $(2P_3 - 1)^2$ as the weight W.

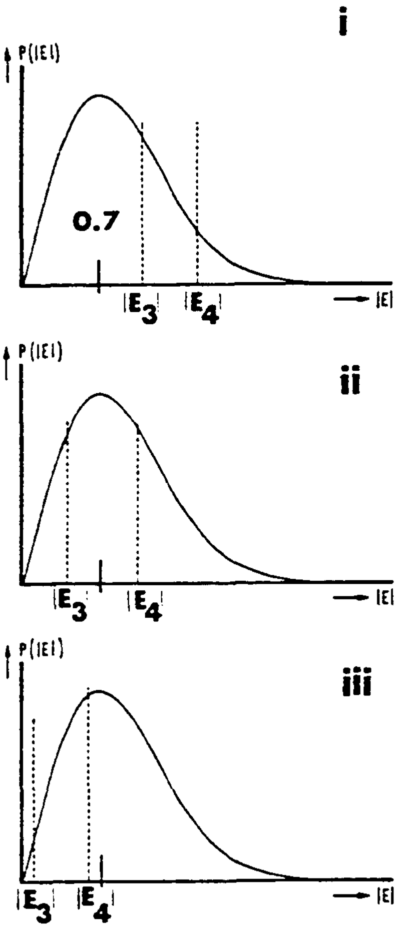

Fig. A-3 Classification of reflections depending on $|E_3|$ and $|E_4|$ pairs: (i) $|E_4|>|E_3|>0.7$, (ii) $|E_3|<0.7<|E_4|$, (iii) $|E_3|<|E_4|<0.7$.

The form of weighted tangent formula may be given as the same as that in (5.19). The strength of the new phase indication (see Fig. A-3) also has the same form as (5.20) except that the constant 2λ in (5.20) is replaced by Q which is defined in (5.29). Note that here the E's in (5.19) and (5.20) are difference structure factors rE_2. The new weight associated with the new phase can also be defined by (5.22) or (5.23) with 2λ being replaced by Q.

New phase angles and weights will replace the old ones if the value of the new weight exceeds that of the original one. If so, the new estimate of $|rE_2|$ can be recalculated according to the following equation:

$$|E| = |\, gG - |rE_2|\exp[i\alpha_2] \,| \qquad (5.36)$$

where α_2 is the phase of rE_2.

CHAPTER 6. IMPROVEMENT OF PATTERSON SUPERPOSITION FUNCTIONS

Introduction

In the previous chapters only "well-behaved" Patterson superposition functions have been mentioned, that is those which multiply all electron density by an approximation of the electron density and have false peaks only where there is insignificant electron density. The Fourier coefficients G of such functions are thus expected to possess all the effective phase-determining properties as described in Chapters 3 and 4. In practice, however, because of lack of atomic resolution, some of the real atoms are buried in the background or are even missing from the Patterson superposition function. It is then hardly true that atoms which simultaneously belong to one image could all contribute to the Fourier coefficients G. In addition, due to peak overlap, the height of the maxima in the function are not a good approximation to the scattering power of the corresponding atoms. Therefore, the Fourier coefficients of a real Patterson superposition function are "worse" than those one can expect from the theory.

It has been found that phase determination deteriorated as the quantity of the Patterson superposition functions deteriorated. The amount of deterioration depends upon the completeness of a desired image in the function. Nonetheless, the phase-determining power in the G's often still remains if a significant portion of the scattering strength from a consistent image is available. Therefore, the success in obtaining a reasonably good Patterson superposition function is one of the critical steps toward obtaining successful solutions using our hybrid approach.

Patterson superposition functions may be obtained by applying three kinds of simple image-seeking functions[3] to Patterson functions: the sum function, the product function, and the minimum function. The sum function is a poor image-seeking function because it finds not only the desired electron density, but also a considerable amount of unwanted density.[41] The product function has a tendency to exhibit somewhat excessive background and thus is ordinarily non-zero everywhere. The minimum function has proven to be the best behaved of the three image-seeking functions.[42] Thus, in this thesis, all of the Patterson superposition functions were constructed by the use of the minimum function except where stated.

The improvement of Patterson superposition functions in this research, if necessary, will be done solely on the images found in the functions themselves rather than the methods used to obtain the image-seeking function. Three methods of improvement are proposed. The first method is called superpositional synthesis[43] (SS). This method is designed to automatically construct a better approximation to the electron density distribution in the crystal from a Patterson superposition function. The second method is called difference synthesis (DS) which enables one to directly eliminate false maxima from Patterson superposition functions. These two methods require the incorporation of symmetry. The third method is called consecutive superpositions (CS). It makes use of both the Patterson and its superposition maps to generate another superposition function which should be exactly the same as that obtained from two superpositions using two distinct displacement vectors. This method does not require any prior symmetry information and thus may be particularly useful for structures which are of P1 symmetry.

Superpositional Synthesis

It has been mentioned that due to lack of atomic resolution, real atoms may be lost on the Patterson superposition functions. If one can somehow uncover these missing atoms or perhaps suppress some of the false maxima, a better approximation of the electron distribution may be obtained from this function.

In the SS method, the originally obtained minimum function is first "refined" by a symmetry analysis. The purpose of this analysis is twofold. First, the unit cell origin might be identified (in all three dimensions if possible). This enables the origin of the Patterson superposition map to be brought into correspondence with that of the unit cell. Second, a systematic search for pairs of vector peaks which satisfy the space group symmetry is performed. This procedure allows the extraneous peaks or images which do not correspond to the required symmetries to be filtered out. Only these potential atom peaks left on the map after the symmetry analysis will be included in the computation of the pseudo-normalized structure factors G.

The next step in the SS method is to form appropriate Fourier coefficients for the β-synthesis[44] or the γ′-synthesis[42] (see Table A-6). Either one of these two Fourier syntheses can be carried out to give a second refinement of the minimum function. This function is again modified by the symmetry analysis mentioned above and the resultant Fourier coefficients will be input to another cycle of the Fourier β- or γ′-synthesis when necessary.

The Fourier synthesis part of the SS method proposed here is similar to that of Simonov's[10] except that in addition to the γ′-synthesis, the β-synthesis is also adopted. In Simonov's procedure, it was found that the false peaks on the minimum function were partially eliminated by the use of $|F_{obs}|$. In theory, however, the γ′-synthesis is not as effective in eliminating false peaks as is the β-synthesis. In addition, the β-synthesis is also more effective in uncovering the missing (or unknown) atoms.

The basic theory of the β-synthesis involving the pseudo-structure factors G is discussed below.

Notation

F_n = structure factor of the complete structure

F_p = structure factor of real atoms on Patterson superposition function

F_q = structure factor of extraneous atoms on Patterson superposition function

F_x = structure factor of real atoms which are missing on Patterson superposition function

$G \simeq F_p + F_q$

α, γ = phases of F_n and G respectively

f_n, f_p, f_q, f_x = scattering factors of the n,p,q, and x atoms

Σ_n = sum of $(f_{n,i}{}^2)$, similarly for Σ_p, Σ_q, and Σ_x

$$d = \frac{\Sigma_p}{\Sigma_n}, \quad \varepsilon = \frac{\Sigma_p}{\Sigma_p + \Sigma_q}$$

r_p, r_q, r_x = positions of the p,q,x atoms

The Fourier β-synthesis

The Fourier coefficients of a regular β-synthesis are $|F_n|^2/F_p^*$, where $F_p^* \equiv$ complex conjugate of F_p. In our case, since the structure factors G include contributions of false peaks, we shall consider the β-synthesis with false atoms. That is, the Fourier coefficients become

$$|F_n|^2/G^*. \tag{6.1}$$

Kalyanaraman et al.[45] have investigated the effect of including wrong atoms in the β-synthesis and their results are implemented here.

Using the relationship

$$F_n = F_p + F_x, \qquad (6.2)$$

the Fourier coefficients of the β-synthesis are now

$$\frac{|F_n|^2}{G^*} = F_p + F_x + \frac{1}{G^*}(F_pF_x^* + |F_x|^2 - F_pF_q^* - F_xF_q^*). \qquad (6.3)$$

The peaks in this synthesis can be obtained by taking the Fourier transform of each of the terms in (6.3). The strength of the peaks at the sites of p,x, and q atoms are shown in Table A-6. It can be seen that in the β-synthesis, the missing atoms (type x) can be uncovered with a strength of εf_x. The peaks of false atoms (type q) are considerably suppressed such that they reappear with less than half heights.

It was mentioned that the γ′-synthesis is not as effective as β-synthesis in both uncovering new atoms and suppressing false ones. This can be illustrated by Main's work.[46] He has investigated weighted γ′-synthesis in which wrongly positioned atoms were involved. In this synthesis, each Fourier coefficient is weighted by ω as defined by Sim.[47] For comparison, some of his results are also listed in Table A-6. It can be seen that new atom peaks (type x) in the γ′-synthesis appear only with half strength compared to the

Table A-6. The strength of peaks in the β-synthesis and the weighted γ'-synthesis

Synthesis	Fourier coefficient	Atom type	Noncentrosymmetric peak strength	Centrosymmetric peak strength
β	$\frac{\lvert F_n \rvert^2}{G^*}$	p	$(\varepsilon/d)f_p$	$(\varepsilon/d)f_p$
		x	εf_x	$2\varepsilon f_x$
		q	$(1-d)\varepsilon f_q/d$	$(1-2d)\varepsilon f_q/d$
γ'	$\lvert F_n \rvert \omega e^{i\gamma}$	p	f_p	$(1+\varepsilon)f_p/2$
		x	$\varepsilon f_x/2$	εf_x
		q	$(1-\varepsilon/2)f_q$	$[(1-\varepsilon)/2]f_q$

β-synthesis and false atoms always reappear in the γ'-synthesis with at least half of the original strength.

Difference Synthesis

It has been shown in Chapter 3 that the probabilities that the phases of the G's are true are essentially governed by the factor

$$\frac{(\sigma_2\sigma_2')^{1/2}}{\sigma_2' - \sigma_2} \sim \frac{(NM)^{1/2}}{M - N} \tag{6.4}$$

for both centro- and noncentro-symmetric structures when the value of the product $|E||G|$ is constant. The term on the right side is an approximation which becomes exact if all atoms are equal. The larger the value of (6.4), the more likely that the phases of the G's are in the vicinity of true value.

It can be seen that the value of (6.4) is more sensitive to the change of the denominator. In order to keep the value of the denominator as small as possible, one should thus try to eliminate as many false peaks on the Patterson superposition function as possible. It is well known that a false peak will appear on the minimum function if a displacement vector equals the difference between two arbitrary Patterson vectors which take no part in the building up of the image of the structure. That is, when the condition[10]

$$r_{hp} = r_{kl} - r_{mn} + R \tag{6.5}$$

(where $r_{ij}=r_j-r_i$, R = θ1*a + θ2*b + θ3*c, a,b,c are the unit cell axes, and θ1,θ2, θ3 are integers) holds, false peaks on the minimum functions will always appear even if no peaks overlap on the Patterson map.

To detect these false peaks, the DS method can be very useful. In this method, a preliminary refinement of the minimum function by a symmetry analysis, which was mentioned in the previous section, is used. A further refinement can then be achieved by a weighted Fourier difference synthesis. The result of this synthesis should disclose all possible extraneous peaks on the first refined Patterson superposition function.

The basic theory of this method was originally developed by Woolfson[30] who applied it to heavy-atom structures. Now it has been modified to include the pseudo-normalized structure factors. The principle of this method is briefly illustrated in the following.

Centrosymmetric case

The equations (3.7) and (3.8) derived in Chapter 3 can be used to predict the probability that E has the same sign as or opposite sign to G, respectively. These two equations can also be used to obtain the average value of E_2 which is the contribution of the (M-N) extraneous atoms to the structure factors G as mentioned in the previous sections. The average value of E_2 for a given pair of values of $|G|$ and $|E|$ is then given by

$$s_G(|gG| - |E|)P_+(GE)/r + s_G(|gG| + |E|)P_-(GE)/r,$$

or

$$\overline{\sum_{j=N+1}^{M} Z_j \cos(\vec{h}.\vec{r}_j)} = s_G[|gG| - |E|\tanh\{\frac{|gG||E|}{r^2}\}]/r,$$

where $g = (\frac{\sigma_2'}{\sigma_2})^{1/2}$ and $r = (\frac{\sigma_2' - \sigma_2}{\sigma_2})^{1/2}$.

It can be seen that the quantity

$$s_G[|gG| - |E|\tanh\{\frac{|gG||E|}{r^2}\}]/r \qquad (6.6)$$

is now playing the same role, in a statistical sense, for the (M-N) "extraneous atoms" as G would normally play for all M atoms.

Therefore, using this quantity (6.6) as the Fourier coefficient, an electron density map may be calculated which contains only the group of (M-N) extraneous atoms. This Fourier synthesis closely resembles a weighted difference synthesis, i.e., the sign of G is adopted and each structure amplitude $|E|$ is weighted by a factor, $(2P_+ - 1)$ (where P_+ was given in equation (3.7)), which has a value between 0 and 1. When it is uncertain that G and E have the same sign the weighting factor is very small, and as the probability that G and E have the same sign increases, so does the weighting factor.

Noncentrosymmetric case

A similar treatment can be made for noncentrosymmetric structures. The Fourier coefficients would be

$$\{|gG| - [\ 2P(\xi) - 1]|E|\}\exp(i\gamma), \qquad (6.7)$$

where $P(\xi)$ was defined in (3.15) and the value of ξ is usually chosen as 90°. The term of $2P(\xi) - 1$ is a weighting factor: when X (in equation (3.13)) is small, $|\alpha - \gamma|$ is likely to be large and $2P(90°) - 1$ approaches 0 (see Table A-3), and when X is large, $|\alpha - \gamma|$ is likely to be small and $2P(90°) - 1$ approaches unity. Therefore, using the quantity (6.7) as the Fourier coefficient, an electron density map can also be calculated and in which contains only the group of (M-N) extraneous atoms.

The Patterson superposition function is then modified by taking out all the extraneous peaks obtained from the above difference synthesis. New Fourier coefficients G of this function may be calculated and input to another cycle of difference synthesis, if necessary, to obtained better "refined" Patterson superposition functions.

Consecutive Superpositions

The method of consecutive superpositions is a numerical approach for deconvoluting Patterson superposition functions. A Patterson map, its minimum function, and the displacement vector used are required in this CS method. Symmetry operations, bond distances, and other chemical information may be useful but are not required. The basic principle of this method is illustrated as follows:

It is known that on the Patterson function, the peaks are representations of interatomic vectors. In general, each of the Patterson peaks belongs to the vector set $\{A_i-A_j\}$, where A_i and A_j represent the vectors from a conventionally chosen origin to the ith and jth atom, respectively. A Patterson superposition (PS) map is obtained by displacing a second copy of the Patterson map (PM) relative to the first one by a vector, say A_2-A_3 (= SV), and then placed on top of the first map. The determination of the overlapping peaks between the two maps is equivalent to looking for a common set of vectors between the two vector sets, $\{A_i-A_j\}$ and $\{A_i-A_j+A_2-A_3\}$. As a result, on the PS, only those vectors which are of the type of $\{A_2-A_j\}$ and $\{A_i-A_3\}$ exist. These vectors represent a mixture of two images if A_2-A_3 is a single vector, four images if A_2-A_3 is a double vector and six images if A_2-A_3 is a triple vector, etc.

Let us now consider the characteristics of the overlapping pairs of vectors. For a vector A_2-A_j on the PM to be overlapped with a vector on the shifted Patterson map (SM), the vector on the SM must be equivalent to A_3-A_j+SV. Similarly, the vector A_i-A_3 on PM needs a vector A_i-A_2+SV on the SM to overlap. This means that if a vector, say V1, on the PM remains after a superposition by a shift vector SV, there is always a vector, say V2, existing on the PM where V1-V2 = SV. On the other hand, the images $\{A_i-A_3\}$ and $\{A_2-A_j\}$ are inversion related to each other by the displacement vector SV, A_2-A_3. Thus, if there is a V1 existing on the superposition map, there is always a vector, say V3, where V3 = SV-V1, on this map, too. After some rearrangement, it is easily seen that the vectors V2 and V3 are inversely related to each other.

Similarly because V3 appears on the superposition map, there must exist another vector, say V4, where V3-V4 = SV on the PM. Again V1 and V4 are found to be inversely related to each other. Thus, these four vectors immediately form a "quartet" relation; it is:

$$\begin{aligned} V1 &\longrightarrow V2(=-V3) \\ V3 &\longrightarrow V4(=-V1) \\ \text{or} \quad V1 &+ V2 + V3 + V4 = 0. \end{aligned} \tag{6.7}$$

The use of this quartet relation is the key to the CS method. Consider that a superposition map is obtained in a usual fashion.[24] By searching for the pair of vectors generating the superposition peaks, tens or hundreds of quartets can be formed. Ideally, the actual number of the quartets should be less than the number of atoms in an individual image by m, where m is equal to the multiplicity of the displacement vector. What can we learn from these quartets?

Remember that if V1 is A_i-A_3, V2 must be A_i-A_2, V3 must be A_2-A_i, and V4 must be A_3-A_i. Assuming that i=1, and A_1 is placed at the origin, then the positions of A_2 and A_3 can be calculated from V1 and V2 in the quartet. On the other hand, A_2 and A_3 can also be derived from V3 and V4. There is no difference between the solutions from (V1,V2) or (V3,V4) except when the absolute configuration of the structure is concerned. The rest of the quartets each containing two pair of the vector peaks: (A_x-A_3,A_x-A_2) and (A_2-A_x,A_3-A_x) where x ranges from 4 to n (the number of atoms in the unit cell) are then analyized by substituting the coordinates of A_3 and A_2 into each pair. Only one pair should yield the correct position of A_x. As more quartets are analyzed, more atomic positions are obtained. Finally, a complete image whose origin corresponds to atom A_1 is formed.

A summary of the analysis procedures is given below:

(1) Use the displacement vector to generate a superposition map and find all possible "quartets".

(2) Among the quartets, pick one quartet as a starting one and then generate coordinates for A_2 and A_3 (always assume the atoms forming this quartet are A_1,

A_2 and A_3).

(3) Calculate possible atomic coordinates from the rest of the quartets. Each calculated atomic position will be checked to see if it exists on the PM. If not it is discarded.

(4) Internal consistency of the interatomic vectors is checked among atoms A_4 through A_n yielding a final solution.

The solution obtained from the above procedure primarily contains an image whose origin is placed at atom A_1. This image is equivalent to a Patterson superposition function which is obtained from two consecutive superpositions using A_2-A_1 and A_3-A_1 as displacement vectors.

CHAPTER 7. RESULTS AND DISCUSSIONS

Most of the theoretical developments mentioned in the previous chapters have been tested using either model or real structures. Test procedures, results and discussions are presented in this chapter.

Examination of the Σ_2-like Relation

The validity of our Σ_2-like relation (or the E-G relation), equation (2.18), has been investigated using known structures. Our intention was to understand how well the E-G relation would hold, i.e., with known phases of the E's, how much of the phase correction in the G's can be made by applying this E-G relation? Both centro- and noncentrosymmetric cases were studied. For centrosymmetric structures, the phases are either 0 or π and thus the percentage of correct signs was used to determine the efficiency of the E-G relation. For noncentrosymmetric structures, because the phase angle is an arbitrary number between $-\pi$ and $+\pi$, the value of mean phase-angle error was used.

Tests were performed on three structures: CA, FSA and CR. Their compositions and some crystal data are listed in Table A-7. Both CA and CR are real structures and their Patterson superposition functions were generated from their observed intensity data. FSA is a model structure and its Patterson

Table A-7. List of test structures

Name	Formula	no. indep. atoms	no. indep. reflections	space gr. symmetry
CA	$Ca_{5.45}Mo_{18}O_{32}$[a]	15	569	C2/m
FS	FeS_3OC_8[b]	13	1167	PI
FSA	$[FeS_3OC_8]_2$[c]	26	1167	P1
CR	$Cr[C_6H_8N_3O_2]_2NO_3$[d]	27	1523	$P2_1$
IN	$InMo_4O_6$[e]	5	154	P4/mbm

[a] See reference 48.

[b] See reference 49.

[c] See text (p. 87) for detail.

[d] See reference 50.

[e] See reference 51.

superposition function was artificially generated from the coordinates of two structural images displaced relative to each other. For simplicity, all the structures were assumed to correspond to point-atom cases and their normalized structure factors E were obtained by using equation (2.7).

Centrosymmetric case

CA is a very complicated structure. It contained so many parallel vectors that most of the peaks which could be distinguished from background on the Patterson map were highly overlapped. For instance, the peak of a single Mo-Mo vector should have a height ~4.9% of the origin peak. However, peaks which had this height were hardly distinguished from the background. Finally a vector which had a height of ~16% of the origin peak was selected to generate a Patterson superposition map. This vector was later analyzed as a composite of 20 overlapping peaks: two vectors of Mo-Mo, 2 vectors of Mo-O, four vectors of Ca-O and 12 vectors of O-O. Thus, on the Patterson superposition map, there were many images overlapped on each other.

From this superposition map 150 peaks, or about 2.5 times the number of atoms in a unit cell, were selected and the Fourier coefficients G were obtained by using the equation

$$G_{\vec{h}} = 2 \sum_j (HT)_j^{1/2} \cos\vec{h}.\vec{r}_j \Big/ \sum_j (HT)_j, \qquad (7.1)$$

where HT is the peak height[52] and its square root was taken as an approximation to the atomic scattering factor at zero Bragg angle.[53]

The signs of the G's were then compared with those of the E's. The percentage of incorrect signs as functions of $|E|$ and $|G|$ are listed in Table A-8. For example, among the total of 569 reflections, there were 90 whose values in both $|E|$ and corresponding $|G|$ were greater than 1.5 and of these only 4.5% had incorrect signs. Overall, there were 66% of the structure factors G whose signs were correct.

It was mentioned in both Chapters 3 and 5 that according to equation (3.1) when both the E's and the corresponding G's were large in magnitude, the phases of the G's could be taken as those of the E's. One now can observe this fact in Table A-8. The value in this table can also be referred to as the "level of sign transferability". For example, the sign transferability can be considered as 100% when $|E| \geq 1.5$ and $|G| \geq 2.25$ are chosen as limiting values.

Now when both the E's and the G's are known in sign, two questions are to be answered: First, can wrong sign indication from the G's be corrected by applying the E-G relation? Second, will the E-G relation hold when only a few reflections whose $|E|$'s and corresponding $|G|$'s are large in magnitude are included in the summation?

To answer the first question, the new sign for each of the reflections whose sign of the G was different from that of the E was recalculated using the E-G relation, equation

Table A-8. Wrong-sign[a] distribution (%) as functions of |G| and |E| based on 569 reflections of the structure CA

E \ G	2.50	2.25	2.00	1.75	1.50	1.00	0.50	0.00
2.25	0.0	0.0	0.0	0.0	0.0	3.5	5.8	5.7
2.00	0.0	0.0	4.4	3.4	3.0	4.9	6.0	10.7
1.75	0.0	0.0	4.3	3.2	5.1	6.2	9.3	13.9
1.50	0.0	0.0	4.0	2.9	4.5	5.2	10.7	16.7
1.00	0.0	2.4	4.8	4.9	5.6	7.4	16.9	25.8
0.50	0.0	4.2	5.8	5.7	6.0	11.1	22.8	31.3
0.00	0.0	4.0	5.6	6.6	8.7	15.0	26.8	34.1

[a] The phase angles of the G's were not exactly 0 or π due to the fact that no inversion symmetry was included in the calculation of the structure factors. However, when the absolute value of the phase angle was less than 90°, the sign was regarded as "+". Otherwise, the sign was regarded as "-".

(2.18). Some of the results are shown in Table A-9. In this table, the first column gives the reflection code. The magnitudes of the E's and the G's are listed in the second column. The number of sigma two relationships (s2rs) which were included in the summation is listed in the third column. α is the phase angle of the E and γ is the phase angle of the G. (Note that the value of γ was not exactly 0 or 180° here. This was due to the fact that no inversion symmetry was included in the calculation of the G's. However, these values were only slightly off "0" or "180" and thus the "sign" of each structure factor amplitude could still be easily identified.) α' is the new phase angle calculated by using the E-G relation in which all possible s2rs among the 569 reflections were included with unit weight. Among 192 wrong signs, 140 became correct. This result definitely suggests a positive answer to the first question.

To answer the second question, only those s2rs in which both $|E|$ and $|G|$ values greater than 1.5 were included with unit weight in the E-G relation to obtain new phase angles α''. The results are shown in the last two columns in Table A-9. The number of s2rs used in obtaining α'' was significantly less than those used in the calculation of α'. But among 192 wrong signs, only 28 (~5%) remained incorrect after applying the E-G relation. This result seemed better than those in which all the s2rs were used in the E-G relation. Therefore, the answer to the second question is

Table A-9. The results obtained by using the E-G relation for the real structure CA

code	$\|E\|(\|G\|)$	#s2rs	$\alpha(°)^a$	$\gamma(°)$	$\alpha'(°)$	#s2rs	$\alpha''(°)$
1	2.50(1.04)	152	0.	-180.	-2.	12	1.
2	2.48(0.63)	150	0.	179.	-2.	12	1.
3	2.25(0.09)	212	0.	154.	-7.	19	0.
4	2.14(0.34)	202	180.	7.	-150.	24	180.
5	2.08(2.05)	244	0.	178.	3.	23	-3.
6	1.99(0.59)	178	0.	175.	5.	19	0.
7	2.00(0.07)	354	0.	45.	-6.	33	0.
8	1.84(0.12)	450	0.	169.	2.	30	0.
9	1.79(0.98)	231	0.	176.	-10.	15	0.
10	1.75(0.07)	250	180.	-46.	157.	25	180.
11	1.74(0.64)	266	0.	-178.	84.	18	-1.
12	1.64(0.23)	203	180.	19.	173.	20	0.
13	1.63(0.80)	293	180.	4.	-176.	21	180.
14	1.61(0.97)	271	0.	-179.	-4.	26	0.
15	1.61(0.37)	172	0.	-177.	1.	13	0.
16	1.53(0.35)	264	0.	168.	-10.	24	0.
17	1.51(0.68)	262	180.	5.	-175.	29	180.
18	1.50(0.43)	284	0.	173.	0.	17	-1.
19	1.48(0.11)	70	0.	-169.	56.	3	0.
20	1.48(0.77)	261	0.	177.	-13.	22	5.
21	1.47(1.26)	111	0.	177.	-7.	9	0.
22	1.46(0.29)	197	180.	8.	158.	19	-1.
23	1.46(0.10)	97	180.	88.	-126.	6	180.
24	1.45(0.28)	289	0.	170.	1.	14	0.
25	1.44(0.94)	270	0.	179.	-14.	18	0.
26	1.44(0.85)	217	0.	180.	4.	22	0.
27	1.42(0.14)	169	0.	-178.	-31.	8	0.
28	1.43(1.29)	216	0.	-179.	6.	18	1.
29	1.40(0.65)	283	0.	-177.	-7.	14	2.
30	1.39(0.12)	191	0.	166.	2.	11	0.
31	1.40(0.65)	174	0.	-177.	18.	7	0.
32	1.38(0.81)	204	180.	5.	-163.	20	179.
33	1.37(0.07)	89	180.	-50.	108.	6	180.
34	1.36(0.31)	219	0.	167.	2.	18	0.
35	1.33(0.16)	447	0.	-168.	-4.	30	1.

---

[a] α is the phase angle of E, γ is the phase angle of G, α' is the new phase angle calculated by using the E-G relation in which all possible sigma-two relationships were included, and α'' is the new phase angle calculated by using the E-G relation in which only those s2rs with $|E|\geq 1.5$ and $|G|\geq 1.5$ were included.

Table A-9 (continued)

36	1.29(0.64)	229	180.	4.	164.	13	180.
37	1.24(0.53)	75	0.	177.	-15.	1	0.
38	1.24(1.27)	225	0.	177.	-8.	12	-1.
39	1.24(0.85)	114	0.	179.	4.	8	1.
40	1.22(0.82)	253	180.	0.	-170.	25	180.
41	1.19(0.19)	169	180.	11.	167.	6	180.
42	1.18(0.09)	356	180.	-9.	70.	24	-179.
43	1.18(0.43)	202	0.	178.	-9.	22	-2.
44	1.16(2.25)	79	0.	-179.	91.	7	1.
45	1.13(0.29)	399	0.	-171.	4.	25	1.
46	1.10(0.15)	275	180.	29.	178.	19	180.
47	1.11(0.42)	112	180.	13.	-157.	3	179.
48	1.07(1.98)	230	180.	1.	-177.	21	180.
49	1.05(0.75)	348	0.	-178.	-8.	21	1.
50	1.04(0.30)	214	0.	-177.	-177.	21	176.
51	1.05(0.75)	162	0.	-178.	-164.	9	173.
52	1.03(0.19)	147	180.	-13.	142.	8	2.
53	1.03(0.50)	195	180.	1.	-90.	18	180.
54	1.01(0.84)	125	0.	179.	-153.	10	-5.
55	1.01(0.69)	152	0.	179.	38.	12	-2.
56	1.01(0.13)	199	180.	-8.	142.	14	180.
57	0.99(0.12)	212	180.	5.	-169.	16	-179.
58	0.99(0.27)	156	180.	1.	17.	16	-179.
59	0.97(0.76)	373	0.	176.	3.	23	-7.
60	0.96(0.45)	297	180.	3.	156.	19	-179.
61	0.95(0.05)	187	0.	-101.	11.	14	3.
62	0.94(0.96)	333	0.	176.	-59.	21	-1.
63	0.89(0.38)	188	0.	169.	-10.	15	-1.
64	0.88(0.34)	408	0.	-176.	-6.	20	174.
65	0.85(0.69)	345	180.	-1.	-152.	22	0.
66	0.85(1.07)	66	0.	-179.	-4.	4	1.
67	0.84(1.24)	358	180.	-1.	150.	25	180.
68	0.85(0.73)	178	0.	-179.	-6.	13	3.
79	0.85(1.07)	314	0.	-179.	1.	17	1.
70	0.82(0.78)	105	180.	-4.	88.	8	3.
71	0.81(0.96)	462	180.	2.	160.	43	180.
72	0.73(1.07)	286	180.	2.	172.	19	179.
73	0.68(1.23)	160	180.	1.	8.	12	179.
74	0.60(0.71)	309	0.	176.	-18.	18	0.

also affirmative.

Noncentrosymmetric case

The E-G relation has been applied to two noncentrosymmetric cases. In the first case, the Patterson superposition function of a model structure, FSA, was designed to contain two complete structural images which were enantiomorphic to each other. This two-image function is usually difficult to resolve into two individual images unless a fragment of the structure is known. In the second case, two different Patterson superposition functions of a real structure, CR, were constructed by two different displacement vectors. One was a Harker vector of two-fold screw axis, which would usually result in images related by pseudo-symmetry, and the other one was a double Cr-O vector. Thus, on the Patterson superposition maps, there existed several images which could not be distinguished from their enantiomorphs. This CR structure was first solved by the heavy-atom method only with great difficulty since it is not a typical heavy-atom structure ($Z_h^2/\Sigma Z_l^2 \simeq 0.5$). MULTAN[12] failed to give a correct solution. This was not unexpected[54] since the direct methods usually encounter trouble with low symmetry, in this case $P2_1$.

The effectiveness of the E-G relation on these two acentric cases was shown in terms of the mean phase-angle error. For the real structure CR, electron density maps were also constructed so that a direct comparison of the results in real space could be made between different phase solutions.

Test results for structure FSA The model structure FSA (see Table A-7 for details) had P1 symmetry and was derived from the centrosymmetric structure, FeS_3OC_8 (also see Table A-7), of space group PI by shifting the origin away from the center of symmetry. A hypothetical Patterson superposition map was constructed such that two images, which were inversely related to each other through the origin, existes on the map. The Fourier coefficients G of this Patterson superposition function were calculated by using equation (2.11.1). The mean errors of phase angles in the G's as functions of both $|E|$ and $|G|$ are listed in Table A-10. The values of phase-angle errors shown in this table are surprisingly not large. When compared with some of MULTAN results,[55] these values of phase-angle errors could still yield a structural solution. This is true because the G's indeed contained valid structural information, although in this case the phase angles of the G's could not adequately define a single enantiomorph.

Three questions were studied:

1. Does the E-G relation, (2.18), hold when a large number of reflections are included?
2. Will the E-G relation hold when only a limited number of reflections are used?
3. Will the E-G relation hold when only a few large

Table A-10. Mean phase-angle error (°) (based on 1167 reflections) as functions of |G|[a] and |E| for the structure FSA

E \ G	2.50	2.25	2.00	1.75	1.50	1.00	0.50	0.00
2.25	32.2	32.2	32.2	32.2	32.2	32.2	32.2	50.3
2.00	25.1	25.1	25.1	25.1	25.1	30.4	30.4	36.0
1.75	22.5	25.4	26.0	26.6	28.1	29.7	31.4	32.4
1.50	22.1	25.1	27.3	29.5	30.6	32.4	34.9	36.1
1.00	18.4	19.8	21.8	24.6	27.0	30.6	33.4	34.8
0.50	18.4	19.8	21.8	23.1	24.7	28.2	32.8	35.6
0.00	18.4	19.8	21.8	23.1	24.7	28.2	32.4	35.8

[a] The G's were calculated from a hypothetical Patterson superposition function on which two complete images enantiomorphic to each other existed.

reflections are used?

To answer these questions, a group of 41 reflections in which the E's and the corresponding G's varied in magnitude were selected. To answer question (1), all sigma-two relationships (s2rs) from the 1167 reflections for each of these reflections were found. New phase angles calculated from the E-G relation are denoted by α'. Four different weighting functions were tried and the results are listed in Table A-11. In this table, the first column contains the code number for each of the 41 reflections. Values of $|E|$ and corresponding $|G|$ of each reflection are given in the second column. The number of s2rs included in the calculation of the new phase angle α' is given in column 3. Deviations in the phase angles of the G's, $(\alpha - \gamma)$, are listed in the fourth column. The phase differences between $\alpha' - \alpha$, and $\alpha' - \beta$ (β being the phase angle of the squared structure) are listed in the next two columns. The column on the extreme right lists the phase difference between those phase angles calculated from Sayre's Σ_2 relation (the E-E relation), (2.3), and the correct phase angles.

Before phases were corrected by using the E-G relation, (2.18), the mean phase-angle error was 32.4°. However, this figure significantly decreased after applying the E-G relation (see the last row in Table A-11). With unit weight, the error was about 17.1° while with other weighting functions, the mean

Table A-11. The results of E-G relation for the structure FSA when a large number of sigma-two relationships are included in the summation

				Wt^a=1		Wt=|EG|		Wt=|G|		Wt=$\|G\|^2$		Δ^c
#	|E|(|G|)	#s2rs	$\alpha^b-\gamma$	$\alpha'-\alpha$	$\alpha'-\beta$	$\alpha'-\alpha$	$\alpha'-\beta$	$\alpha'-\alpha$	$\alpha'-\beta$	$\alpha'-\alpha$	$\alpha'-\beta$	
1	2.39(0.30)	497	87	19	7	15	3	17	5	17	5	14
2	2.27(3.11)	333	47	-15	-12	-11	-8	-12	-9	-10	-8	-3
3	2.21(1.32)	788	-73	2	7	4	8	4	9	4	9	-4
4	2.17(4.25)	531	11	-5	-5	-4	-4	-4	-4	-3	-3	-3
5	2.07(4.07)	1001	-11	-7	-6	-3	-2	-4	-3	-2	-2	-1
6	1.99(0.96)	563	-76	25	16	20	11	22	13	19	10	12
7	1.98(2.26)	475	55	-5	-12	-9	-16	-8	-15	-9	-16	8
8	1.97(3.54)	419	-26	11	14	8	11	8	10	5	8	0
9	1.96(3.38)	632	30	1	-6	-2	-8	-2	-8	-3	-9	7
10	1.95(3.90)	440	-2	4	-2	3	-3	3	-4	1	-5	4
11	1.95(0.89)	832	-77	4	5	5	5	5	7	7	8	-2
12	1.94(2.91)	526	-41	26	17	21	12	21	12	19	10	12
13	1.92(3.65)	456	18	-8	-10	-5	-7	-6	-8	-4	-6	0
14	1.89(3.57)	492	-19	13	8	12	8	12	8	11	7	5
15	1.84(3.10)	472	33	15	-10	8	17	10	-14	8	-17	27
16	1.79(1.50)	779	65	-39	-19	32	13	-33	-14	-31	-11	-22
17	1.77(1.88)	772	58	8	15	6	13	7	13	5	12	-6
18	1.73(0.82)	690	76	-40	-20	37	17	-38	-18	-36	-17	-26
19	1.72(0.50)	660	-82	11	8	9	6	11	8	10	7	5
20	1.70(2.85)	557	33	-20	-13	-16	-10	-17	-10	-15	-8	-10
21	1.63(3.26)	512	2	7	-4	7	-4	7	-5	7	-4	10
22	1.61(0.23)	556	-86	21	11	13	3	16	6	13	3	11
23	1.59(0.88)	592	74	3	-3	-2	-8	-1	-6	-3	-8	8
24	1.56(2.82)	453	25	-3	-19	-4	-19	-3	-18	-3	-18	12
25	1.54(2.87)	466	21	-11	-16	-9	-4	-10	-5	-9	-4	-6

26	1.50(1.01)	777	-70	1	6	1	6	3	8	4	9	-4
27	1.47(2.90)	754	-9	-3	8	-3	8	-3	8	-3	8	-8
28	1.42(2.83)	513	-5	10	-3	11	-1	11	-2	11	-2	12
29	1.36(2.71)	358	-1	-2	-1	-1	0	-1	0	-1	0	-4
30	1.31(2.48)	570	19	-6	-7	-2	-3	-4	-5	-3	-4	-2
31	1.23(2.45)	365	-4	3	9	3	10	2	8	1	8	-5
32	1.17(2.33)	441	-4	-12	8	-9	10	-10	9	-9	10	-21
33	1.11(2.16)	647	13	-23	3	-16	9	-17	8	-16	10	-23
34	1.04(2.07)	420	1	3	-2	2	-4	2	-4	1	-5	6
35	1.00(2.00)	748	4	-15	10	-11	13	-12	12	-12	12	-19
36	0.93(1.87)	568	-2	1	3	0	2	-1	1	-2	0	-3
37	0.90(1.71)	652	-18	-4	0	0	5	0	5	3	8	-3
38	0.79(1.56)	588	-9	47	-10	39	-18	38	-19	34	-23	60
39	0.71(1.37)	475	-14	15	5	11	2	12	3	12	2	12
40	0.66(1.28)	731	15	12	-5	7	-10	7	-10	3	-14	17
41	0.59(1.15)	628	12	-3	-9	-1	-7	-1	-6	2	-3	-1
mean phase error:			32	17	8	9	8	10	8	9	8	11

[a] Wt respresents weighting function.

[b] α is the phase angle of E, γ is the phase angle of G, β is the phase angle of V (the squared structure, see p.10), and α' is the new phase angle of E calculated from the E-G relation, (2.18).

[c] $\Delta = \langle\alpha\rangle - \alpha$, where $\langle\alpha\rangle$ is the new phase angle of E estimated from Sayre's E-E relation.

errors were about the same or even slightly better than those calculated from the E-E relation. Therefore, the answer to question (1) is affirmative.

The phase angles estimated from Sayre's E-E relation can be far off the correct phase values. For example, the reflections #15 and #38 had errors of 27° and 60°, respectively. These deviations can be explained by Cochran's work.[32] According to his derivation, when the number of terms in the summation is large

$$\sum_{1}^{m} E_{\vec{k}} E_{\vec{h}-\vec{k}} \xrightarrow{m \text{ large}} V_{\vec{h}}.$$

In our case the number of s2rs included in the summation was indeed large and it was expected that the phases calculated from the E-E relation should be closer to the values of β than of α. Thus it can be seen that the phase-angle errors which were 27° and 60° when compared with α, were only 2° and 3° when compared with β.

This phenomenon was also seen in the values of α'. For example, reflections such as #6,12,16,18, and 38 had large values of $(\alpha' - \alpha)$, but their $(\alpha' - \beta)$ values were relatively small. These smaller values of $(\alpha' - \beta)$ can be considered as strong supporting evidence for the basic assumption, $\rho^2 \sim M_{ps} \cdot \rho$, which was used in deriving our Σ_2-like relation.

The variation of the phase angle obtained as a function of the number of s2rs in the E-G relation gives additional

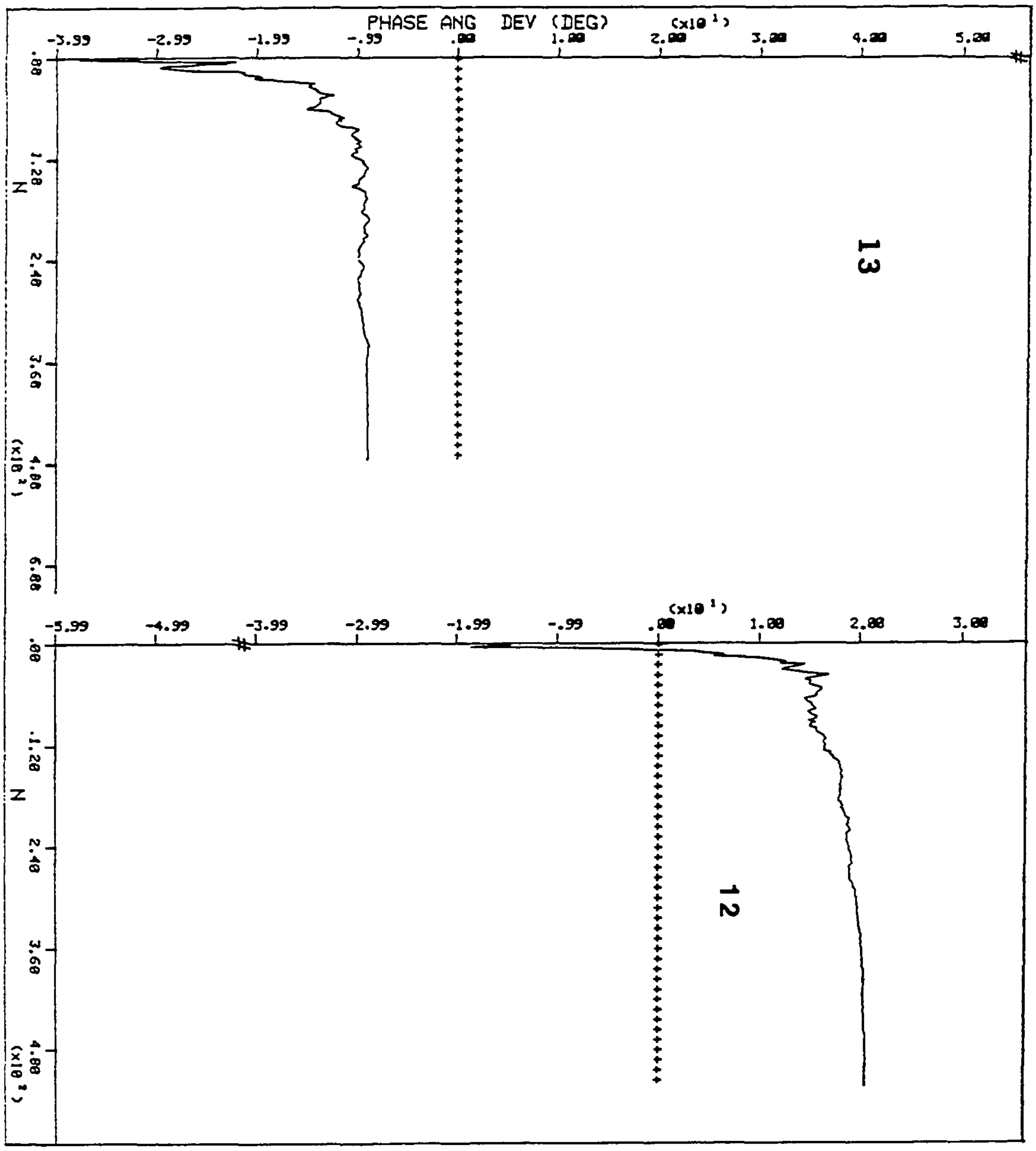
PHASE ANG DEV (DEG)
(x10¹)
-3.99
-2.99
-1.99
-.99
.00
1.00
2.00
3.00
4.00
5.00
N
.00
1.20
2.40
3.60
4.80
6.00
(x10²)
13
(x10¹)
-5.99
-4.99
-3.99
-2.99
-1.99
-.99
.00
1.00
2.00
3.00
N
.00
1.20
2.40
3.60
4.80
(x10²)
12

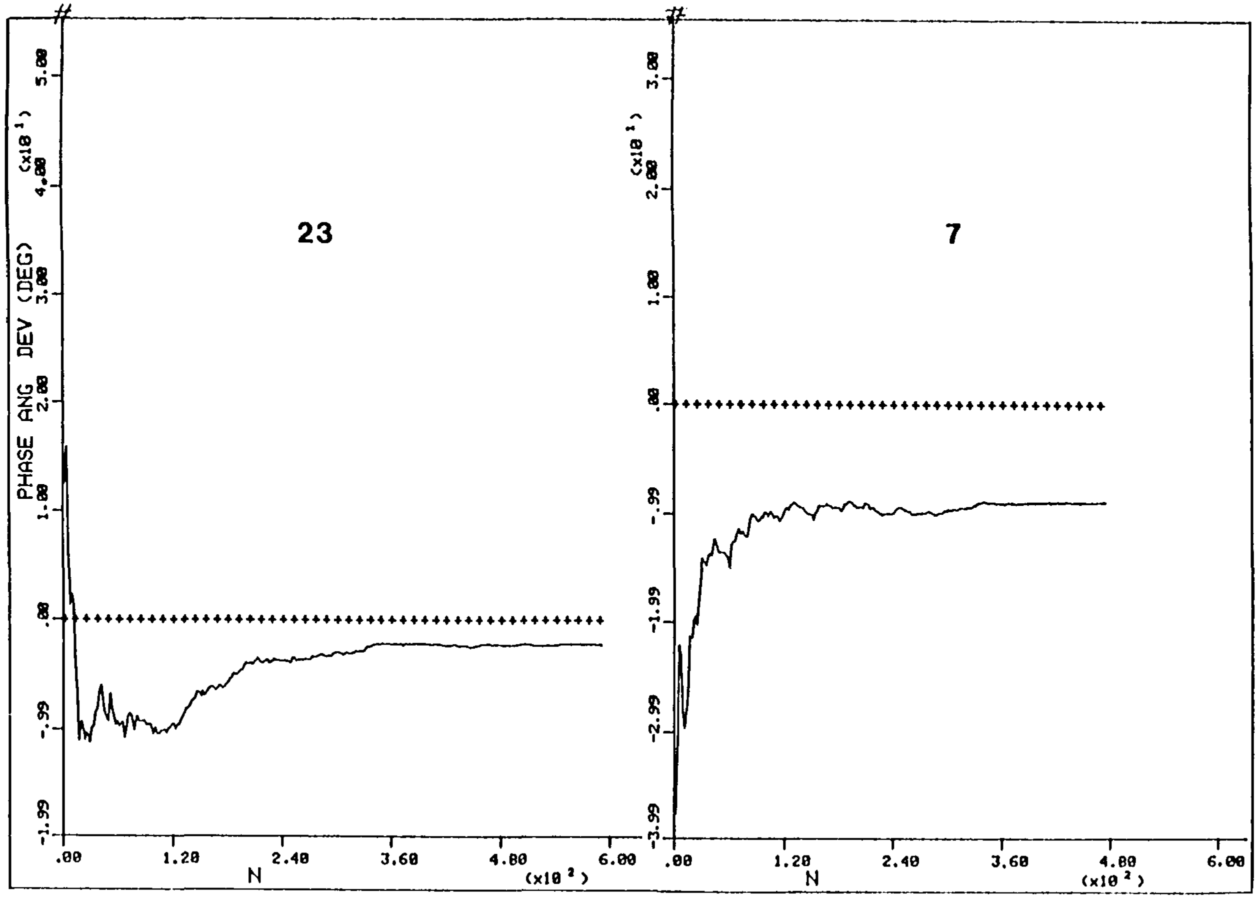

Fig. A-4 Phase-angle errors as a function of number of s2rs. See text for detail.

insight. The phase-angle errors of reflections #7,#12,#13 and #23, as a function of the number of s2rs are plotted in Fig. A-4. The symbol "#" on each plot denotes the quantity $(\alpha-\gamma)$, the original phase angle error in the G's. The summation was taken from the strongest sigma two relationships, in our case the largest value of the product of $|E_{\vec{k}}|$ and $|G_{\vec{h}-\vec{k}}|$ instead of $|E_{\vec{k}}|$ and $|E_{\vec{h}-\vec{k}}|$, to the weakest one. In these four plots, it is clearly seen that the phase-angle errors converge very fast within just the first several strongest s2rs. This may implies a positive answer to question (3).

To use only a subset of reflections in the E-G relation, the same procedure used above was repeated except that: (A) only one tenth of s2rs were summed, and (B) only those s2rs in which the value of $|E_{\vec{k}}|\geq 1.5$ were used. (A) was done by dividing the total number of s2rs into groups such that each group contains 10 s2rs. Only the first one in each group was selected and used in the calculation of α'. (B) was done by neglecting those s2rs in which the value of $|E_{\vec{k}}|<1.5$ in the summation. In both cases, the weight of $|E_{\vec{k}}G_{\vec{h}-\vec{k}}|$ was applied. The phase angle for each reflection was also calculated via Sayre's E-E relation. All of the results are shown in Table A-12.

In (A), the mean phase-angle errors were 10° and 12° by the E-G relation and Sayre's E-E relation, respectively. In (B), a different reflection set was used and the mean phase-angle errors were also small. The individual phase-angle

Table A-12. The results of the E-G relation for the structure FSA structure when only a subset of reflections included in the summation

			(A)[a]				(B)[a]		
#	|E|(|G|)	α[b]−γ	#s2rs	α′−α	α′−β	Δ[c]	#s2rs	α′−α	α′−β
1	2.39(0.30)	87	50	12	0	17	78	9	-4
2	2.27(3.11)	47	34	-24	-21	-2	53	-9	-6
3	2.21(1.32)	-73	79	4	9	-2	130	1	6
4	2.17(4.25)	11	54	1	1	-7	86	-4	-4
5	2.07(4.07)	-11	101	0	1	-3	147	0	0
6	1.99(0.96)	-76	54	11	2	10	86	17	8
7	1.98(2.26)	55	48	-22	-30	15	74	-14	-21
8	1.97(3.54)	-26	42	-1	1	-7	71	14	16
9	1.96(3.38)	30	64	-3	-10	0	101	-3	-9
10	1.95(3.90)	-2	45	-6	-12	7	79	7	0
11	1.95(0.89)	-77	84	-8	-7	1	128	-1	1
12	1.94(2.91)	-41	53	13	4	18	78	21	12
13	1.92(3.65)	18	46	-12	-14	2	80	-5	-7
14	1.89(3.57)	-19	50	10	6	5	77	13	9
15	1.84(3.10)	33	49	11	-14	23	72	-1	-25
16	1.79(1.50)	65	78	-29	-10	-25	114	-31	-14
17	1.77(1.88)	58	78	-3	3	0	105	5	12
18	1.73(0.82)	76	69	-32	-12	-25	99	-36	-16
19	1.72(0.50)	-82	66	6	3	0	89	1	-2
20	1.70(2.85)	33	56	-16	-10	-13	80	-14	-7
21	1.63(3.26)	2	52	5	-6	4	82	5	-6
22	1.61(0.23)	-86	56	-3	-13	14	74	7	-3
23	1.59(0.88)	74	60	14	9	15	80	-8	-14
24	1.56(2.82)	25	46	5	-10	7	70	-6	-21
25	1.54(2.87)	21	47	0	5	-6	74	-7	-2

26	1.50(1.01)	-70	78	7	12	3	101	-6	0
27	1.47(2.90)	-9	76	-1	10	-7	109	3	14
28	1.42(2.83)	-5	52	16	3	23	74	16	3
29	1.36(2.71)	-1	36	-3	-2	-8	57	4	5
30	1.31(2.48)	19	57	1	0	8	92	3	1
31	1.23(2.45)	-4	37	-4	3	-5	58	11	17
32	1.17(2.33)	-4	45	1	20	-26	72	-5	14
33	1.11(2.16)	13	65	-3	23	-25	86	-10	15
34	1.04(2.07)	1	42	13	7	16	66	2	-4
35	1.00(2.00)	4	75	-8	16	-21	117	-7	18
36	0.93(1.87)	-2	57	-4	-2	0	82	5	6
37	0.90(1.71)	-18	66	16	20	10	82	3	7
38	0.79(1.56)	-9	59	50	-8	46	65	43	-14
39	0.71(1.37)	-14	48	-3	-13	18	69	4	-6
40	0.66(1.28)	15	74	18	1	26	96	2	-15
41	0.59(1.15)	12	63	5	0	6	80	-3	-8
mean error:		32		10	9	12		9	9

[a] See text for detail.

[b] α is the phase angle of E, γ is the phase angle of G, β is the phase angle of V (the squared structure factor, see p.10), and α' is the new phase angle of E calculated from the E-G relation, (2.18).

[c] $\Delta = \langle\alpha\rangle - \alpha$, where $\langle\alpha\rangle$ is the new phase angle of E estimated from Sayre's E-E relation.

deviation for each reflection obtained from the E-G relation was also consistent with that obtained from the E-E relation. Those with larger values of $(\alpha'-\alpha)$, for instance, reflections #7,16,18,28, and 38, also had larger values of Δ. All these results indicate that the E-G relation is almost as good as Sayre's Σ_2 relation even if only a subset of reflections is used.

Another fifty reflections which satisfied the condition that the values of both $|E|$ and the corresponding $|G|$ were large were selected to test if the E-G relation would hold for a small set of reflections. Only those s2rs in which $|E_{\vec{k}}|\geq 1.5$ and $|G_{\vec{h}-\vec{k}}|\geq 2.75$ were included in the calculation of the new phases for the reflection $\vec{h}$.

Four different sizes of $\vec{k}$ set were tried. In Table A-13 from columns (A) to (D) the number of s2rs included in the calculation of the values of α' are gradually decreased to less than 5 for each reflection. In average, there were 18.8, 6.6, 4.2 and 2.8 sigma-two relationships per reflection (s2rspr) for (A), (B), (C) and (D), respectively. The mean phase-angle error was very small (5.6°) in (A) and slightly increased to 8.8° in (C) as s2rspr decreased to 4.2. Fig. A-5 shows the phase angle error as a function of s2rs for reflections #4,#16 and #25 respectively. Again the summation was done from the strongest s2rs to the weakest. All these data suggest a very positive answer to question (3).

Although a further decrease in s2rspr, such as 2.8 in

Table A-13. The results of the E-G relation for the structure FSA when only a few strong sigma-two relationships are used in the summation

			(A)		(B)		(C)		(D)		(E)	
#	|E|(|G|)	$\alpha^a-\gamma$	#s2rs	$\alpha'-\alpha$	#s2rs	$\alpha'-\alpha$	#s2rs	$\alpha'-\alpha$	#s2rs	$\alpha'-\alpha$	#s2r	$\alpha'-\alpha$
1	2.30(4.38)	18	(29)	-3	(10)	-3	(6)	-3	(4)	1	(14)	-2
2	2.27(3.11)	47	(16)	-8	(6)	-13	(4)	-11	(2)	-6	(3)	-31
3	2.23(4.38)	10	(26)	-3	(9)	-4	(6)	-6	(4)	6	(19)	4
4	2.20(3.09)	-45	(18)	4	(6)	14	(4)	1	(3)	27	(3)	61
5	2.17(4.25)	11	(22)	-2	(8)	16	(5)	1	(3)	7	(13)	3
6	2.14(3.73	29	(18)	-2	(6)	-6	(4)	-2	(3)	1	(7)	15
7	2.07(4.07)	11	(43)	3	(15)	3	(9)	-2	(6)	9	(20)	4
8	2.05(3.59)	29	(23)	-9	(8)	-11	(5)	-13	(3)	-7	(14)	-14
9	1.98(3.22)	26	(18)	-4	(6)	1	(4)	15	(3)	-1	(7)	-20
10	1.97(3.54)	16	(14)	4	(5)	-14	(3)	-14	(2)	0	(7)	40
11	1.96(3.38)	30	(19)	-4	(7)	-7	(4)	-2	(3)	6	(10)	-15
12	1.95(3.90)	-2	(23)	-1	(8)	-13	(5)	8	(3)	1	(7)	18
13	1.95(3.88)	-5	(23)	2	(8)	-1	(5)	-8	(3)	22	(12)	19
14	1.94(3.80)	12	(28)	2	(10)	11	(6)	11	(4)	16	(15)	3
15	1.93(3.86)	0	(15)	8	(5)	14	(3)	11	(2)	-14	(6)	14
16	1.93(3.65)	18	(25)	0	(9)	-5	(5)	-1	(4)	9	(14)	-3
17	1.93(3.85)	-3	(21)	10	(7)	7	(5)	3	(3)	24	(12)	18
18	1.92(3.52)	23	(23)	-11	(8)	-11	(5)	-5	(3)	-17	(9)	-9
19	1.91(3.53)	-22	(16)	-7	(6)	-18	(4)	-7	(2)	-8	(5)	39
20	1.89(3.57)	-19	(14)	10	(5)	8	(3)	-3	(2)	-9	(7)	35
21	1.87(3.43)	-23	(14)	-5	(5)	-13	(3)	2	(2)	-33	(5)	39
22	1.86(3.28)	28	(12)	-10	(4)	-10	(3)	-15	(2)	-10	(6)	-14
23	1.86(3.16)	-32	(12)	-2	(4)	-20	(3)	-5	(2)	-28	(4)	46
24	1.86(3.45)	-22	(16)	0	(6)	9	(4)	-3	(2)	-24	(5)	37
25	1.85(3.10)	33	(14)	-3	(5)	-2	(3)	6	(2)	2	(5)	-18

26	1.84(3.63)	8	(26)	10	(9)	-2	(6)	2	(4)	19	(11)	7
27	1.84(3.10)	33	(10)	-7	(4)	2	(2)	-7	(2)	17	(4)	-17
28	1.79(3.28)	24	(12)	8	(4)	6	(3)	29	(2)	2	(3)	-5
29	1.78(3.34)	20	(19)	0	(7)	-4	(4)	-10	(3)	23	(9)	-5
30	1.78(3.31)	21	(26)	-3	(9)	-1	(6)	-1	(4)	5	(15)	-6
31	1.77(3.44)	-13	(11)	5	(4)	-2	(3)	7	(2)	-9	(4)	29
32	1.76(3.52)	3	(24)	7	(8)	11	(5)	6	(3)	10	(11)	11
33	1.76(3.27)	-22	(18)	0	(6)	-1	(4)	20	(3)	28	(8)	37
34	1.76(3.50)	-6	(11)	13	(4)	20	(3)	12	(2)	14	(6)	20
35	1.76(3.50)	-5	(19)	5	(7)	15	(4)	25	(3)	13	(10)	19
36	1.75(3.46)	-9	(17)	11	(6)	-1	(4)	14	(3)	11	(9)	25
37	1.74(3.43)	9	(19)	12	(7)	11	(4)	13	(3)	14	(8)	6
38	1.73(3.11)	-26	(18)	-3	(6)	-3	(4)	-3	(3)	-24	(6)	42
39	1.71(3.21)	21	(22)	-2	(8)	12	(5)	9	(3)	-12	(9)	-4
40	1.71(3.34)	-12	(16)	3	(6)	2	(4)	8	(2)	3	(8)	25
41	1.70(3.00)	28	(25)	-3	(9)	4	(5)	-7	(4)	-7	(10)	-14
42	1.70(3.39)	-4	(17)	-2	(6)	-7	(4)	-3	(3)	-7	(8)	20
43	1.68(3.31)	9	(13)	5	(5)	9	(3)	-4	(2)	5	(6)	5
44	1.67(3.05)	-24	(16)	11	(6)	14	(4)	36	(2)	39	(7)	39
45	1.67(3.25)	-13	(23)	11	(8)	11	(5)	18	(3)	16	(9)	28
46	1.66(3.31)	2	(23)	7	(8)	11	(5)	11	(3)	-16	(10)	11
47	1.66(3.16)	18	(11)	9	(4)	12	(3)	18	(2)	2	(6)	-2
48	1.66(3.15)	-18	(7)	-21	(3)	-23	(2)	-18	(1)	-28	(1)	32
49	1.66(3.15)	18	(17)	5	(6)	5	(4)	-2	(3)	0	(6)	-2
50	1.66(3.25)	11	(17)	1	(6)	1	(4)	-2	(3)	18	(11)	3
mean error:		17.8		5.6		8.5		8.8		12.6		18.7

$^a\alpha$ is the phase angle of E, γ is the phase angle of G (see p.10), and α' is the new phase angle of E calculated from the E-G relation, (2.18).

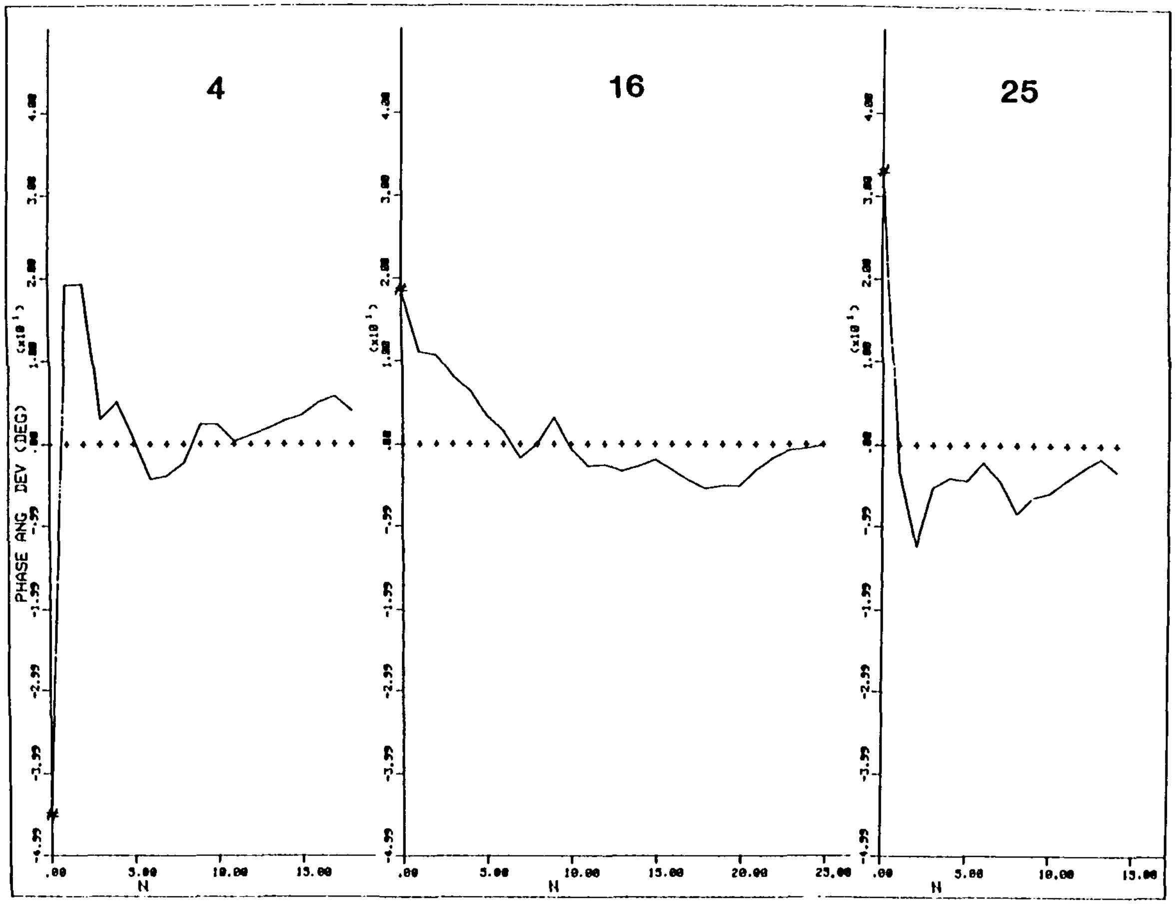

Fig. A-5 Phase-angle error as a function of s2rs. See text for detail.

(D), caused the phase error to jump to 12.6°, this value was still much better than that of $(\alpha-\gamma)$. Direct phase transfer from the G's to the corresponding E would result in a mean error of 17.8° for those 50 reflections.

From the above results, it is clearly seen that the phases as well as the magnitudes of the G's could be effectively utilized in the triple phase relationship in an acentric structure like FSA. In the centric case, signs of some reflections with the large |G|'s can be directly transferred to the phases of corresponding the E's (for example, in the structure CA, sign transferability was ~95% for reflections whose $|E|\geq 1.5$ and $|G|\geq 1.5$). However, phase transfer was not adequate in the FSA structure. In Table A-13 one can see that in this particular case, even though both |E| and |G| were very large for a reflection (e.g., #2, #3, etc.), the value of $(\alpha-\gamma)$ could be very large, too. These large phase errors may not form an accurate enough starting phase set from which a good phase set could be obtained via our modified tangent formula phase refinement procedure. How can one find a reliable phase set with which to start?

The usual way to tackle this problem is to start with the phases of the G's and use these for both $E_{\vec{k}}$ and $G_{\vec{h}-\vec{k}}$ and calculate better phases via the E-G or the E-E relation for some reflections with large |E|'s. Unfortunately, this method did not work for the FSA structure. Here the structure factors G are centrosymmetric and the values of the phase angle γ were either 0 or π. Even using equations (2.18) or (2.3), the new phases obtained would always be 0 or π. The result were exactly the same as that obtained by applying the direct phase transfer from G to $|E|$.

To solve this problem, a new scheme was tested. In this scheme, a constant δ was first added to the phases of some reflections with large G values to shift them away from 0 or π, and then transferred to be used as the phases of the corresponding E's. In this way, the initial phase values were not zero or π for the k→ set, $(E_{\vec{k}})$, though they were still 0 or π for the $(\vec{h}-\vec{k})$ set, $(G_{\vec{h}-\vec{k}})$. After phase averaging took place among all of the s2rs from this limited $\vec{k}$ and $(\vec{h}-\vec{k})$ reflection sets, better phases could be obtained for those reflections with large $|E|$ values. The values of δ were fixed in a range from 10° to 16°. This range was chosen as it was not only large enough to make a contribution to the imaginary part of the structure factor but also small enough to avoid introducing significant amount of errors in the phases. The new scheme was applied to the 50 sample reflections in Table A-13 and the differences between the phases obtained from such, α', and the true phase angles as well as the number of s2rs involved are listed the column (E) in Table A-13.

The mean phase error obtained by this new scheme for the 50 sample reflections were about the same as that from a direct phase transfer. However, the advantage of this new scheme over the direct phase transfer method was in that we could now recognize some reflections which had more reliable phases than others just by setting up a criterion involving the the number of s2rs used in the derivation of the new phases or by using the probabilities which were mentioned on page 49.

Test results for structure CR The structure CR (see Table A-7 for detail) crystallized in space group $P2_1$. Two real Patterson superposition maps of this structure were generated using two different displacement vectors. The first superposition map, SUPR1, was obtained via a displacement vector which corresponded to a double CR-O vector peak. This would theoretically result in four images, i.e., two pairs of inversely related structural images. After a symmetry analysis, which was mentioned in Chapter 6, the first 143 peaks (two times more than the number of real atoms, 54) were used to obtained the structure factors G by using equation (7.1). The second superposition map, SUPR2, was obtained by using a single CR-CR vector, corresponding to a twofold screw symmetry-related Harker vector. This map was also treated by the symmetry analysis and the pseudo-normalized structure factors G were then computed from the first 189 peaks (3.5 times the number of real atoms) according to (7.1). The phase differences between the G's and E's are listed in Table A-14. They are also plotted as a function of |E| and |G| separately

Table A-14. Mean phase-angle error (based on 1523 reflections) as functions of |G| and |E| for the structure CR

(a) G were calculated from 143 vector peaks on SUPR1

E\G	2.50	2.25	2.00	1.75	1.50	1.00	0.50	0.00
2.25	13.7	13.8	17.1	17.5	17.5	15.9	16.7	16.3
2.00	13.5	14.1	15.7	15.7	15.8	14.9	18.7	18.5
1.75	14.7	15.1	16.0	17.0	16.8	17.6	25.7	25.8
1.50	15.8	16.8	18.1	18.6	18.6	20.0	27.7	30.7
1.00	16.1	17.5	18.2	19.5	20.5	26.1	35.6	43.0
0.50	16.1	19.3	19.2	21.4	22.3	31.1	48.5	57.4
0.00	17.9	20.5	20.4	22.2	25.6	36.8	55.5	65.2

(b) G were calculated from 189 vector peaks on SUPR2

E\G	2.50	2.25	2.00	1.75	1.50	1.00	0.50	0.00
2.25	9.7	9.7	9.7	9.4	9.4	9.9	9.9	15.8
2.00	10.1	10.0	9.5	10.1	10.5	11.4	11.4	14.2
1.75	10.5	10.0	10.7	11.6	12.9	14.9	15.2	20.6
1.50	11.8	11.2	12.4	13.4	14.5	16.3	18.9	26.2
1.00	11.8	11.1	12.4	13.8	15.6	19.0	23.7	37.8
0.50	11.8	11.1	14.4	15.4	17.2	25.2	37.9	55.1
0.00	15.5	14.2	16.6	20.1	22.0	32.9	46.2	61.6

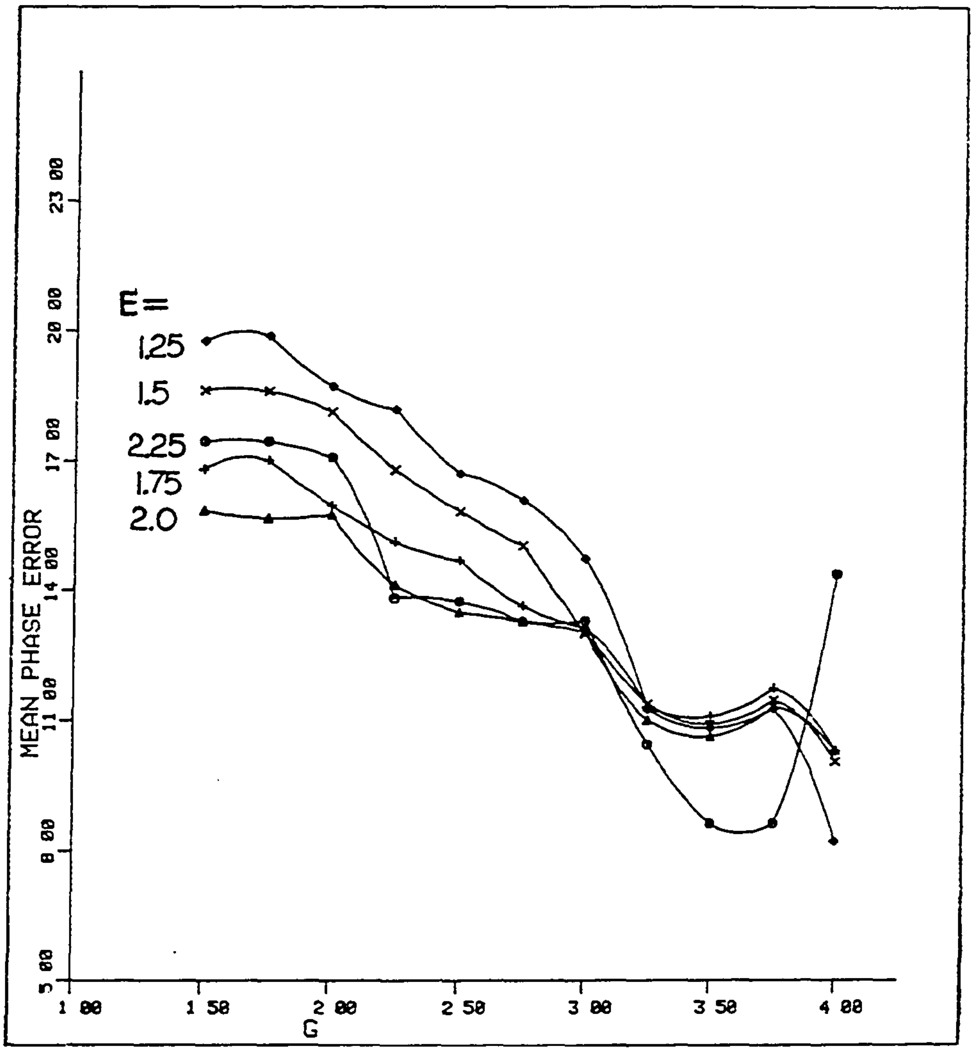

Fig. A-6 Mean phase-angle error as functions of |G| and |E| for SUPR1.

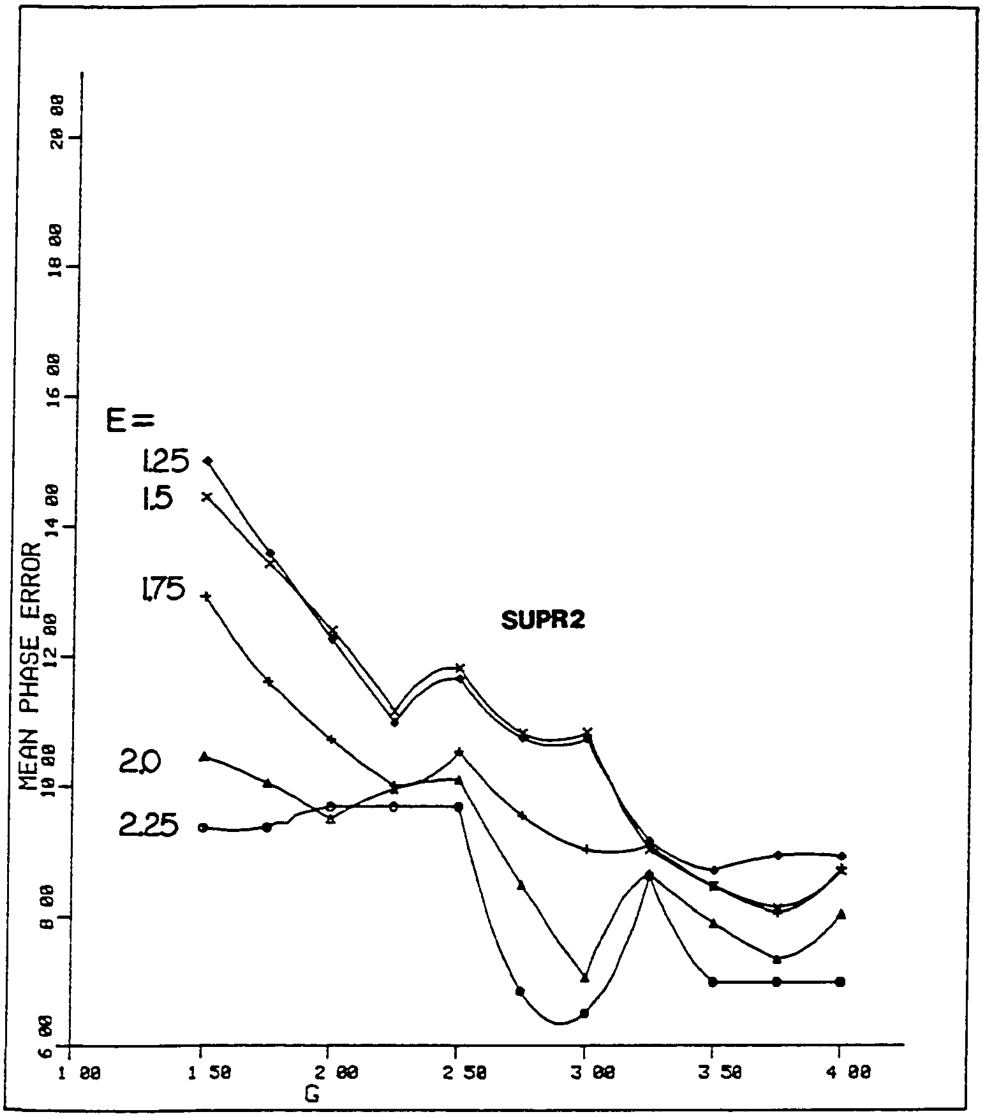

Fig. A-7 Mean phase-anlge error as functions of |G| and |E| for SUPR2.

in Fig. A-6 and Fig. A-7.

From these two figures, it can be noticed that the phases of the G's of SUPR2 were better than those of SUPR1. Two explanations may be advanced. First, the real-atom ratio on the two maps were 21:26 (27 independent atoms per asymmetric cell in the structure). Second, the false atoms in SUPR2 were more randomly distributed than those in SUPR1 so that phase errors were cancelled out among one another to a larger extent than in SUPR1.

Before applying the E-G relation to the phases of the G's, an unweighted γ'-synthesis was performed to examine the nature of this Fourier synthesis. The 300 reflections with $|E| \geq 1.33$ (with their average phase-angle errors in G of 36.9° for SUPR1 and 28.5° for SUPR2) were used to calculate the E maps. The results are shown in Tables A-15 and A-16, respectively (only the first 50 or so of the highest electron density peaks are listed in these tables).

Note that only 21 real atoms appeared on the SUPR1 but the γ'-synthesis resulted in two more atoms, namely C2 and N7, to give a total of 23 real atoms. This gain in real atoms was carefully checked to see if they were among the original 143 atom peaks on SUPR1 map and they were not. For SUPR2, although among the top 53 peaks, there were the same number, 25, of real atoms found in the γ'-synthesis, the ninth peak (C12) was not one of the 189 peaks in SUPR2 at all. Therefore, this atom was also gained from the Fourier

Table A-15. Comparisons of identified atoms obtained from different phase sets for the structure CR

pk no.	SUPR1	|E|exp(iγ)	E-G	E-E
identified atoms	21	23	26	27
1	Cr	Cr	Cr	Cr
2	N4	N4	O1	O1
3	O1	O1	N4	N4
4	O3	C12	N1	N1
5	*(O3')[a]	*(O3')	C11	C11
6	*(C12')	N1	O3	O3
7	C12	*(N1')	O2	O2
8	N1	C11	O6	C2
9	*(N1')	*	N3	O6
10	C6	O4	C2	O5
11	N2	O5	O4	N3
12	O4	O3	C12	N5
13	*	*(O2')	N5	N7
14	*	*(C8')	N2	O4
15	O5	*(N7')	O5	C6
16	*(N6')	C8	N6	N2
17	N6	*(N3')	C6	N6
18	*	O2	N7	O7
19	*	*(N2')	C5	C12
20	*(C8')	N2	C1	C5
21	C8	N3	O7	C1
22	O7	N6	*(C11')	*
23	*(O7')	C1	C8	C8
24	*	C6	*	*(C11')
25	*(N3')	*(O7')	*(O3')	C10

26	N3	N5	*(C8′)	*
27	*	*	*(N1′)	*
28	O2	O6	*	*(O3′)
29	*(O2′)	O7	C7	C4
30	*	*(N5′)	*	C7
31	*(C11′)	*	*	*
32	C11	*	C4	C9
33	*(C4′)	*	*	*
34	C4	C2	C10	*(N1′)
35	*	N7	*	*
36	*	*	*	*
37	*	C5	*	*
38	*	*	*	*
39	*	C4	*	*
40	*	*	*	*
41	C1	*	*	*
42	*(C1′)	*	*	*
43	*	*(C2′)	C9	*
44	*	*	*	*
45	*(N5′)	*	*	C3
46	N5	*	*	
47	*(C5′)	*	*	
48	C5	*	*	
49	*	*(C4′)	*	
50	O6	*	*	

[a] The *′s represent extraneous atoms; atom symbols with primes in parentheses belonged to an image enantiomorphic to the correct one.

Table A-16. Comparisons of identified atoms obtained from different phase sets for the structure CR

pk no.	SUPR1	$\lvert E\rvert \exp(i\gamma)$	E-G	E-E
identified atoms	25	25	27	27
1	Cr	Cr	Cr	Cr
2	O1	O1	O1	O1
3	N4	O4	N4	N4
4	O4	*(O3')	C11	N1
5	O3	*	N1	C11
6	*(O3')[a]	O3	O3	O3
7	N2	*(N1')	C2	O2
8	N1	N1	O2	C2
9	*(N1')	C12	O4	O6
10	*	N2	O6	N7
11	*(O2')	C11	N3	O4
12	O2	N4	N6	O5
13	*(C6')	*(N3')	N2	N5
14	C6	*(C11')	N5	N3
15	*(N3')	C6	N7	N6
16	N3	O5	O5	N2
17	*(C2')	*(C2')	C5	O7
18	C2	*(C8')	C6	C6
19	*(N7')	C8	C12	C5
20	N7	N3	*	C12
21	*(C5')	C2	C8	*
22	C5	N6	O7	C1
23	*(N6')	*(C1')	C1	C8
24	N6	*(N6')	*	C10
25	*(C4')	O2	*	*
26	C4	C10	*	*
27	*(C11')	*(N5')	C10	*

28	C11	C1	*(C8′)	C4
29	C7	*(N7′)	C7	C7
30	*(C7′)	*(O6′)	*(N1′)	*
31	C8	N7	C4	*
32	*(C8′)	O6	*	C9
33	O5	*	*	*
34	*(C1′)	*(O2′)	*	*
35	C1	*(O7′)	*	*
36	*	N5	*	*
37	*	*(C10′)	*	*
38	*	O7	C9	*
39	C9	C5	*	*
40	*(C9′)	*(C5′)	*	*
41	*(C10′)	*	*	*
42	C10	C4	*	*
43	*(N5′)	*	*	*
44	N5	*(C4′)	*	C3
45	O7	C7	*	
46	*(O7′)	*	*	
47	C3	*	*	
48	*(C3′)	*	*	
49	*	*(C7′)	*	
50	*	*	*	
51	*	*	*	
52	*	*	*	
53	*	*	C3	

---

[a] The *′s represent extraneous atoms; atom symbols with primes in parentheses belonged to an image enantiomorphic to the correct one.

synthesis using the quantities $|E_{obs}|\exp(i\gamma)$ as the Fourier coefficients. These results indicate that the γ'-synthesis is useful in improving the Patterson superposition function.

The new phase angles obtained by using the E-G relation, (2.18), and the E-E relation, (2.3), for those 300 reflections mentioned above were separately combined with $|E_{obs}|$ to compute E maps. Atoms thus found are also listed in Tables A-15 and A-16. The results obtained from the E-G relation were very close to those obtained from the E-E relation for both SUPR1 and SUPR2. Once again, one is convinced that the substitution of the G's for the E's in the sigma two relation is valid.

Mean phase-angle errors for both SUPR1 and SUPR2 obtained from different methods are summarized in Table A-17. Again, α denotes the true phase angle, γ is the phase angle of the structure factor G', and β is the phase angle of the squared structure factor V. The phase angles obtained from the E-G relation and the E-E relation are denoted by α' and α'', respectively. In the case of SUPR1, before the phases were recalculated by the E-G relation, the mean phase-angle errors with respect to α were 36.9° and 0° for the structure factors G and E. After the phases were refined via equation (2.18) and (2.3) separately, the errors, 17.6° and 13.7°, became very close to each other. The phase-angle errors with respect to β became 10.2° and 6.8° after refinement. All these data indicate that good structural solutions could be obtained by

Table A-17. Six different mean phase-angle errors calculated from 300 reflection with $|E| \geq 1.33$ for the structure CR

Designation	Type[a]	SUPR1	SUPR2
1	$\alpha - \gamma$	36.9	28.5
2	$\alpha - \alpha'$	17.6	17.0
3	$\alpha - \alpha''$	13.7	13.5
4	$\beta - \alpha'$	10.2	7.5
5	$\beta - \alpha''$	6.8	5.9
6	$\beta - \alpha$	12.1	12.1

[a] α is the phase angle of the E's. γ is the phase of the G's. α' is the phase angle obtained by using the E-G relation and α'' is the phase angle obtained by using the E-E relation. β is the phase angle of the squared structure factor V.

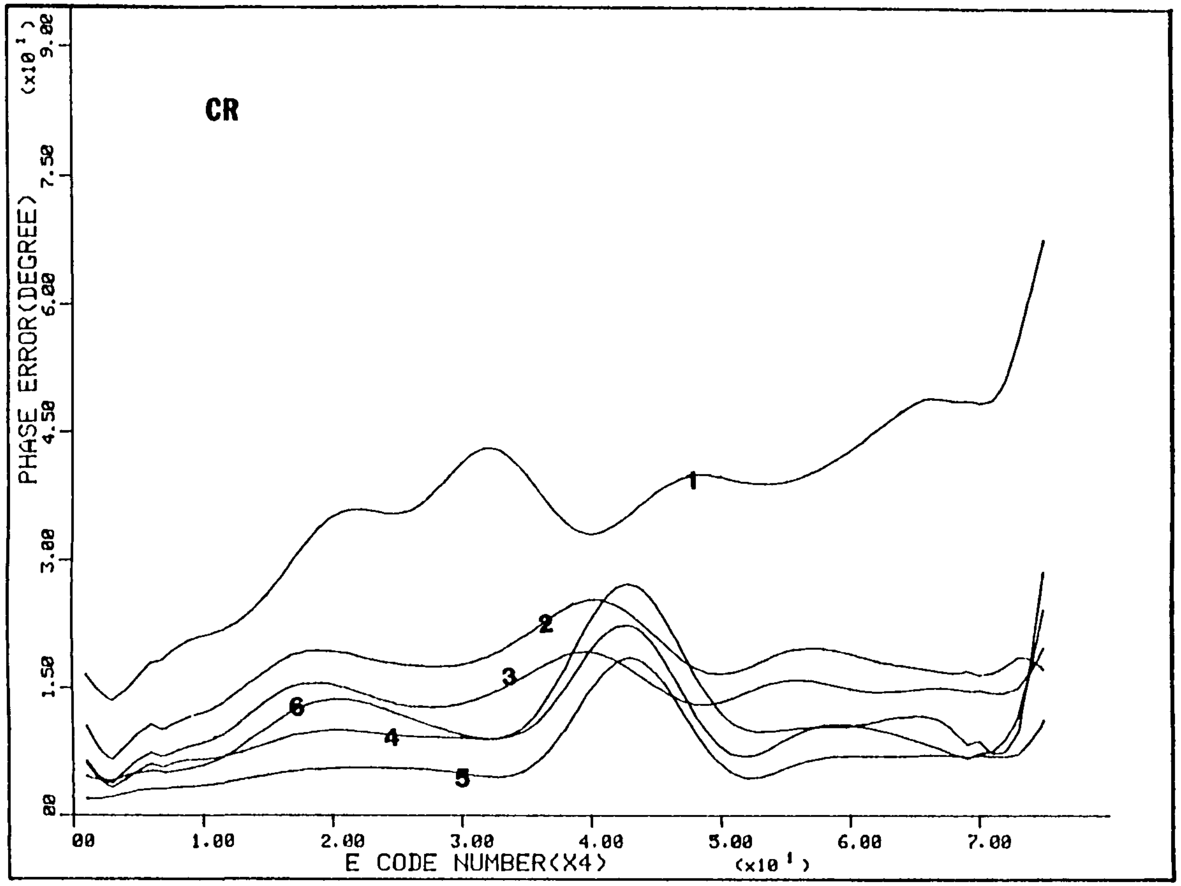

Fig. A-8 Phase-angle error as a function of |E| for SUPR1. See text for detail.

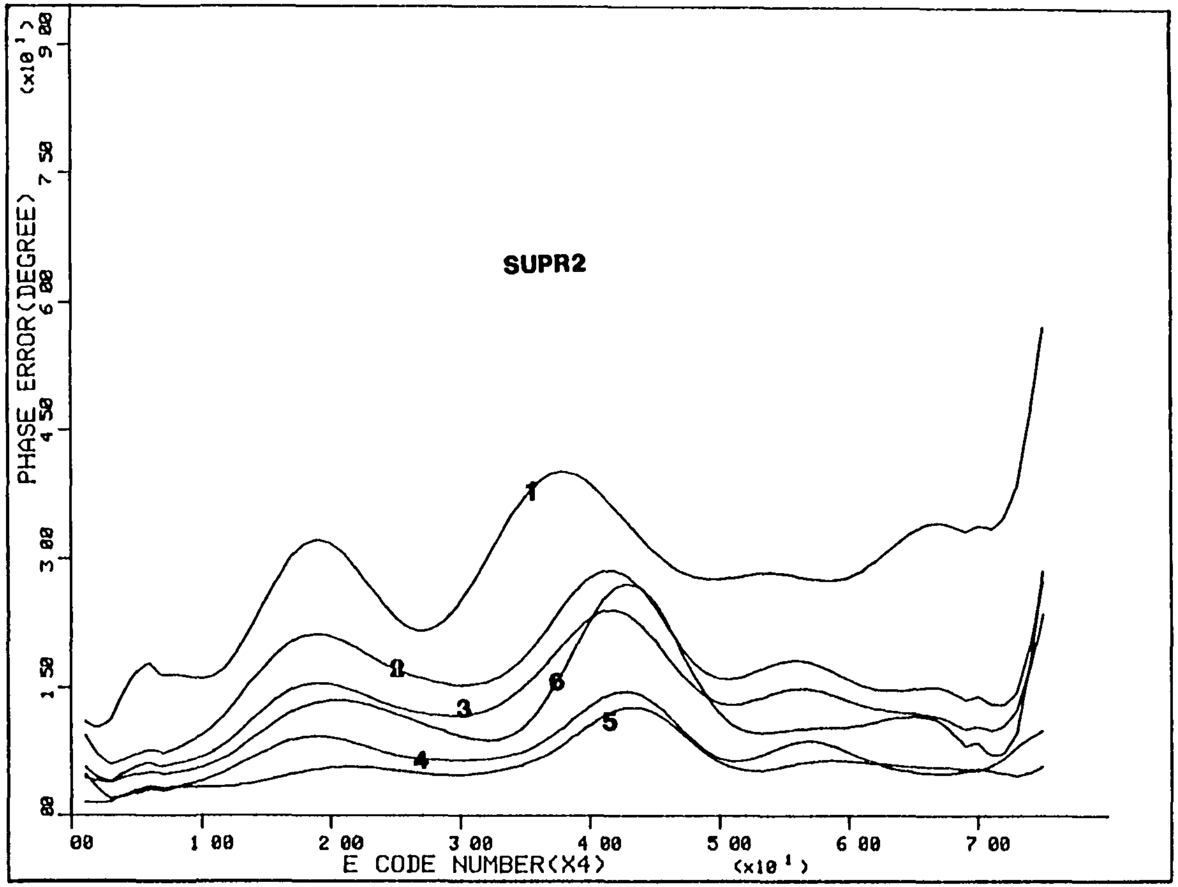

Fig. A-9 Phase-angle error as a function of |E| for SUPR2. See text for detail.

using the E-G relation.

The phase-angle errors as a function of the magnitude of |E| (the smaller the code number for a reflection, the larger the magnitude of E) for the 300 reflections are plotted in Fig. A-8 and Fig. A-9. It can be seen that curves 2 & 3, and 4 & 5 are very close to each other, and variations in phase angles within each pair is also consistent.

The Statistical Tests

All of the probabilistic properties which are associated with the Fourier coefficients of Patterson superposition functions have been derived using the same principle as that for the "heavy-atom" case which was mentioned on page 21. Now we need to prove that the properties so obtained are correct. This can be done by comparing experimental data with those predicted by equation (3.5) or (3.15). Two tests were performed. The first one was conducted on a centrosymmetric structure, EC, and the second one was conducted on a noncentrosymmetric structure, CR.

The first test structure EC was a hypothetical equal-atom case version of the structure of FeS_3OC_8 (see Table A-7) with $P\bar{1}$ space group symmetry. 23% to 400% extra electron density was added into this structure to generate twelve different sets of atom coordinates to represent 12 different Patterson superposition maps. Since all of the atoms were regarded as point atoms, the factor r (which was defined in Table A-2) in each map was then treated as a constant. The pseudo-normalized structure factors G were calculated from each of the 12 superposition maps using equation (2.11). Their signs were subsequently compared with the true signs. The values of r, which in a sense correspond to the square root of the ratio of the total scattering power to that contributed from the atoms at wrong position, the percentage of correct signs and other related information are listed in Table A-18. The fraction of the number of the structure factors E which have the same signs as those of G is also plotted in Fig. A-10 as a function of r for each of the twelve superposition maps. In this figure, the solid curve represents the predicted values of N_f. The circles are the experimental data at different r. It is clearly seen that they are in satisfactory agreement with the theoretical values.

The second test structure was the noncentrosymmetric structure CR (see Table A-7) with $P2_1$ space group symmetry. "Extraneous" atoms ranging in number from 26% to 400% with their coordinates randomly selected from the Patterson map of the CR structure were separately added to the real atom coordinates to generate twelve different hypothetical Patterson superposition functions. In this non-centrosymmetric structure, however, the reflections in the h00, 00l lines and h0l zone were centrosymmetric. Equation (3.5) was expected to give a good estimate of the fraction of

Table A-18. The test of the fraction of the structure factors determined in sign by G for the structure EC

set no.	# atoms (M/2)	r	%extra atoms	%correct atoms	%correct phase	N_f
1	16	2.309	23.1	81.3	86.7	86.87
2	18	1.897	38.5	72.2	84.2	84.26
3	20	1.690	53.8	65.0	82.4	82.69
4	23	1.517	76.9	56.5	80.9	81.13
5	26	1.414	100.0	50.0	77.9	77.83
6	30	1.328	130.8	43.3	75.3	75.39
7	35	1.261	169.2	37.1	72.6	71.74
8	39	1.225	200.0	33.3	71.7	71.56
9	46	1.180	253.8	28.3	71.1	71.04
10	52	1.154	300.0	25.0	68.0	68.09
11	58	1.135	346.1	22.4	65.9	66.00
12	65	1.118	400.0	20.0	64.6	64.22

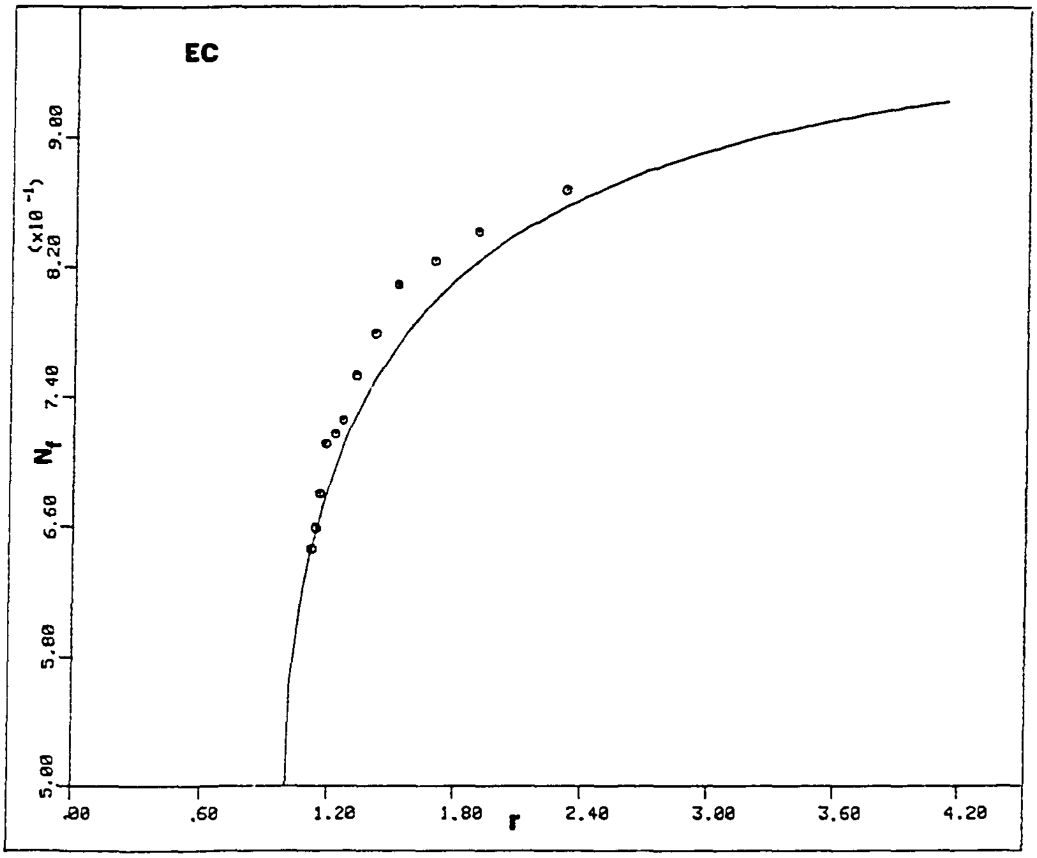

Fig. A-10 The observed (circles) and theoretical (smoothed curve) values of N_f as a function of r for the structure EC.

the structure factors E whose signs were the same as those of the corresponding G's. The values of r and percentage of correct signs for these reflections along with other related information are listed in Table A-19. The values of r and fraction of correct signs for the total 223 centrosymmetric reflections for each of the twelve different superposition maps as well as the estimated values are plotted in Fig. A-11. Again, it is seen that equation (3.5) has made a satisfactory prediction of the signs.

To investigate the validity of equation (3.15), it is necessary to examine the changes in the phase-angle error in an individual reflection with respect to $|G|$ for different superposition maps. The mean phase-angle error as a function of both $|E|$ and $|G|$ for the following maps: sets no. 4, 6, 9, and 11 of the structure CR are listed in Table A-20. The value of corresponding $|G|$ and phase angle error of an individual reflection for each of the twelve maps are also plotted in Fig. A-12. These plots represent six different reflections. On each plot, the horizontal straight line indicates the magnitude of $|E|$ which was a constant for all the twelve maps. The solid curve which connects the 12 round dots shows the value of $|G|$. The dotted line which connects the 12 "+"'s represents the variations in the phase-angle error. From these plots, it is seen that the phase-angle error tends to increase as the value of $|G|$ decreases. But increasing the value of $|G|$ did not affect the phase angle

Table A-19. The test of the fraction of the structure factors determined in sign by G for the structure CR

set no.	# atoms M/2	%extra atoms	%correct atoms	r	%correct[a] phases	N_f	mean[b] error(°)
1	34	25.9	79.4	2.204	85.7	85.65	25.7
2	38	40.7	71.1	1.859	80.7	80.78	32.4
3	42	55.6	64.3	1.673	79.8	80.26	36.0
4	48	77.8	56.3	1.512	80.3	79.91	40.1
5	54	100.0	50.0	1.414	79.8	77.13	42.8
6	62	129.6	43.5	1.331	77.1	77.13	46.4
7	70	159.3	38.6	1.276	77.1	74.00	50.1
8	81	200.0	33.3	1.225	74.0	71.39	54.0
9	94	248.1	28.7	1.845	71.3	70.00	57.0
10	108	300.0	25.0	1.155	70.0	70.00	59.1
11	121	348.1	22.3	1.135	70.0	66.00	60.9
12	135	400.0	20.0	1.118	65.9	66.00	64.5

[a] The value of this percentage was based on 223 relfections of h00,h01, and 001 types only.

[b] The mean phase-angle error was estimated from all of the 1167 reflections.

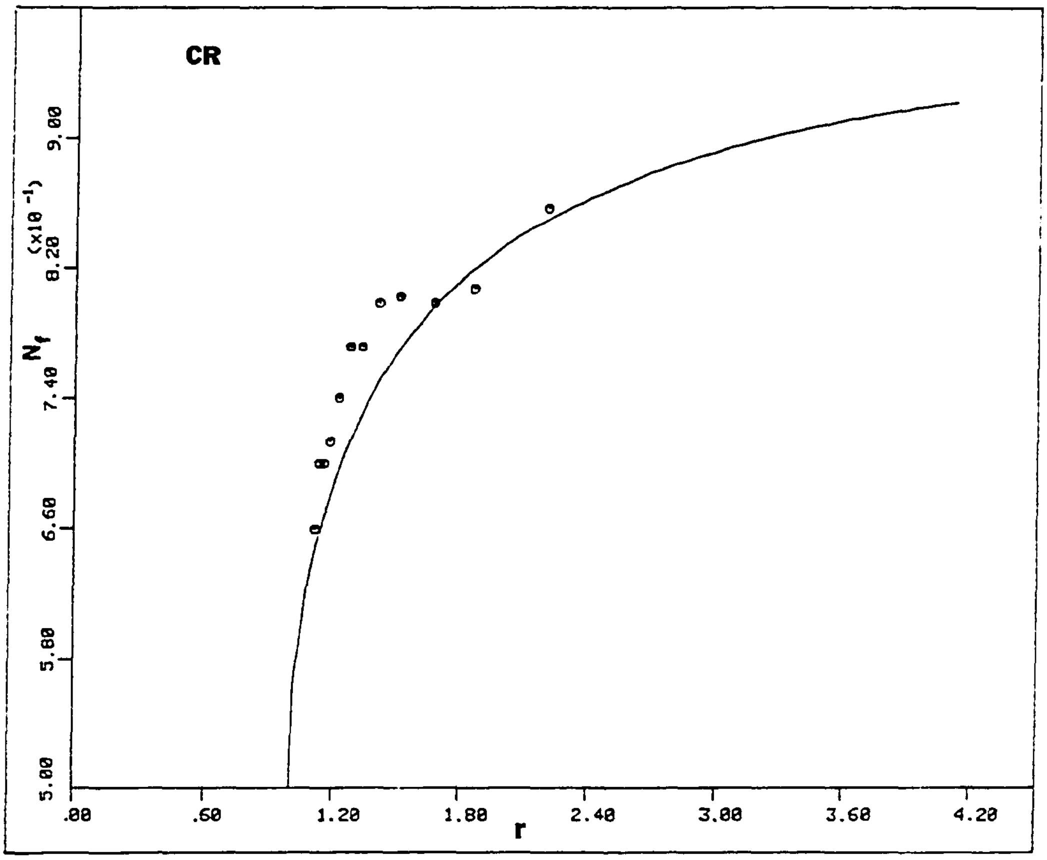

Fig. A-11 The observed (circles) and theoretical (smoothed curve) values of N_f as a function of r for the structure CR.

Table A-20. Mean phase-angle error(°) as functions of both |E| and |G| for different superposition map of the structure CR

G>=

Set 4	2.50	2.25	2.00	1.75	1.50	1.00	0.50	0.00
E>=2.25	1.1	0.9	0.9	5.5	5.5	6.9	6.9	6.9
2.00	1.1	0.8	4.6	6.5	7.3	8.8	8.6	8.6
1.75	3.1	6.5	7.3	8.5	8.3	10.0	10.3	10.3
1.50	3.1	6.6	7.3	9.3	8.9	11.6	12.0	12.5
1.00	3.1	6.1	7.8	10.8	11.5	15.3	19.7	21.3
0.50	3.1	6.4	7.9	11.3	12.5	19.2	26.2	32.2
0.00	2.9	6.1	7.7	11.0	12.4	21.1	31.4	40.1
Set 6								
E>=2.25	7.6	6.5	6.2	6.8	6.5	10.3	10.7	10.7
2.00	7.6	4.6	7.6	8.7	9.5	13.2	14.0	13.6
1.75	6.7	7.8	11.6	12.0	10.8	13.1	16.3	15.6
1.50	6.3	7.3	10.7	12.4	11.3	13.7	17.3	17.7
1.00	5.8	8.2	11.4	13.0	12.8	18.8	25.8	29.5
0.50	5.8	8.2	14.4	14.7	15.7	24.3	35.2	41.0
0.00	5.8	7.9	14.1	15.9	16.4	27.4	40.2	46.4
Set 9								
E>=2.25	5.8	8.5	14.6	12.9	12.9	13.5	19.6	19.6
2.00	5.8	7.8	11.2	10.4	11.1	13.5	21.9	21.6
1.75	9.5	7.9	12.7	18.0	17.2	18.0	26.2	29.5
1.50	9.0	8.7	13.8	16.9	17.0	17.9	26.3	32.9
1.00	13.1	12.5	16.0	17.7	19.0	26.1	36.0	42.7
0.50	13.1	12.1	15.8	19.1	22.8	31.9	44.8	52.0
0.00	10.9	11.4	18.0	25.0	26.1	35.3	49.6	57.0
Set 11								
E>=2.25	9.0	9.0	17.2	13.8	12.6	22.2	21.9	38.8
2.00	8.3	8.8	14.9	15.9	15.5	18.9	24.1	33.4
1.75	32.9	29.5	27.8	23.7	21.0	22.2	27.6	36.9
1.50	29.1	26.0	26.4	22.7	19.4	22.2	30.7	40.8
1.00	27.2	28.3	28.3	28.3	26.1	31.8	40.4	48.5
0.50	27.2	28.3	28.3	30.6	28.4	38.9	49.9	57.5
0.00	27.2	28.1	32.9	32.4	31.2	45.0	54.9	60.9

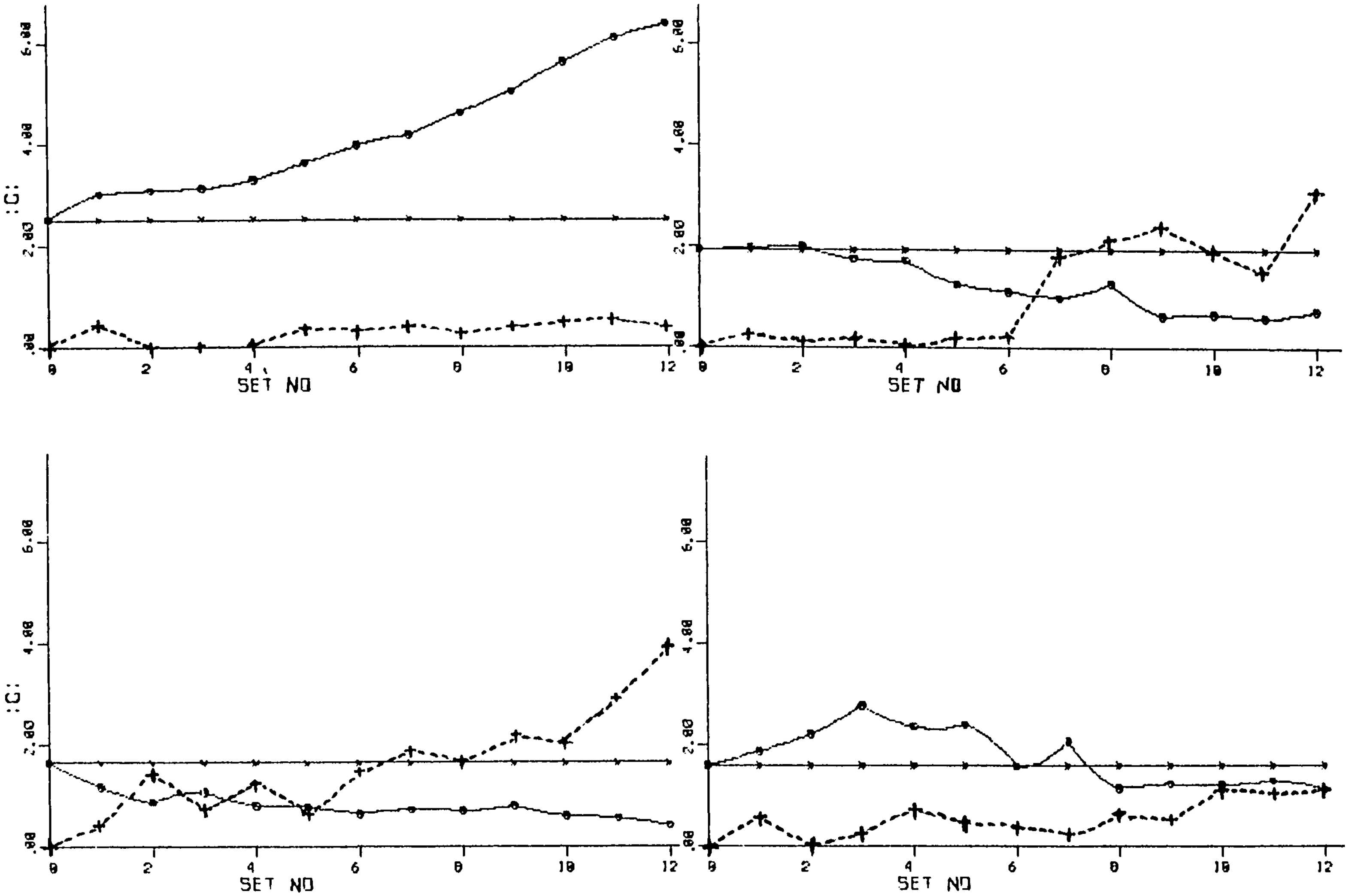
6.00
4.00
2.00
.00
:C:
0
2
4
6
8
10
12
SET NO

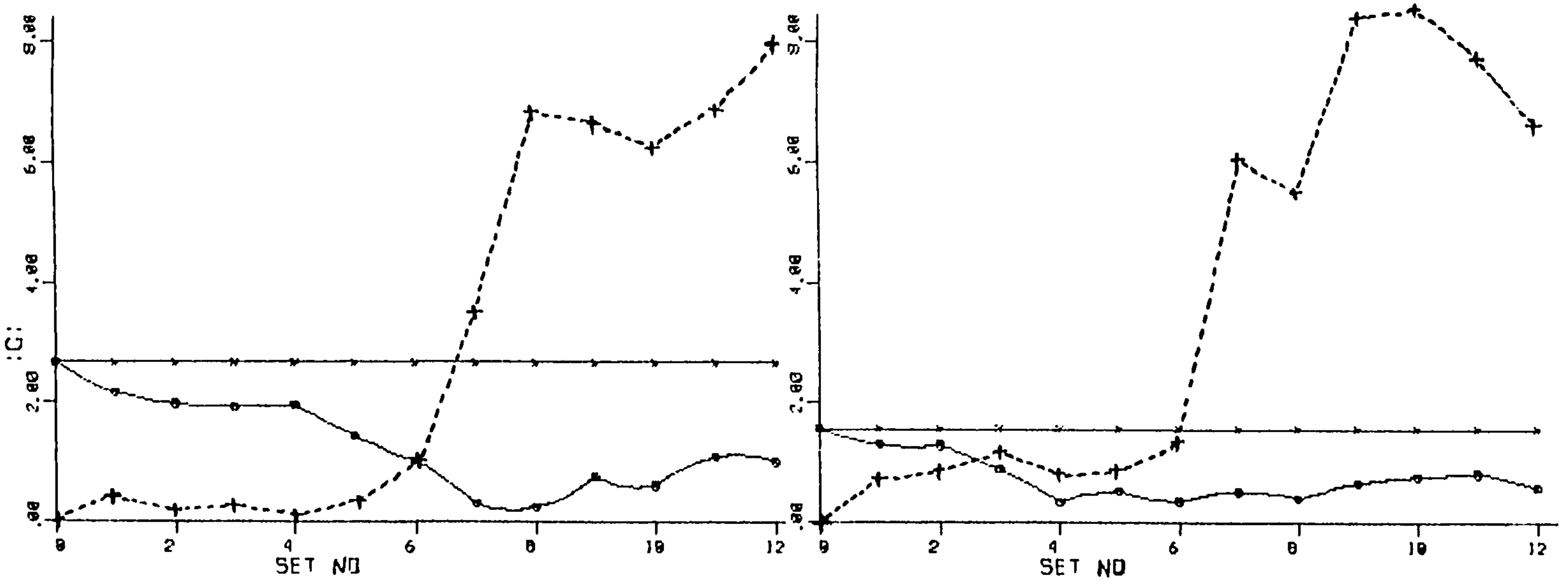

Fig. A-12 Phase-angle error as a function of G for six different reflections. See text for detail.

very much as shown in A-12(a). This observed behavior in the phase-angle errors actually corresponds to that predicted by equation (3.15) and the amount of the change can be estimated for the numbers listed in Table A-3.

The Difference Synthesis Test

It has been discussed in Chapter 6 that a weighted difference synthesis using the quantity (6.6) or (6.7) as Fourier coefficient may result in an electron density map which contains primarily extraneous atoms. This difference synthesis method has been tested using the two centrosymmetric structures, FS and CA.

The structure FS (see Table A-7) contains 13 atoms in an asymmetric unit. A Patterson superposition map was generated by using the Fe-Fe inversion vector, and after a symmetry analysis a list of 60 potential atom coordinates were obtained and used to compute the G's (the highest 26 peaks found on the map are shown in Table A-21). This superposition map was a very good approximation to the real electron density; one can see in the table that all of the real atoms can be found in the top 25 peaks and there were only four interspersed extraneous peaks in the top 13 peaks. In practice, the structure can be readily recognized from the map without ambiguity. This map, however, is a good candidate to answer a basic question about the DS method, can all the extraneous

Table A-21. The results of the difference synthesis test for the structure FS

pk. no.	SUPR[a]	DS[b]	SUPR-DS[c]
1	FE(113)[d]	J1(45)*	Fe(78)
2	S1(84)	FE(35)	S1(60)
3	S2(71)	S1(24)	S2(54)
4	S3(54)	S2(17)	S3(43)
5	J1(41)*	J2(17)*	C1(29)
6	C1(34)	J4(16)*	C3(22)
7	J2(33)*	J10(15)*	O1(22)
8	C2(33)	J6(15)*	C2(21)
9	C3(31)	C5(13)	C4(20)
10	J3(31)*	J3(13)*	C6(20)
11	C4(30)	J8(13)*	J3(18)*
12	C5(27)	C7(12)	C8(17)
13	J4(25)*	C2(12)	C7(17)
14	J5(24)*	J5(12)*	J2(16)*
15	C6(24)	S3(11)	C5(14)
15	J6(23)*	C4(10)	J7(13)*
17	O1(22)	J13(10)*	J5(12)*
18	C7(22)	J7(9)*	J9(12)*
19	J7(22)*	J9(9)*	J11(11)*
20	J8(21)*	C3(9)	J12(10)*
21	J9(21)*	J12(8)*	J4(9)*
22	J10(21)*	J11(7)*	J6(8)*
23	J11(18)*	C1(5)	J8(8)*
24	J12(18)*	C8(1)	J13(7)*
25	C8(17)	C6(0)	J10(6)*
26	J13(17)*	O1 (0)	J1(0)*

[a] Only the highest 26 peaks on the superposition map are listed. Extraneous peaks are indicated by "*"'s.

[b] The peaks in the difference synthesis. Only those which corresponded to the highest 26 peaks on the superposition map are shown.

[c] The difference between the superposition map and the DS map.

[d] The numbers in the parentheses are peak heights at an arbitrary scale. Three maps in the table were set on the same scale.

atoms (in this case, the atoms from J1 to J13 in Table A-21) be disclosed exclusively in the difference synthesis?

Originally it was expected that all the 13 extraneous atoms would be revealed as the highest peaks on the DS map. The 13 extraneous atoms did show up but they were not the top ones on the DS map. Some of the real atoms, such as Fe, S, etc., were still dominant on the difference map. But on closer examination, it was found that the distribution of the extraneous atoms on the DS map was different in that they were more dominant here than on the superposition map. The two maps were then carefully brought to the same scale, and it was found that the difference between the two could yield a better map on which the extraneous atoms were highly suppressed (the peaks on the map are shown in the last column in Table A-21). For example, there was only one extraneous atom, say J3, left among the top 13 peaks. In addition, the peak-height ratios among the real atoms became more reasonable than those on the superposition map.

For the structure CA, a Patterson superposition map was generated using a multiple Mo-Ca vector and 112 peaks (twice of the number of atoms in the unit cell) were used to obtain the G's. On the superposition map, there existed only 9 out of 15 real atoms among the highest 30 peaks. Again the result of the difference synthesis did not clearly distinguish between the extraneous and the real atoms. But the difference

Table A-22. The results of the difference synthesis test for the structure CA

pk. no.	SUPR[a]	DS[a]	SUPR-DS[b]
1	Mo1(158)	Mo1(101)	Mo1(57)
2	*	*	Mo3(42)
3	Mo2(110)	Mo2(68)	Mo2(42)
4	*	*	Mo4(39)
5	Mo3(110)	Mo3(67)	*
6	Mo4(102)	*	Mo5(33)
7	*	Mo4(62)	*
8	*	*	*
9	*	*	O5(21)
10	Mo5(89)	*	*
11	*	*	*
12	*	*	O6(16)
13	*	*	*
14	*	*	*
15	*	Mo5(56)	O1(13)
16	*	*	*
17	*	*	*
18	*	*	*
19	*	*	*
20	O6(60)	*	O7(9)
21	O1(60)	*	*
22	*	*	*
23	*	*	O3(8)
24	O5(59)	*	*
25	*	*	CA(7)
26	*	*	*
27	*	*	*
28	*	*	*
29	O4(52)	*	*
30	*	*	O2(6)

[a] Only the highest 30 peaks on both the superposition map and DS map are listed. Peaks denoted by the "*"'s are extraneous peaks.

[b] The difference between the superposition map and DS map. The numbers in the parentheses are peak heights on an arbitrary scale. All the three maps in the table were set on the same scale.

between the DS map and the superposition map yielded a better map on which 12 real atoms showed up among the top 30 peaks. Although the advantage the difference synthesis is less in practice than they would indicate, it is still a very useful method to use for the elimination of extraneous atoms as long as it can be used in conjunction with the superposition map.

The Consecutive Superpositions Test

This method has been tested on both model and real structures. In this section, an example of a hypothetical two-dimensional structure is given to illustrate how this method would work and what kind of results could be expected.

The structure consists of seven point atoms (see Fig. A-13). A Patterson map was created from all possible interatomic vectors within the structure. It contained 35 peaks including a pair of extraneous peaks which were added. Several superposition maps were subsequently generated using the shift vectors SV1, SV2 and SV3, of multiplicity one, two and three, respectively. The number of quartets found ranged from four to ten. Selected results from steps (1), (3) and (4) which were mentioned in the analysis procedures in Chapter 6 are given below:

<u>Results obtained after step (1)</u> The number of potential quartets from three different superposition maps are listed in Table A-23.

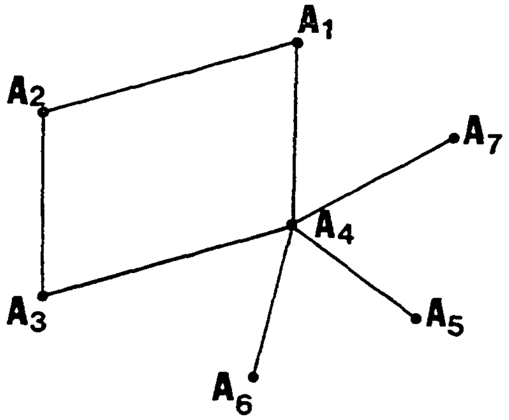

ATOM COORDINATES IN GRIDS

(12X12)

A_1=(0,5)

A_2=(5,7)

A_3=(5,0)

A_4=(0,10)

A_5=(4,0)

A_6=(11,2)

A_7=(4,7)

Fig. A-13 The hypothetical two-dimentional point-atom structure used in the consecutive superpositions test.

Results obtained after step (3) The initial positions of A_2 and A_3 were calculated by selecting the quartet #3 for SV1, #5 for SV2, and #1 for SV3. All the possible atomic coordinates derived from the remaining quartets are listed in Table A-24. The coordinates marked by "X" were considered incorrect because they did not exist on the Patterson map.

Results obtained after step (4) All the possible atomic coordinates in Table A-24 were checked to see if the interatomic vectors among them were consistent with the Patterson peaks. All the solutions are listed in Table A-25.

From the above results, it was obvious that that an isolated image could be readily obtained whether the shift vector was single or multiple. Some comments about this CS method are given below:

(i) Excessive quartets must be eliminated The number of quartets obtained from a superposition map was almost independent of the multiplicity of the shift vector. Since there were always some quartets resulting from extraneous vector peaks, it is better to obtain as small set of the quartets as possible. To achieve this, the shift vector must be carefully chosen. Several potential shift vectors can be used to roughly estimate the number of vector pairs, (V1,V3), before a superposition is really carried out. A better shift vector is the one that generate fewer but still reasonable number of quartets.

The reason for the elimination of excessive quartets is

Table A-23. All possible quartets obtained from three different superposition maps

	SV1[a]	SV2[b]	SV3[c]
1	(5, 2) (11, 0) (1, 0) (7,10)	(5, 2) (1, 0) (11, 0) (7,10)	(5, 2) (5, 7) (7, 5) (7,10)
2	(5, 7) (11, 5) (1, 7) (7, 5)	(5, 7) (1, 5) (11, 7) (7, 5)	(4, 2) (4, 7) (8, 5) (8,10)
3	(11, 9) (5, 7) (7, 5) (1, 3)	(0, 5) (8, 3) (4, 9) (0, 7)	(7,10) (7, 3) (5, 9) (5, 2)
4	(7,10) (1, 8) (11, 4) (5, 2)	(4, 7) (0, 5) (0, 7) (8, 5)	(11, 0) (11, 5) (1, 7) (1, 0)
5	(7, 3) (1, 1) (11,11) (5, 9)	(11, 9) (7, 7) (5, 5) (1, 3)	(6, 2) (6, 7) (6, 5) (6,10)
6	(6, 7) (0, 5) (0, 7) (6, 5)	(11, 5) (7, 3) (5, 9) (1, 7)	(11, 7) (11, 0) (11, 4) (11, 9)
7	(11, 0) (5,10) (7, 2) (1, 0)	(11, 4) (7, 2) (5,10) (1, 8)	(11, 4) (11, 9) (1, 3) (1, 8)
8	(11, 7) (5, 5) (7, 7) (1, 5)		(4, 9) (4, 2) (8,10) (8, 3)
9	(5, 9) (11, 7) (1, 5) (7, 3)		(7, 2) (7, 7) (5, 5) (5,10)
10			(1, 8) (1, 1) (11,11) (11, 4)

[a] SV1=A_6-A_3 (a single vector).

[b] SV2=$A_7-A_1=A_5-A_4$ (a double vector).

[c] SV3=$A_1-A_4=A_2-A_3=A_7-A_5$ (a triple vector).

Table A-24. Atomic coordinates derived by using the quartet relation in Table A-23

ATOM[a]	SV1	SV2	SV3
A1	(0, 0)	(0, 0)	(0, 0)
A2	(11, 9)	(11, 9)	(5, 2)
A3	(5, 7)	(7, 7)	(5, 7)
A4	(6, 7)	(6, 7)	(1, 0) X
A4′	(10, 8) X[b]	(0, 9) X	(9, 9) X
A5	(6, 2)	(6, 2)	(10, 4) X
A5′	(4, 0) X	(0, 2) X	(0, 5)
A6	(4,11) X	(11, 4)	(6, 2)
A6′	(0, 5)	(7, 0)	(4, 7)
A7	(4, 6) X	(7, 2)	(11, 0)
A7′	(0, 9) X	(11, 2) X	(11, 9)
A8	(5, 2)	(0, 4) X	(6, 7)
A8′	(11, 2) X	(6, 0) X	(4, 2)
A9	(0, 9) X	(0, 5)	(6,10)
A9′	(4, 7)	(6,11)	(4,11) X
A10	(0. 2) X		(1, 5)
A10′	(4, 2)		(9, 4) X
A11	(6, 0) X		(10, 0) X
A11′	(10, 3) X		(0, 9) X
A12			(4, 6) X
A12′			(6, 3) X

[a] Atoms which are denoted by primes belong to the corresponding inverse structure. Atoms greater than seven are extraneous atoms.

[b] The symbol "X" indicates wrong coordinates.

Table A-25. All possible solutions obtained by using the quartet relation

shift vector		Solutions[a]
SV1	#1	$A_1,A_2,A_3,A_6,A_8,A_9',A_{10}'$
	#2	A_1,A_2,A_3,A_4,A_5,A_6
	#3	$A_1,A_2,A_3,A_4,A_6,A_{10}$
SV2	#1	$A_1,A_2,A_3,A_4,A_5',A_6,A_7$
	#2	A_1,A_2,A_3,A_4,A_6,A_8
SV3	#1	$A_1,A_2,A_3,A_5',A_6',A_7',A_8'$
	#2	$A_1,A_2,A_3,A_4,A_5,A_8,A_9,A_{10}$
	#3	A_1,A_2,A_3,A_5,A_7,A_8
	#4	A_1,A_2,A_3,A_5,A_7,A_9

[a] The atoms which are denoted by primes belong to the corresponding inverse structure. Atoms greater than seven are extraneous atoms.

twofold. One is to decrease the possibility of picking up a non-valid quartet to initiate "wrong" coordinates for A_2 and A_3. The other is to avoid introducing extraneous atoms in the final solution.

(ii) The atoms derived from the quartet relation may contain fewer extraneous peaks than that from two consecutive superpositions   The results obtained after performing step (3) were compared with the image singled out by two consecutive superpositions using A_2-A_1 and A_3-A_1 as shift vectors. The vector set derived form the quartet relation was the same as or only a subset of the one from the regular superposition procedure. This was probably due to the quartet relation which resists many extraneous vectors peaks on the superposition map.

(iii) Multiple solutions are expected   There was usually more than one solution for the structure as can be seen in Table A-25. Any one of these can be used to obtain the G's to proceed with phase refinements. If the crystal symmetry has a higher symmetry than P1, one may try to apply the symmetry analysis procedure to find unit cell origin and eliminate those peaks which are not consistent with the required symmetries.

(iv) No symmetry is required   Throughout the procedure, no symmetry was required to obtain the solutions. This method may be very useful for those structures which are noncentrosymmetric and of low symmetry.

Application of the Hybrid Approach to the Solution of Real Structures

The application of our hybrid approach to the solution of four real structures is presented in this section. The first two structures, CA and IN (see Table A-7 for detail), were previously solved by other methods.[48,51] The other two structures, GD and AS, were unknown before they were solved using this new approach. For all of these four structures, the Patterson superposition functions were generated using our FORTRAN program SUPR.[56] These functions were then "refined" by the symmetry analysis (mentioned in Chapter 6) to obtain possible unit cell origins and select peaks which were consistent with the space group symmetry. These peaks were then used to obtain the pseudo-normalized structure factors G according to equation (7.1). The normalized structure factors E were calculated by using the normalization program in MULTAN.

The modified tangent formula (or the E-G relation) phase refinement, which was previously described in Chapter 5, was ultilized to obtain phase solutions for all the structures. Major procedures, results, and discussions are given in the following.

Structure solutions for IN and CA

The structures IN and CA are known structures. In the structure IN, there were only five atoms in an asymmetric unit. The reason to choose this as one of the test structures is because of its high crystal symmetry. Since it consists of repeating metal cluster chains, on the Patterson map the first 20 strong peaks were all multiple or overlapping vectors of In-Mo, Mo-Mo, and Mo-O types. An unweighted Patterson superposition map was generated by using the fifth highest vector (an arbitrary choice) as the displacement vector. This vector was later analyzed as a composite of one fourfold Mo-O and one twofold In-Mo vector. The Patterson superposition map was first refined by a symmetry analysis and then the top 42 peaks (two times of the number of atoms in the unit cell) were used to compute the G's. For structure CA, the same Patterson superposition function, which was mentioned on page 80, was used.

For both of the structures, the phase refinement proceeded as follows:

(a) Set up an initial E phase set. This was done by assigning the phases of the G to the E for reflections with both $|E|\geq 1.5$ and $|G|\geq 1.5$. The size of the initial E phase set was about one tenth of the total reflection number.

(b) Sort the initial G phase set. The G set was sorted in sequence with respect to both the magnitude of the G and the magnitude of $G^2/|E|$. The purpose of this arrangement was to include the best G's in the refinement in the early stage. The size of the G set was also cut down by eliminating those reflections with $|G| \leq 0.3$ in IN and $|G| \leq 0.5$ in CA.

(c) Obtain new signs using equation (5.3). In the first cycle, unit weight was applied to all the signs in the E set. The new signs for reflections with $|E| \geq 0.3$ in IN and $|E| \geq 0.5$ in CA were computed and only those signs which resulted from more than three contributors (or s2rs) were accepted. The initial E phase set was then expanded by including these reflections with their new signs.

(d) Obtain new signs using equation (5.15) in the second cycle. All weights were considered to be unity. In this cycle, the value of $|E|$ replaced the value of the corresponding $|G|$ and then entered into the refinement again.

Only two cycles were tried for both structures and all of the new signs were accepted without any discrimination. The distributions of correct signs after the phase refinement for both structures are summarized in Table A-26(a). The percentage was computed according to the total number of reflections occurring in each class. These signs were also combined with the $|E_{obs}|$'s to compute E-maps and the results

Table A-26. Results of the phase refinement obtained by using the E-G relation for the structures IN and CA

(a) Sign distribution (%) after phase refinement

$X=\|E\|$	structure IN % correct signs	structure CA % correct signs
$X>2.0$	97%	100%
$2.0>X\geq1.5$	94%	75%
$1.5>X\geq1.0$	90%	65%
$1.0>X\geq0.5$	59%	79%

(b) Comparison of the results in real space before and after phase refinement

	structure CA		structure IN	
	SUPR[a]	E map[b]	SUPR	E map
pk. no.	atom	atom	atom	atom
1	Mo1(286)[c]	Mo5(654)	Mo1(350)	In1(568)
2	Mo3(262)	Mo2(620)	In1(296)	Mo1(498)
3	*	Mo1(588)	*	Mo2(478)
4	*	Mo3(569)	Mo2(289)	O1(89)
5	Mo5(232)	Mo2(549)	*	O2(73)
6	Mo4(180)	Ca2(304)	*	
7	*	O2(202)	*	
8	*	O3(164)	O1(253)	
9	*	O1(147)	*	
10	O6(124)	O5(129)	*	
11	*	O4(118)	*	
12	*	O6(110)	*	
13	*	O7(109)	*	
14	Ca2(90)	O8(109)	*	

[a] The highest 14 peaks on the "refined "Patterson superposition function after the symmetry analysis.

[b] The highest 14 peaks on the E-map which was calculated by using the phases obtained from the phase refinement.

[c] Peak heights are on an arbitrary scale.

are shown in Table A-26(b). Only the top 14 peaks (non-symmetry related ones) are listed in the table. It can be seen that the complete images were obtained for both structures and the difference between the E-map obtained after the phase refinement and the superposition map was striking; all the atoms in the structure were found in the E-map and the peak-height ratios also became more reasonable.

It may be noticed that on the Patterson superposition maps (see Table A-26(b)) of both IN and CA the major part of a structural image already existed. This really accounted for the success of only two cycles of phase refinement. A few more cycles of refinement may be needed if the starting Patterson superposition functions are not as good as the ones that were used in the above tests.

Structure solution for GD

The structure GD, $Gd_4Mo_4O_{11}$,[57] was crystalized in an orthorhombic space group symmetry Pbam and it consisted of 15 atoms: four Gd's, three Mo's, and eight O's in an asymmetric unit. Before the structure had been solved and its magnetic susceptibility was measured, the compound was thought to be a La-containing[58] molybdenum oxide and $LaMo_4O_8$ are used as an initial estimate of its empirical formula.

On its Patterson map, most of the peaks were anomalously broad as most "peaks" consisted of two or more maxima. Perhaps this was due to the nature of the structure itself and to the poor quality of the intensity data (the crystal was a twin). Thus peak positions could not be determined accurately. Several different Patterson superposition maps were generated using different displacement vectors. Finally a map which was generated by using the vector with a height of 4.2% of the origin peak and ~2.9Å in length was chosen and the top 108 peaks which were consistent with the space group symmetry were used to obtain the G's.

The difference synthesis method was subsequently used to modify the superposition function and the new G's were obtained after applying one cycle of the difference synthesis. The new G's were then entered into the phase refinement via equation (5.3). In the refinement, the starting E phase set was obtained by a direct sign transfer in which the limiting value of 1.0 was chosen for both $|E|$ and $|G|$. Only one cycle of the refinement was undertaken and new signs for all reflections with $|E|\geq 0.5$ were accepted with unit weight. An E-map was subsequently computed. The results of the DS method and the phase refinement are shown in Table A-27.

It can be seen that before using the DS method, there were only five peaks which appeared at positions roughly about those of the real atoms. The difference synthesis did make an improvement in that two more peaks appeared at real atom sites. At this stage, the top two or three peaks had been entered into a least-squares refinement using the ALLS program[59] in which all of the atoms were regarded as Mo's, but

Table A-27. Comparisons of the results obtained at different stage in the hybrid procedure for the structure GD

pk.no.	SUPR	SUPR-DS	E-map
1	Gd(1)	Gd(1)	Gd(1)
2	*	Gd(2)	Mo(2)
3	Gd(2)	~Mo(2)	Gd(2)
4	*	*	*
5	*	*	*
6	*	*	*
7	*	*	*
8	*	~Gd(4)	~Gd(4)
9	*	*	Mo(1)
10	*	*	*
11	*	*	~Mo(3)
12	~O(1)[a]	*	~O(2)
13	*	*	*
14	*	*	*
15	*	*	*
16	*	*	*
17	*	*	*
18	~Mo(2)	*	Gd(3)
19	*	~Gd(3)	*
20	*	*	*
21	*	~Mo(3)	*
22	~Gd(4)	*	*
23	*	*	*
24	*	*	~O(3)
25	*	~O(2)	*
26	*	*	*
27	*	*	~O(5)

[a] The symbol "~" indicates that the peak position roughly corresponded to that of a real atom (but was a little beyond a specified tolerance).

the agreement factor was always in the vicinity of 58%. After the phase refinement, the first 10 peaks on the final E-map were entered into the least-squares refinement again with all atoms regarded as Mo's; the R-factor became approximately 38%. The rest of the structure was then solved by regular difference synthesis.[60]

A few comments about the solution of the structure GD are given below:

1. Both MULTAN and the ALCAMP procedure[61] had failed to give the correct solution before the structure was solved by the hybrid method. However, it was discovered later that if a closer guess of the structural composition had been made and that if the scattering factor of the Gd atom were used instead of that of La, the structure could be solved by MULTAN with the use of the SWTR scheme.[62]
2. The success of direct methods is usually very sensitive to the |E| values.[63] As was mentioned before the intensity data were collected from a twin crystal and the wrong scattering factor used (the difference in Z is 7 between La and Gd); these certainly made the estimated |E| values worse than they should be such that not only had MULTAN failed but also the results obtained from the E-G refinement were not as good as was expected.
3. Two more cycles of the phase refinement were also tried but the final solution was about the same as the earlier one except that the peak-height ratios for those real

atoms became more reasonable. The reason why the phase solution did not improve was investigated and two explanations can be advanced. First, only 80% of the signs in the starting E set were correct (see Table A-28.(a)). Because these signs had unit weights througout the refinement, wrong signs propagated fast enough to cancel out newly obtained correct signs. Second and more likely, both the |G| and |E| values were poor due to the reasons noted above which caused MULTAN to fail.

4. Our hybrid method was superior to MULTAN or complete Patterson-based techniques as far as this structure solution was concerned. It has been demonstrated that with a roughly measured intensity data and without knowing the correct composition plus a significantly wrong scattering factor, it was still possible to solve the structure by the hybrid method.

Structure solution for AS

The compound AS, KSi_3As_3[64], crystallized in the orthorhombic space group symmetry Pbam and it consisted of seven atoms: three As's, three Si's, and one K in an asymmetric unit. The composition of this structure was thought as K_2SiAs_2 and both MULTAN and ALCAMP failed to give correct structure solutions.

It is a layer structure and thus most of the Patterson peaks reside at planes with z=0 or z=1/2. A vector peak which

Table A-28. Wrong-sign distribution (%) as functions of |G| and |E| in the structures GD and AS

(a) Structure GD: 654 reflecton in total

E \ G|	2.50	2.25	2.00	1.75	1.50	1.00	0.50	0.00
2.25|	0.0	0.0	0.0	0.0	0.0	0.0	0.0	0.0
2.00|	0.0	0.0	0.0	0.0	0.0	0.0	0.0	21.1
1.75|	0.0	0.0	0.0	0.0	0.0	0.0	14.8	41.0
1.50|	0.0	0.0	0.0	0.0	0.0	4.3	19.6	47.2
1.00|	0.0	0.0	0.0	0.0	0.0	19.6	28.6	46.5
0.50|	0.0	0.0	0.0	0.0	6.7	26.4	36.9	50.8
0.00|	0.0	0.0	0.0	0.0	5.9	29.9	37.4	49.8

(b) Structure AS: 674 reflections in total

E \ G|	2.50	2.25	2.00	1.75	1.50	1.00	0.50	0.00
2.25|	0.0	0.0	0.0	0.0	0.0	0.0	0.0	18.2
2.00|	0.0	0.0	0.0	0.0	0.0	0.0	0.0	8.0
1.75|	0.0	0.0	0.0	0.0	0.0	0.0	0.0	9.8
1.50|	0.0	0.0	0.0	0.0	0.0	0.0	2.0	13.2
1.00|	0.0	0.0	0.0	0.0	0.0	0.0	5.4	19.7
0.50|	0.0	0.0	0.0	0.0	0.0	1.3	16.0	31.3
0.00|	0.0	0.0	3.3	2.4	2.0	3.4	20.2	34.3

was the strongest in height among all vectors of bonding distance (2.4±0.1 Å) was selected to generate a superposition map. After symmetry analysis, the G's were computed from the top 88 peaks on the map.

The solution was obtained immediately from the SS method (mentioned in Chapter 6) in which the γ'-synthesis was used. At this stage, six atoms were found and they were thought to be K_2SiAs_3 according to their peak-height ratios. Later E-G phase refinement was undertaken in which the initial E phase set was obtained by transferring the signs of the G's to the E's for those reflections with both $|E|$ and $|G|$ greater than 1.0. After one cycle of phase refinement, an E-map was computed using reflections with $|E|>0.5$. The structure was then unambigiously solved (see Table A-29).

After the structure was solved by the above procedure, MULTAN was tried again. It was found that with correct composition, it could give a solution in which six real atoms could be located from the top 10 peaks on the E-map except that three of them had y-coordinates off by 0.10 or 0.15 (fractional). The success of our hybrid procedure, in this case, probably lies in the fact that the structural information buried in the Patterson superpositon function helped the establishment of enough correct signs in the E's (see Table A-28.(b)) that one cycle of the phase refinement via the E-G relation yielded the correct phase solution.

Table A-29. Comparisons of the results obtained at different stage in the hybrid procedure for the structure AS

pk. no.	SUPR	SS[a]	E-map
1	*	As(3)	As(2)
2	*	As(2)	As(3)
3	As(1)	As(1)	As(1)
4	*	K(1)	K(1)
5	*	*	Si(2)
6	As(2)	Si(2)	Si(1)
7	*	*	Si(3)
8	Si(2)	*	
9	K(1)	*	
10	*	*	
11	*	Si(1)	
12	Si(1)		
13	As(3)		
14	*		
15	*		
16	*		
17	*		
18	*		
19	*		
20	*		
21	*		
22	*		

[a] The results were obtained from the superpositional synthesis. The peaks found were assigned the corresponding real atom symbols.

CHAPTER 8. SUMMARY

The basic theory of the hybrid Patterson-superposition/direct-method as well as the probability theory of the triple-phase structure invariants in which the pseudo-normalized structure factors G participate have been derived. The validity of the Σ_2-like relation was proven to be very effective in both centrosymmetric and noncentrosymmetric structures and the use of this relation in real structure solutions were also very successful.

An algorithm of this hybrid method may be given as follows:

Algorithm:

```
1. Calculate $|E_{obs}|$ from the intensity data.
2. Calculate $P(\vec{r})$ from the intensity data.
3. Select an adequate displacement vector from $P(\vec{r})$ to
   obtain $M_2(\vec{r})$.
4. If any symmetry element other than the identity is
   known to exist, then goto 6.
5. Apply the CS method and then goto 7.
6. Perform symmetry analysis on $M_2(\vec{r})$ to find the unit
   cell origin and select peaks which correspond to the
   required symmetries to form a new $M_2(\vec{r})$.
7. Calculate the Fourier coefficients of $M_2(\vec{r})$, G.
8. Apply the SS or DS method and compute new G's, if
   necessary.
```

9. Calculate $P_+(|G||E|)$ or $P(\xi)$ for the G's.
10. Form initial E phase set from the G's.
11. Perform E-G phase refinement for one or two cycle(s).
12. Compute an E-map according to the phase solution obtained from 11.
13. Analyze the E-map and do least-squares refinements.
14. If the solution is not correct then:
    a) goto 11 if no more than five cycles of refinement have been tried.
    b) goto 8 if no more than three cycles of SS or DS have been tried.
    c) goto 6 if no more than six origin choices have been tried.
    d) goto 3.
15. Stop

As can be seen from the argorithm the Patterson superposition function plays a very important role in this hybrid method. Three different methods for the construction of better M_{ps} functions have been studied. These functions are usually closer to the true electron density and hence better phases of the G's can be obtained.

Because of the use of a large G phase set, the refinement of the phases converges very fast. It is found that usually less than five cycles are required to produce a good phase set from which the correct structure can be obtained. Although the squaring effect[65] is not as sigificant as that in the tangent refinement in which only the E's are involved, it is better to refine the phases no more than five cycles to avoid this effect as much as possible.

Although it is desirable that the Patterson superposition function be close to the true electron density, it does not mean that this function should provide a "recognizable" fragment of the structure. This point has made the new method distinct from either Patterson-based techniques or direct methods in which partially known structures are required.

A major advantage of this new hybrid approach over other methods is the capability to accommodate false atoms in the phase refinement. Thus, not only Patterson superposition functions, but also any other kind of electron density function, from which the true structural image cannot be recognized readily and which is obtained as a result of MULTAN or other methods, can directly enter into the hybrid procedure to obtain complete structural solutions.

REFERENCES

1. A. L. Patterson, Phys. Rev. 46, 372 (1934).
2. D. M. Wrinch, Phil. Mag. 27, 98 (1939).
3. M. J. Buerger, Vector Space (Wiley, New York, 1959).
4. R. A. Jacobson, J. A. Wunderlich, and W. N. Lipscomb, Nature, London 184, 1719 (1959).
5. J. Donohue, L. R. Lavine and J. S. Rollett, Acta Crystallogr. 9, 655 (1956).
6. R. A. Pasternak, L. Katz, and R. B. Corey, ActaCrystallogr. 7, 225 (1954).
7. R. A. Jacobson, Trans. Am. Cryst. Assoc. 2, 39 (1959).
8. D. Harker and J. S. Kasper, Acta Crystallogr. 1, 70 (1948).
9. G. Germain and M. M. Woolfson, Acta Crystallogr. 21, 845 (1966).
10. V. I. Simonov, Acta Crystallogr. B25, 1 (1969).
11. M. F. C. Ladd and R. A. Palmer, Theory and Practice of Direct Methods in Crystallography (Plenum Press, New York, 1980).
12. P. Main, S. J. Friske, S. E. Hull, L. Lessinger, G. Germain, J-P, Declercq, and M. M. Woolfson, MULTAN 80. A System of Computer Programs for the Automatic Solution of Crystal Structures from X-ray Diffraction Data. (Univ. of York, York, England, 1980).
13. G. M. Sheldrick in Computing in Crystallography, Ed. H. Schenk (Delft University Press, 1978), pp. 34-42.
14. P. T. Beurskens, V. den Hark, Th. E. M. and G. Beurskens, Acta Crystallogr. A32, 82 (1976).
15. H. Hauptman and J. Karle, Acta Crystallogr. 15, 547 (1962).
16. R. K. Wismer and R. A. Jacobson, Acta Crystallogr. B28, 3457 (1972).

17. (a) G. Allegra, *Acta Crystallogr.* *A35*, 213 (1979).

    (b) G. Allegra, *Acta Crystallogr.* *A39*, 273 (1983).

18. D. Harker and J. S. Kasper, *Acta Crystallogr.* *1*, 70 (1948).

19. J. Karle and H. Hauptman, *Acta Crystallogr.* *3*, 181 (1950).

20. J. A. Goedkoop, *Acta Crystallogr.* *3*, 374 (1950).

21. D. Sayre, *Acta Crystallogr.* *5*, 60 (1952).

22. E. W. Hughes, *Acta Crystallogr.* *6*, 871 (1953).

23. J. Karle and H. Hauptman, *Acta Crystallogr.* *9*, 635 (1956).

24. (a) R. A. Jacobson, *Crystallographic Computing*, Ahmed F. R., Ed. (Munksgaard, Copenhagen, Demark, 1970), pp. 81-6.

    (b) R. A. Jacobson, J. A. Wunderlich and W. N. Lipscomb, *Acta Crystallogr.* *14*, 598 (1961).

25. W. Cochran and M. M. Woolfson, *Acta Crystallogr.* *8*, 1 (1955).

26. D. Sayre, *Acta Crystallogr.* *5*, 60 (1952).

27. W. Cochran, *Acta Crystallogr.* *5*, 65 (1952).

28. H. Cramer, *Random Variable and Probability Distributions* (University Press, Cambridge, 1937), pp. 56-60.

29. G. A. Sim, *Acta Crystallogr.* *10*, 177 (1957).

30. M. M. Woolfson, *Acta Crystallogr.* *9*, 804 (1956).

31. G. A. Sim, *Acta Crystallogr.* *12*, 813 (1959).

32. W. Cochran, *Acta Crystallogr.* *8*, 473 (1955).

33. H. Hauptman, and J. Karle, *The Solution of the Phase Problem. I. The Centrosymmetric Crystal*, A.C.A. Monograph No. 3. (The Letter Shop, Wilmington, 1953).

34. J. Karle and H. Hauptman, *Acta Crystallogr.* *9*, 635 (1956).

35. J. Karle, *Acta Crystallogr.* *B24*, 182 (1968).

36. D. M. Blow, and F. H. C. Crick, *Acta Crystallogr.* *12*, 794 (1959).

37. G. Germain, P. Main and M. M. Woolfson, *Acta Crystallogr.* *A27*, 368 (1971).

38. R. O. Gould, Th. E. M. van den Hark, and P. T. Beurskens, *Acta Cryatallogr.* *A31*, 813 (1975).

39. Th. E. M. van den Hark, P. Prick and P. T. Beurskens, *Acta Crystallogr.* *A32*, 816 (1976).

40. P. T. Beurskens, P. A. J. Prick and H. M. Doesburg, *Acta Crystallogr.* *A35*, 765 (1979).

41. See p.247 in Reference 3.

42. G. N. Ramachandran & R. Srinivasan, *Fourier Methods in Crystallography* (Wiley-Interscience, London, 1970).

43. The superpositional synthesis is different from that of Simonov's (see reference 10) in that known atom positions are not required in our SS method.

44. G. N. Ramachandran and S. Raman, *Acta Crystallogr.* *12*, 957 (1959).

45. A. R. Kalyanaraman, S. Parthasarathy, and G. N. Ramachandran In *Physics of the Solid State*, edited by S. Balakrishna, M. Krishnamurthy and B. Ramachandra Rao (Academic Press, New York, 1969), pp. 63-67.

46. P. Main, *Acta Crystallogr.* *A35*, 779 (1979).

47. G. A. Sim, *Acta Crystallogr.* *13*, 511 (1960).

48. R. E. McCarley, K. H. Lii, P. A. Edwards, and L. F. Brough, *J. Solid State Chem,* *57*, 17 (1985).

49. J. R. Matachek, Ph.D. Dissertation, Part II. Iowa State University, Ames, Iowa, 1985.

50. S. L. Wang and R. A. Jacobson, unpublished research, Department of Chemistry, Iowa State University, Ames, Iowa, 1985.

51. K. H. Lii, Ph.D. Dissertation, Section 2. Iowa State University, Ames, Iowa, 1985.

52. J. W. Richardson, Ph.D. Dissertation, Appendix B. Iowa State University, Ames, Iowa, 1984.

53. The square-root of the peak height may be scaled such that the highest value corresponds to the heaviest atomic number.

54. N. V. D. Putten and H. Schenk, Acta Crystallogr. A36, 891 (1980).

55. R. Bagio and M. M. Woolfson, Acta Crystallogr. A34, 883 (1978).

56. C.R. Hubbard, M. W. Babich and R. A. Jacobson, U.S. E.R.A.D.A Research and Development Report, IS-4106, 1977.

57. K. H. Lii, Ph.D. Dissertation, Section 3. Iowa State University, Ames, Iowa, 1985.

58. The sample vial of one of the starting materials Gd_2O_3 was mislabled as La_2O_3.

59. R. L. Lapp and R. A. Jacobson, U.S. D.O.E Research and Development Report, IS-4708, 1979.

60. D. R. Powell and R. A. Jacobson, U.S. D.O.E. Research and Development, IS-4737, 1980.

61. J. W. Richardson, Ph.D. Dissertation, Iowa State University, Ames, Iowa, 1984.

62. S. E. Hull and M. J. Irwin, Acta Crystallogr. A34, 863 (1978).

63. S. R. Hull and V. Subramanian, Acta Crystallogr. A38, 598 (1982).

64. W. M. Hurng and J. D. Corbett, unpublished research, Department of Chemistry, Iowa State University, Ames, Iowa, 1985.

65. J. Gassmann and K. Zechmeister, Acta Crystallogr. A28, 270 (1972).

SECTION B

IN-LAB EXAFS TECHNIQUES

CHAPTER 1. INTRODUCTION

Introduction

The phenomenon of EXAFS has been known for over 50 years, but only recently has its power for structure determination been appreciated. The renascence of this rather old X-ray absorption technique has been attributable to both the theoretical advances made by Stern[1] and the advent of synchrotron radiation sources. In the last decade, after it was shown that EXAFS can be utilized to obtain information on the atomic arrangement of materials[2] (particularly the short-range interatomic correlations in complex systems), EXAFS measurements have experienced a tremendous growth. The feature of EXAFS that makes it attractive is its capability to measure the atomic arrangement around a chosen atom type independent of whether the material is crystalline or not. This new technique has made feasible structure determination on systems that were not amenable to the more standard techniques.

In the past few years, the availability to the general scientific community of EXAFS facilities at synchrotron radiation laboratories has lead to a spectacular growth in the application of the technique. As the demand to do EXAFS measurements increased and outstripped available facilities, there began a trend to develop techniques for doing the EXAFS measurements in the laboratory reviving a technology that had almost disappeared. Modern instruments which take full advantage of computer technology and modern electronics have made in-lab EXAFS measurements feasible.

From many studies[3] it has been shown that an in-lab EXAFS apparatus using either rotating anode or fixed anode source is feasible covering the X-ray range from about 2.5 - 20 KeV with an energy resolution spanning 1 - 20 eV. This laboratory facility is as adequate as the synchrotron source for measuring EXAFS on samples that are concentrated enough to use the transmission mode within this energy range. Fluorescence experiments can also be performed, but the dilution limits are, as yet, undetermined. The most significant advantage for the in-laboratory system is that the experiment can be performed at any time when needed (this is almost impossible with a synchrotron source). This can be extremely important at a research laboratory where knowledge of an atomic arrangement may be of immense importance as part of some theoretical or technical development.

Because of the nature of X-ray sources, in-lab EXAFS techniques are more complicated than those employed at a synchrotron radiation laboratory. First of all, the spectrum of the radiation of an X-ray tube contains characteristic lines originating from the target material and contaminants. These can seriously deteriorate the quality of certain EXAFS requirement. Second, a single bent-crystal spectrometer with

Rowland circle geometry is used in order to achieve maximum focusing. Third, a series of bent monochromators with various d-spacings are employed to produce wide energy ranges. Fourth, pulse detectors and shaping electronics are used to provide the capability of energy discrimination.

In this part of this thesis, the construction and development of an in-lab EXAFS facility in the Ames Laboratory are described. These primarily include: (a) spectrometer alignment, (b) automation, (c) tests of the electronic detector systems, (d) improvement of the energy resolution, and (e) development of both data acquisition and data reduction programs.

In the following sections, a qualitative description of the EXAFS theory, EXAFS measuring techniques and data analysis methods are briefly introduced. General considerations for in-lab EXAFS experimentation are also briefly discussed in Chapter 2. The test results which were obtained from our in-lab EXAFS system are presented and discussed in Chapter 3. Finally, a summary is given in Chapter 4.

EXAFS Description

The origin of the EXAFS is very well understood by now.[4,5] Theories of EXAFS based on the short-range single-electron single-scattering model has been discussed at length in the literature.[1,6,7] A qualitative description of EXAFS is given below:

The absorption coefficient for the photoexcitation of an electron from the K shell of atom type α can be written as

$$\mu(E) = \mu_0(E)[1 + \chi(E)], \qquad (1.1)$$

where E is the X-ray photon energy. The μ_0 factor in equation (1.1) is similar to the absorption coefficient observed for free atoms, but is essentially featureless except for the threshold. χ expresses the modulation of the photoexcitation rate arising from changes in the photoelectron wave function in the core region caused by interference between the outgoing portion of the wave function and that small fraction of the wave which is scattered back from near-neighbor atoms. This modulation yields the oscillations in μ with increasing photon energy which are known as the EXAFS. The oscillations in the interference result from the energy dependence of the phase difference between the outgoing and backscattered waves. The principal contribution to this phase difference is simply the product of the photoelectron momentum k and the round-trip distance 2r to a near neighbor. There are also energy-dependent contributions to the phase arising from the excited atom and backscattering atom potentials. Finally, the amplitude of the backscattered electron wave depends on the backscattering strength of the near-neighbor atom potential and on the attenuation of the electron wave in traveling the distance 2r. Combining these elements, the EXAFS for a randomly oriented local environment in k space can be expressed as

$$\chi(k) = \Sigma\, N_j F_j(k) \exp(-2\sigma_j{}^2 k^2) \exp[-2r_j/\lambda(k)]$$

$$\times\ \frac{\mathrm{Sin}(2kr_j + \phi_j(k))}{kr_j^2}. \qquad (1.2)$$

In this expression,

$$E = E_o + (h^2k^2/8m\pi^2). \qquad (1.3)$$

E_o is the final-state electron energy corresponding to k=0, m is the mass of the electron; $F_j(k)$ is the backscattering amplitude from each of the N_j neighboring atoms of the jth type with Debye-Waller factor of σ_j (to account for thermal vibration (assuming harmonic vibration) and static disorder[5,8] (assuming Gaussian pair distribution) and at a distance r_j away). $\phi_j(k)$ is the total phase shift experienced by the photoelectron and it contains two contributions which are from the absorber and backscatterer, respectively:

$$\phi_{\alpha\beta}(k) = \phi_\alpha(k) + \phi_\beta(k) - \pi, \qquad (1.4)$$

where $\phi_\alpha = 2\delta$ is the phase shift of the absorber and ϕ_β is the phase of the backscattering amplitude.[6] The term $\exp(-2r_j/\lambda)$ is due to inelastic loses in the scattering process (due to neighboring atoms and the medium in-between) with λ being the electron mean free path.

Each shell of atoms scatters the emitted photoelectrons with a phase contribution of $2kr_j$. In the R-space Fourier transform of the k-space data, peaks appear at the distances from the absorber atom at which scattering occurs, shifted by the linear part of phase shift. The dominant contribution to the EXAFS comes from the contribution of the closest one or two shells, as the effects of higher shells are diminished due to damping by the Debye-Waller and scattering length factors. Thus, EXAFS is primarily a technique for measuring short range order in materials, especially the nearest neighbor distance.

The total phase shift $\phi(k)$, i.e. the value of equation (1.4), must be obtained independently before the near neighbor distance can be determined. The phase shift, as seen in (1.4), is specific to the atomic species of both absorber and backscatterer, but is not dependent on the chemical enviroment.[7,9,10] Thus a model compound consisting of the same atom pair in which the near neighbor distance is well known can be used to determine the phase shift.

Measuring Techniques

The EXAFS spectrum can be derived from a measurement of the photoabsorption coefficient over an appropriate range of X-ray photon energy. The direct approach to this involves measuring the normal incidence transmittance.[10] The absorption coefficient can also be inferred indirectly through measurement of some particular response of the sample to the absorption event. Such indirect schemes may involve detection of the photoemitted electrons, or of the fluorescent[11,12] X-rays or Auger electrons[13] emitted when the hole in the core of the excited atom is ultimately filled, or of ions which desorb from the surface of the sample in response to photoabsorption. These various techniques differ widely, not only in experimental configuration and detection technique, but also in their relative appropriateness for different types of systems. Some are especially suited to dilute systems, for example, whereas others are suited to studies of surface structure. In this chapter, the transmission mode which is the simplest and the most commonly used method for obtaining an EXAFS spectrum is described.

Transmission mode

The basic arrangement for a transmission EXAFS experiment is shown schematically in Fig. B-1. The monochromatic incident X-ray beam intensity is measured before (I_{in}) and after (I_1) the sample. Generally, it is found that

$$I_1 = I_{in}\exp(-\mu_t t), \qquad (1.5)$$

where μ_t is the total X-ray absorption coefficient and t is the sample thickness. For a uniform sample, the total absorption coefficient can be divided into the absorption of the atom of interest μ_a and that of the other atoms μ_b, such

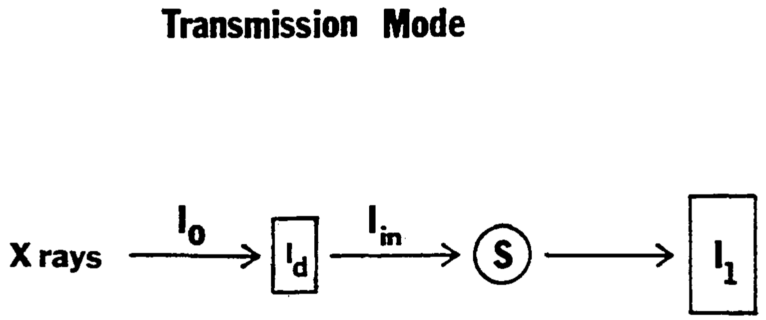

Fig. B-1. Schematic representation of the experimental arrangement for a transmission X-ray absorption experiment: I_o is the intensity of the primary beam; I_d is the amount of the beam detected (i.e. aborbed) by the first detector; $I_{in} = I_o - I_d$, which is the intensity of the beam actually radiates on the sample; I_1 is the beam detected by the second detector which is not transparent.

$$\mu_t = \mu_a + \mu_b. \tag{1.6}$$

Only μ_a is expected to have structure in the energy region being studied.

Signal-to-noise evaluation

According to (1.5), the total signal detected is the ratio I_d/I_1 (refer to Fig. B-1). The EXAFS signal (the modulations $\Delta\mu_a$ only) can be written as

$$S = \frac{\partial(I_d/I_1)}{\partial\mu_a}\,\Delta\mu_a = \Delta\mu_a t\left(\frac{I_d}{I_1}\right). \tag{1.7}$$

The noise is given by

$$N = \frac{I_d}{I_1}\left(\frac{1}{I_d} + \frac{1}{I_1}\right)^{1/2}, \tag{1.8}$$

with the resulting signal-to-noise ratio for a one second integration time being

$$\frac{S}{N} = \Delta\mu_a t\, I_o^{1/2}\left(\frac{1}{1 - e^{-(\mu_d t_d)}} + \frac{1}{e^{-(\mu t_t)} e^{-(\mu_d t_d)}}\right)^{-1/2} \tag{1.9}$$

In equation (1.9), μ_d and t_d are the absorption coefficient and thickness of the filling gas in the first detector (assuming it is a gas proportional counter or an ionization chamber).

The optimum condition for the achievement of large S/N ratio (>100 for EXAFS) can be obtained by maximizing the signal-to-noise ratio with respect to $\mu_d t_d$ and $\mu_t t_t$. We then obtain

$$\mu_d t_d = 0.245$$
$$\mu_t t_t = 2.55, \qquad (1.10)$$

which yields

$$S/N \simeq 0.566(\Delta\mu_a/\mu_t)I_o^{1/2} \qquad (1.11)$$

Under the condition that the ratio S/N >>1 for an EXAFS measurement, the concentration limit for the transmission experiment would be:

$$\mu_a/\mu_t > 10^{-3} \text{ when } I_o \sim 10^{11} \text{ cps,}$$

$$\mu_a/\mu_t > 10^{-1} \text{ when } I_o \sim 10^{7} \text{ cps.}$$

EXAFS Data Analysis

There are various approaches to the analysis of EXAFS data. In general, the steps which are typically involved are: (a) removal of background absorption, (b) extraction of the EXAFS χ, (c) Fourier transform into r space, (d) extraction of structural information in r space, and (f) extraction of structural information in k space. The rigor required at each step in the analysis depends somewhat on the means by which the structural information will ultimately be extracted. Specifically, will it be deduced through comparisons among experimental EXAFS data sets, or through comparisons with calculated spectra? In the former case, it is essential that all the data set be reduced according to the same detailed prescription. On the other hand, comparison with a calculated spectrum demands that each data analysis step be precise on an absolute scale. The procedure for structural determination from EXAFS can be summarized in a flow chart which is shown in Fig. B-2.

In the data analysis, the Fourier transform (FT) and the curving fitting (CF) techniques are the two major approaches. The FT method[1,6,14] involves the Fourier transformation of $k^n\chi(k)$ in momentum (k) space over the finite k range k_{min} to k_{max} to give the radial distribution function $\rho(r')$ in distance space, where

$$\rho(r') = 2\pi^{-1/2}\int k^n\chi(k)\exp(i2kr')dk. \qquad (1.14)$$

Each peak in $\rho(r')$ is shifted from the true distance r by $\alpha = r - r'$ where α amounts to ca 0.2 ~ 0.5 Å depending upon the elements involved[15,16] (the value of α can be obtained from model compounds). For closely related systems,[17] the approximate number of neighboring atoms can be calculated by $N = N_s(Ar^2/A_s r_s^2)$ where N_s, A_s, r_s and N, A, r are the number of atoms, the Fourier transform peak areas, and the interatomic distances in the standard and the unknown compounds, respectively.

The CF technique[8,16], on the other hand, attempts to best fit (via least-squares refinements) the $k^n\chi(k)$ spectra in k

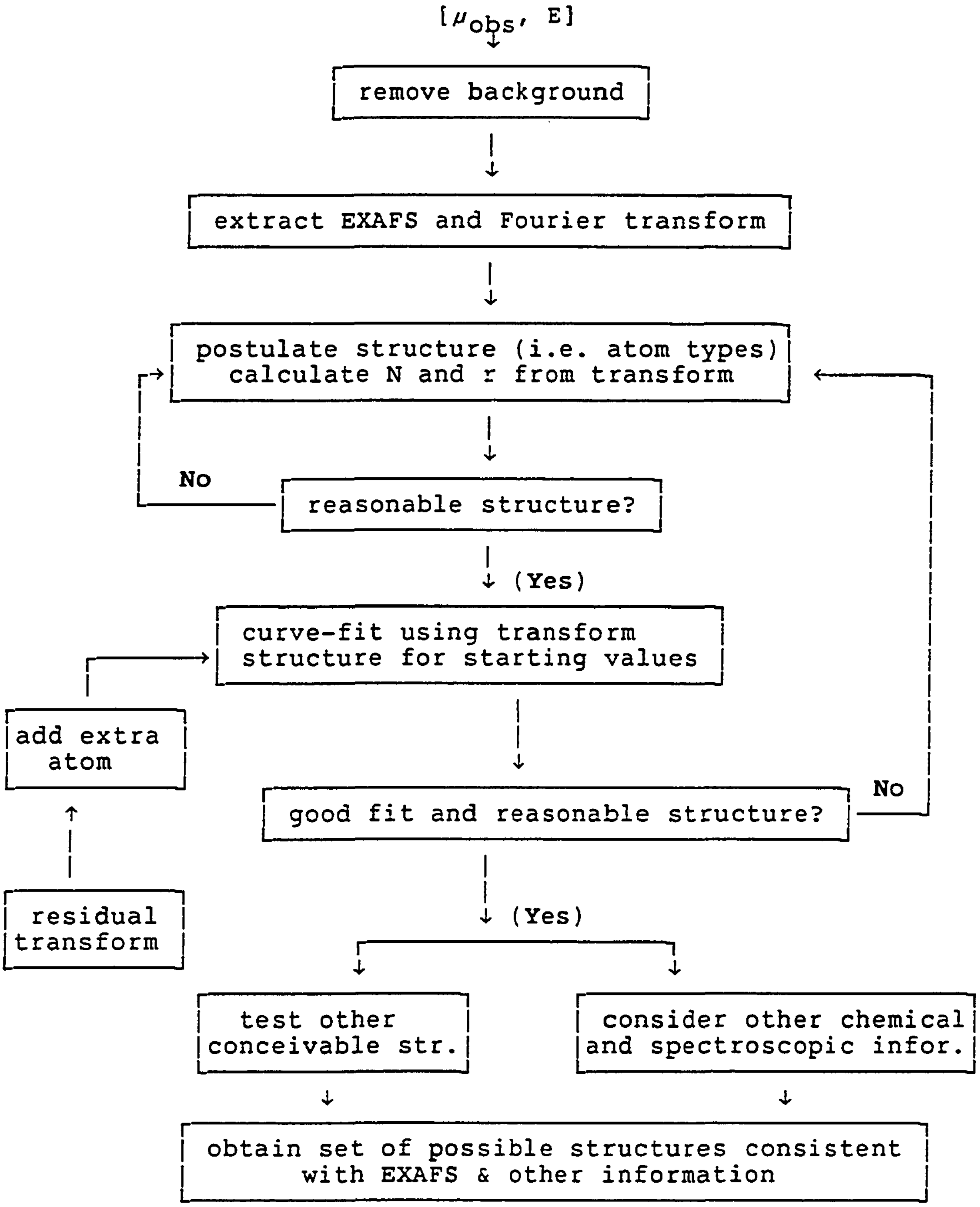

Fig. B-2. A flow diagram for the EXAFS data analysis space with some phenomenological model based on equation (1.2). The EXAFS function $\chi(k)$ is usually divided into two parts: the amplitude function and phase function.[4] These two functions are generally parameterized into simple analytical forms. From the fitting results of the amplitude function, the information of N, F, σ, and λ can usually be obtained. From the fitting results of the phase function, one can obtain refined values for ϕ and r. (Note theoretical values[18] of F and ϕ are also available and can be used in the CF method.)

CHAPTER 2. EXPERIMENTATION

Introduction

The EXAFS signal typically contributes only a few percent to the total absorption and must be measured with a signal-to-noise ratio S/N greater than 100 in order to determine the structure accurately. Since S/N is proportional to the square root of the X-ray intensity (see equation (1.9)), the X-ray source must be very intense. In addition, since the oscillations in $\mu(E)$ in the region of interest for EXAFS have periods usually on the order of ~25 eV, an experimental X-ray energy resolution of at least ~15 eV is required to obtain useful EXAFS measurements. Thus, in general, the experimental requisites of an in-lab EXAFS facility are: (1) high X-ray fluxes, (2) high energy resolution, (3) the capability of energy discrimination (to eliminate harmonics) and the control of radiation purity (to suppress strong characteristic lines) and (5) broad energy range.

The X-ray source is the major problem in in-lab EXAFS. The problem is caused by the fact that not only is intensity wanted but also the suppression of harmonics which may be diffracted by the spectrometer monochromator. The harmonics problem usually necessitates the capability of energy discrimination in the electronic detector system which further complicates the in-lab EXAFS system.

In the following sections, each of the four essential components of an in-lab EXAFS facility is discussed with regard to the above requisites.

X-ray Sources

In general, there are two different sources of continuous X radiation available for EXAFS experiments: bremstrahlung from a conventional X-ray source (CS) and synchrotron radiation (SR). As concerns a typical EXAFS experiment, the most relevant differences between these two sources are intensity, polarization, and purity. Their spectral characteristics are shown in Fig. B-3.

The intensity of the continuous radiation from a conventional X-ray source is usually less than that from SR in the order of $10^4 \sim 10^6$ photon/second. To achieve high photon flux for the in-lab EXAFS experiments, the more powerful rotating anode X-ray sources are generally used to provide as much intensity as possible. Since the efficiency of X-ray generation is proportional to the atomic number of the target and the operating voltage of the tube, it is desirable to use a high Z anode and operate at high voltage to get higher photon flux. However, higher tube voltage also means higher photon energy and this certainly would cause a harmonics problem in EXAFS measurements. Unless a convenient method of eliminating them in the data collection system is devised, one

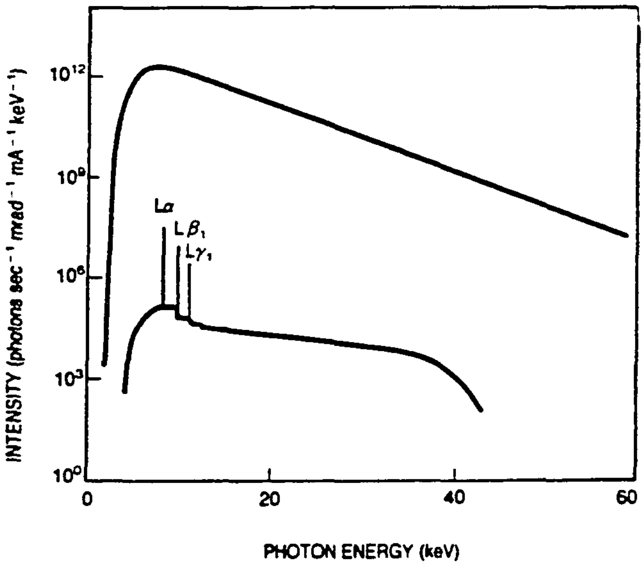

Fig. B-3 Comparison of spectra. The top curve represents the spectrum available from a typical synchrotron radiation source. The lower curve represents the spectrum from a typical tungsten-target X-ray tube.

must avoid generating them in the first place. This can best be achieved by limiting the maximum operating voltage of the tube to the 10 - 20 KV region while keeping the tube current as high as possible.

The radiation obtained from the CS is only partially polarized. As as a consequence, EXAFS information as a function of direction in an oriented sample[19] cannot be obtained in the in-lab EXAFS measurements.

X-rays obtained from the conventional source are not a smooth function of energy. The spectrum contains many sharp characteristic lines. These lines are typically three orders of magnitude more intense than that of bremstrahlung and can usually severely distort the EXAFS spectrum.[20] To avoid running into this problem, automatic control of tube current to lower the beam intensity when scanning through a characteristic line may be one of the best techniques.[21]

Focusing Geometries

The EXAFS spectrometers using a conventional X-ray source can only be made to produce either high flux or high resolution, but cannot easily provide both simultaneously.[3] The two basic geometrical arangements for EXAFS experiments are shown in Fig. B-4: a single crystal spectrometer with Rowland circle focusing geometry and a double crystal spectrometer.

Single crystal spectrometer

This spectrometer (see Fig. B-4a) employs a Johann- or Johansson-type of monochromator[19,22] and it provides a high-flux mode for in-lab EXAFS measurements. The bent crystal monochromatizes the beam and focuses it to a line at a position near the sample. To achieve maximum focusing, the crystal surface should remain on the Rowland circle while it is rotated to scan energy. The focusing condition requires also that the source-to-crystal and crystal-to-sample distances be equal at any given scan energy and obey the relationship

$$D = 2R\sin\theta(E), \qquad (2.1)$$

where D is the source-to-crystal distance, R is the radius of the Rowland circle, and $\theta(E)$ is the Bragg angle for radiation of energy E.

The efficiency of the bent crystal increases linearly with the subtended angle of the primary beam and thus inversely proportional to R. This suggests that the focusing circle should be as small as possible. However, the energy resolution of a bent-crystal monochromator also decreases with R. Thus, the R value must be chosen to represent a compromise (usually ~50 cm) between the efficiency and resolution of the spectrometer.

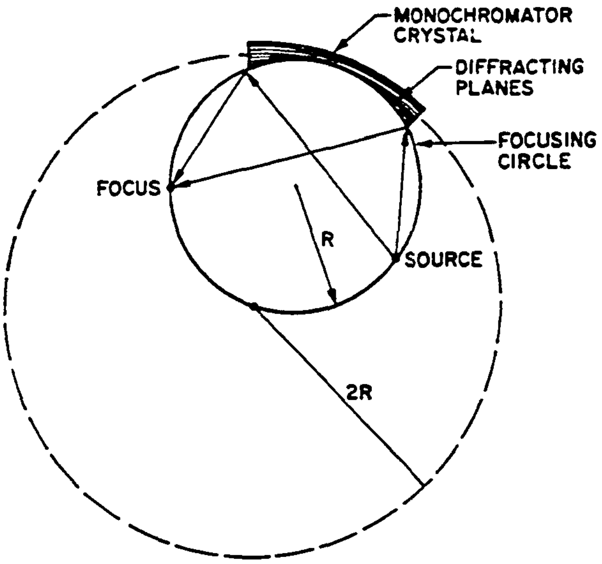

(a) Single crystal spectrometer system

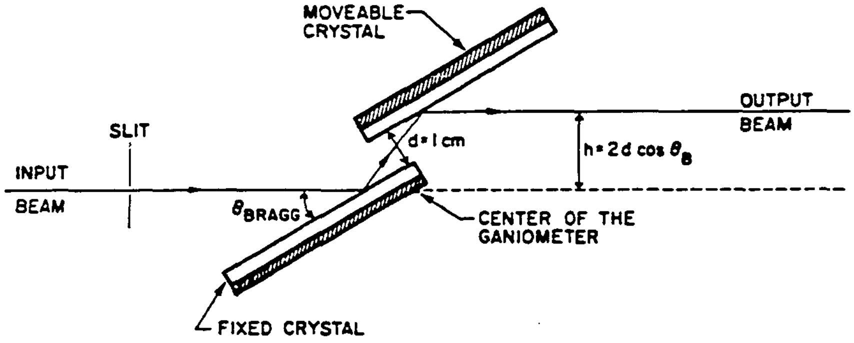

(b) Double crystal spectrometer system

Fig. B-4 Two focusing geometries for the EXAFS spectrometer

Double crystal spectrometer

This spectrometer (see Fig. B-4b) employs two flat-crystals to monochromatize the beam. It provides the high-resolution mode for the in-lab EXAFS measurements. It is usually used to investigate the edge region of the absorption spectrum which needs 1 - 2 eV of resolution. The resolution of this double-crystal monochromator system depends on the angle $\Delta\theta$ made by the divergence slit on the X-ray port of the source, the take-off angle and the distance of the source from the slit. The smaller the slit width, the lower the take-off angle, and the larger the distance, the better is resolution. The resolution also improves when crystals with smaller interplanar spacings are used.

In addition to increased energy resolution over a single-crystal spectrometer, this double-crystal arrangement offers an added advantage that the monochromated output beam is parallel to the input beam but displaced from it by only an amount

$$h = 2L\cos\theta(E), \qquad (2.2)$$

where $\theta(E)$ is the Bragg angle and L is the spacing between the crystal faces of the monochromator. The distance h changes by Δh during a scan, but in practice Δh is negligible over a ~1500 eV scan range.[23]

Monochromators

The monochromator plays a key role in the EXAFS spectrometer. Properly bent crystals can be used to provide maximum focuing and obtain high photon fluxes. Five common considerations for the monchromators are: (a) brightness, (b) energy resolution, (c) energy range, and (d) higher-order reflection. The brightness of the crystal is a function of energy and is associated with the absorption coefficient, structure factor and unit cell volume of the crystal. Ge crystals are generally about two times brighter than Si and thus better for use in EXAFS measurements.

The energy resolution of a bent-crystal may be expressed in the relation[24]

$$\Delta E \sim \frac{E^3(2d)^2}{8RC^2}[(W_a+W_s)^2+(\frac{2LnCE^2}{Kd})^2+(\frac{h^2}{8R})^2]^{1/2}, \qquad (2.3)$$

where d is the crystal interplanar distance, R is the Rowland circle radius, L is the source-to-crystal distance, C = 12396 eV.Å, W_a is the projected width of the anode image, W_s is the width of the receiving slit, and h is the beam's vertical divergence. This equation indicates that ΔE roughly depends on $(2d)^2$, so by using high index-plane crystals adequate resolution may always be achieved.

Because of the mechanical limitation in the Bragg angles, a broad energy range can only be achieved by employing a series of crystals with different interplanar spacings; each crystal covers a different energy range. The harmonics problem, as mentioned in the previous section, may also be eliminated by the use of crystals with planes of all odd indices if no appropriate means is made in the source or in the detector system. For example, the first harmonic is absent for the crystal Si(111) or Si(311) because the structure factor of the first harmonic is zero. Using one of these types of crystals may be the best way to avoid harmonics if one can find appropriate ones.

Detector Systems

The standard X-ray detectors are photographic films, gas ionization detectors, and solid-state detectors.[25] Film is only used for energy dispersive spectra. Two types of gas ionization detectors are commonly used in EXAFS experiments: the ionization chamber and the proportional counter. Both consist of an inert gas between two electrodes. Electron-ion pairs are produced when an X-ray photon is absorbed. The efficiency of these detectors are dependent on the filling gas used for photons with energy E. Ionization chambers are current detectors without multiplication. They have the current stability required for EXAFS measurements and their linearity are not limited by dead time considerations. Their limitations are no energy discrimination and a minimum useful counting rate due to amplifier noise. For photons with energy E, the minimum counting rate for attaining statistical noise can be estimated by the equation

$$N_g = 1.4\text{x}10^3\text{x}(10/E)^2/\text{sec}, \qquad (2.3)$$

where E is in KeV. Thus, the useful intensity range for the ionization chamber is $I > N_g$.

The proportional counters are pulse detectors which have an inherent interdependence of their linearity with the counting rate. Since the current pulse produced is proportional to the energy of the X-ray photon absorbed, they can be used to discriminate among various photon energies. Its energy resolution is ~1300 eV for 10 KeV X rays.

Two types of solid-state detectors are commonly used: scintillation counters and semiconductor detectors. Both are pulse detectors. In a scintillation detector, pulses of visible light are produced by the fluorescence resulting from the absorption of X rays in the scintillating material. The visible radiation is detected with a photomultiplier tube. The detector has high gain and relatively poor energy resolution. For instance, for standard NaI(Tl) scintillation detectors, energy resolution is ~3500 eV at a 10 KeV photon energy.

Semiconductor detectors are Si or Ge crystals compensated with Li. They have an intrinsic gain of unity and good energy resolution (~200 eV at 10 KeV photon energy). Because of high noise level, these detectors are necessarily operated at liquid nitrogen temperature. The characteristics of all the detectors mentioned above are summarized in Table B-1.

In general, the ideal detectors for in-lab EXAFS measurements should have the following characteristics: (a) high linearity, (b) high efficiency over a wide energy range, (c) high counting rate, and (d) good energy discrimination. Nonetheless, the above requirements may be relaxed if harmonics and characteristic line problems are already taken care by some other means. For example, working with continuous radiation from a powerful rotating anode X-ray generator which operates at a high-current and low-voltage mode, the ionization chamber is perhaps the best choice for they can respond linearly to the high photon-flux. They are also highly linear over a dynamics range of 100 to 1, thus the distortion of the EXAFS spectrum owing to the presence of characteristic lines can be significantly reduced.[26] On the other hand, if there are harmonics problems, the proportional counter or the scintillation counter must be used along with some appropriate pulse shaping and analyzer electronics to provide energy discrimination. In this case, counting loss due to dead time of the counters must be corrected or avoided.

Table B-1. Characteristics of various detectors for in-lab EXAFS facilities

Detector	Dead time (sec)	Intensity range (cps)	$\Delta E/E$ at 10 KeV	Energy range	Remarks
ionization chamber	none	no upper limit			no E discrimi. lower limit in I
Propor. counter	10^{-7}	$0\text{-}4\times10^{6}$	~13%	1-30KeV	variable efficiency
Scintil. counter	10^{-6}	$0\text{-}1\times10^{6}$	~35%	2-30KeV	large area
Semicon. detector	10^{-6}	$0\text{-}4\times10^{5}$	~3%	2-30KeV	small area low T operation

CHAPTER 3. RESULTS AND DISCUSSIONS

Introduction

The construction and development of the in-lab EXAFS facility are described in this chapter. This facility employs an X-ray source from an Elliot GX21 rotating anode generator and a commercially designed Johann-type spectrometer, EXAF-3.[24] This GX21 system had been specially designed to suit the need for low-voltage (10-20 KV) high-current (~300 mA) operations. Although the operating voltage is very low, 20 times of useful X-ray flux obtained from sealed tube system[24,27] can be achieved. It has been reported that successful EXAFS spectra can be obtained in 20 minutes working at such conditions.[28,29]

The spectrometer has a Rowland circle radius of 20 cm and its mechanical system had been designed to meet simultaneously the three criteria of (1) equal source-to-crystal and crystal-to-sample distances, (2) variation of source-to-crystal distance with variation in θ, and (3) synchronized θ rotation of the crystal and 2θ rotation of the sample plus detectors. The spectrometer is also equipped with stainless steel beam lines to allow operation in helium atmosphere. Two detectors are employed: a gas-flow proportional counter (as the I_0 detector) using P-10 gas, and a NaI(Tl) scintillation counter (as the I_1 detector). A schematic representation of this

EXAF-3 spectrometer along with the beam path is depicted in Fig. B-5a.

Spectrometer Alignment

The alignment of this EXAF-3 spectrometer is divided into two levels. The first level is the alignment of the X-ray tube take-off angle and this is called a preliminary alignment. Once performed it needs never be repeated or readjusted over the entire angular range of the spectrometer ($40° \leq 2\theta \leq 140°$). The procedure for an appropriate preliminary alignment is done as follows:

(1) Position the pivot A (make it as accurate as possible) under the anode (refer to Fig. B-5a) and slide the monochromator trajectory to the position at a precalculated angle of 6° (see Fig. B-5b).

(2) Replace the monochromator housing with a slit (S1) and also put another slit (S2) at the end of the trajectory. By the aid of a laser beam, put the three points, pivot A (or the center of the X-ray window), S1 and S2, in the same line by rotating the slit S1.

(3) Place the scintillation counter at the end of the trajectory and turn on X-ray beam (keep GX21 power at or below 10 KV x 10mA). Slightly rotate S1 until maximum counts is registered in the counter (by watching the counting rate shown on the digital counter display).

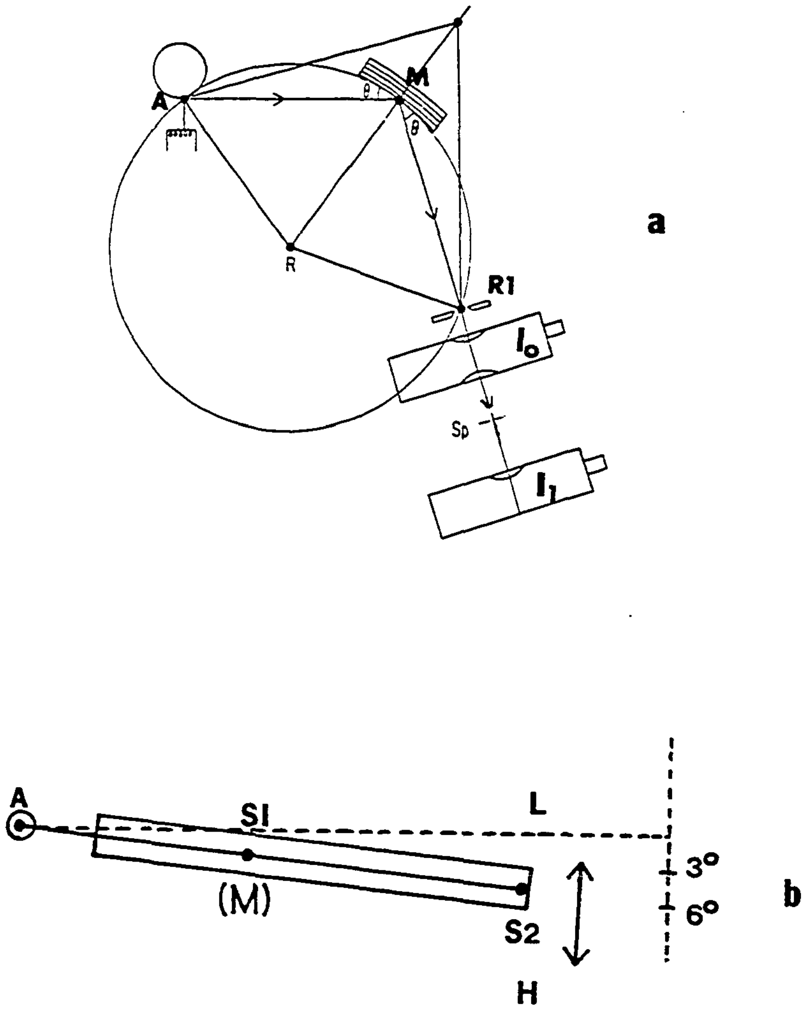

Fig. B-5 A schematic representation of the EXAF-3 spectrometer: (a) The spectrometer, (b) The monochromator trajectory. The dashed line represents zero-degree setting.

Then lock S1 on the Oreil stage.

(4) Slide the trajectory toward the high take-off angle side (direction H) until the X-ray intensity falls to about half maximum.

(5) Slide the trajectory slightly toward the low angle side (direction L) and record the beam intensity at each prespecified angle until the intensity falls off to below half maximum.

(6) Determine the take-off angle from the recorded data and slide the trajectory to that angle. Repeat (4)-(6) until a fixed value of the angle is obtained.

(7) Set the trajectory at the desired angle and lock it.

The second level involves bending the crystal and aligning the monochromator. This alignment is not permanent. It should be redone after changing the GX21 filament, repositioning the anode, or even changing the energy range of detection (the procedure of bending crystal may be omitted if it had been bent and fixed on a permanent bending jig or unless its radius has changed). The procedures are described in the following:

(1) Fix a desired crystal on a bending jig (using screws C and D, refer to Fig. B-6a) and bend it approximately[30] to a radius of 40 cm by the use of screws A and B.

(2) Move the metal flag (which is on the bending fixture) all the way back by turning the screw E (refer to Fig. B-6b) on the backside of the bending fixture, unloosen screw F,

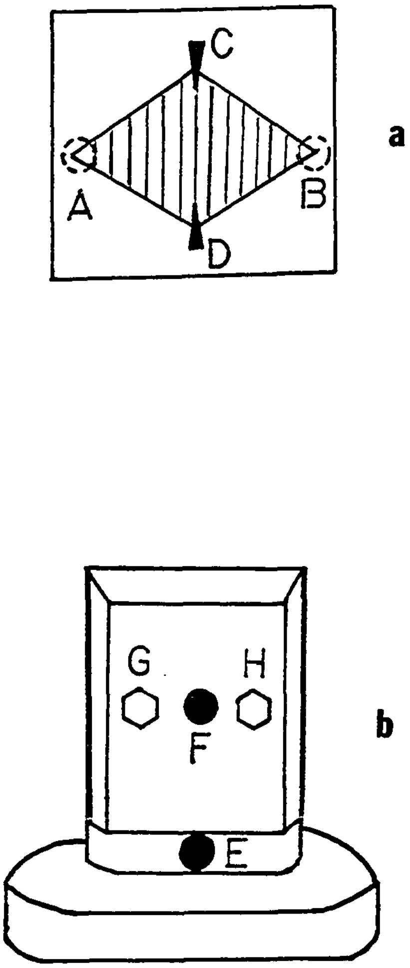

Fig. B-6 Components in the monochromator housing: (a) Bending jig, (b) Bending fixture.

put on the bending jig with crystal on and screw F to make it tight. Move flag close to the crystal surface (~2mm from the surface).

(3) With the X-ray beam on, rotate the crystal until maximum intensity is detected.

(4) Adjust the bending radius slightly through screws G or H (see Fig. B-6b) no more than ±1/8 turn (take the direction that gives the higher intensity) until the maximum intensity is obtained.

(5) Repeat (3) and (4) until no more adjustments are needed to obtain a global maximum intensity.

(6) Move the metal flag away from the crystal until a maximum intensity is obtained.

(7) Drive the Oreil stage (with the crystal) away from the source as far as possible. Adjust the angular setting of the crystal until a maximum flux has been detected through the receiving slit (R1) (refer to Fig. B-5a).

(8) Drive the Oreil stage toward the source as close as possible and adjust the position of pivot A until a maximum flux has been detected.

(9) Repeat (7) and (8) until the beam intensity detected on both sides maintain at their maxima.

Step (7) is essential to orient the crystal so that it can achieve maximum focusing. Step (8) is used to "tune" the position of pivot A in order to keep the source, crystal

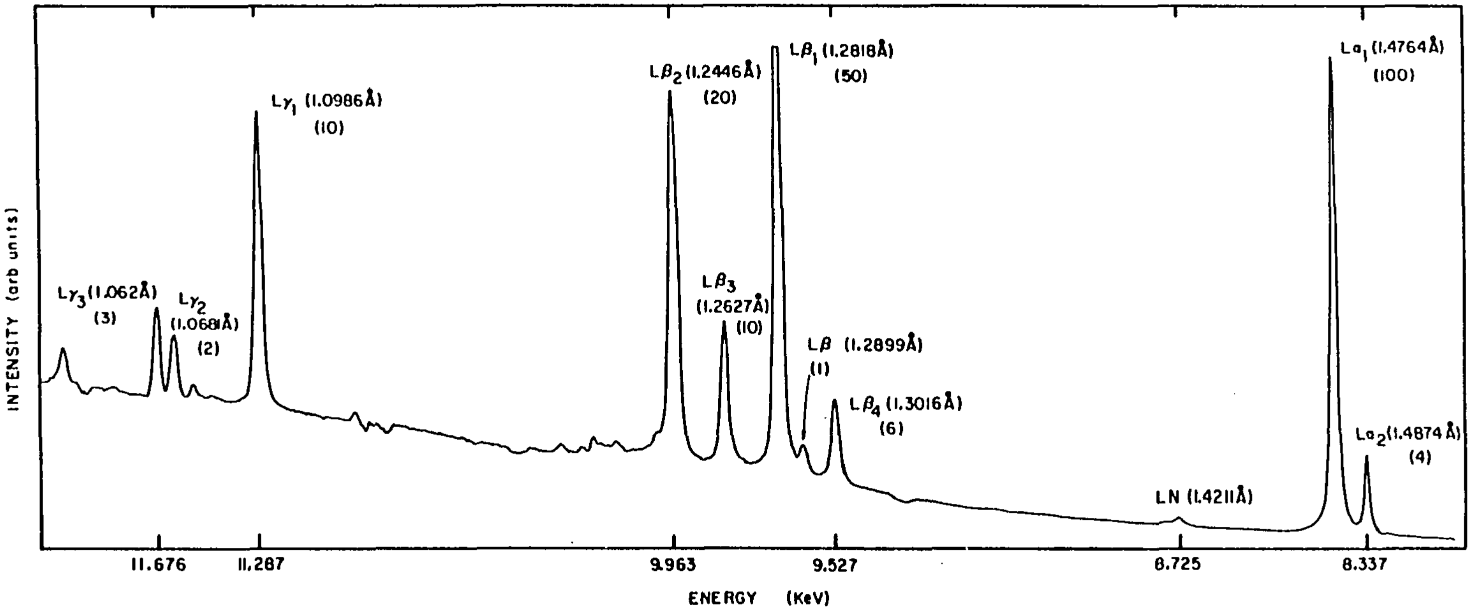

Fig. B-7 Partial X-ray spectrum of the tungsten anode measured from a Si(400) crystal. The number under the wavelengths are the relative intensities of the characteristic lines.

surface, and receiving slit precisely and simultaneously on the Rowland circle. If the alignment described above is done properly, all the significant characteristic lines in the X-ray spectrum of the tungsten anode in the energy range of 8.0 - 12.0 KeV could be measured explicitly, as shown in Fig. B-7, using a Si(400) crystal.

Automation

The hardware and software that have been developed to perform real-time control of the EXAF-3 EXAFS spectrometer and the detector electronics are described in this section.

Computer hardware

The current computer hardware includes a central microcomputer which is a LSI-11/03 with 8K bytes of memory. The computer is hooked to an Ames Laboratory designed interface through which it can control the EXAF-3 spectrometer. Three DLV-11 Serial Interface units are also hooked to the LSI-11/03 computer. One is connected to a VAX11/730 computer (this computer is used to control the total system) utilizing a 1200 baud rate transmission. Another one is connected to a teletype with a 300 baud rate and the third one is connected to an ORTEC interface controller through which it can control an ORTEC dual-channel photon counter. A block diagram of the hardware involved is shown in Fig. B-8.

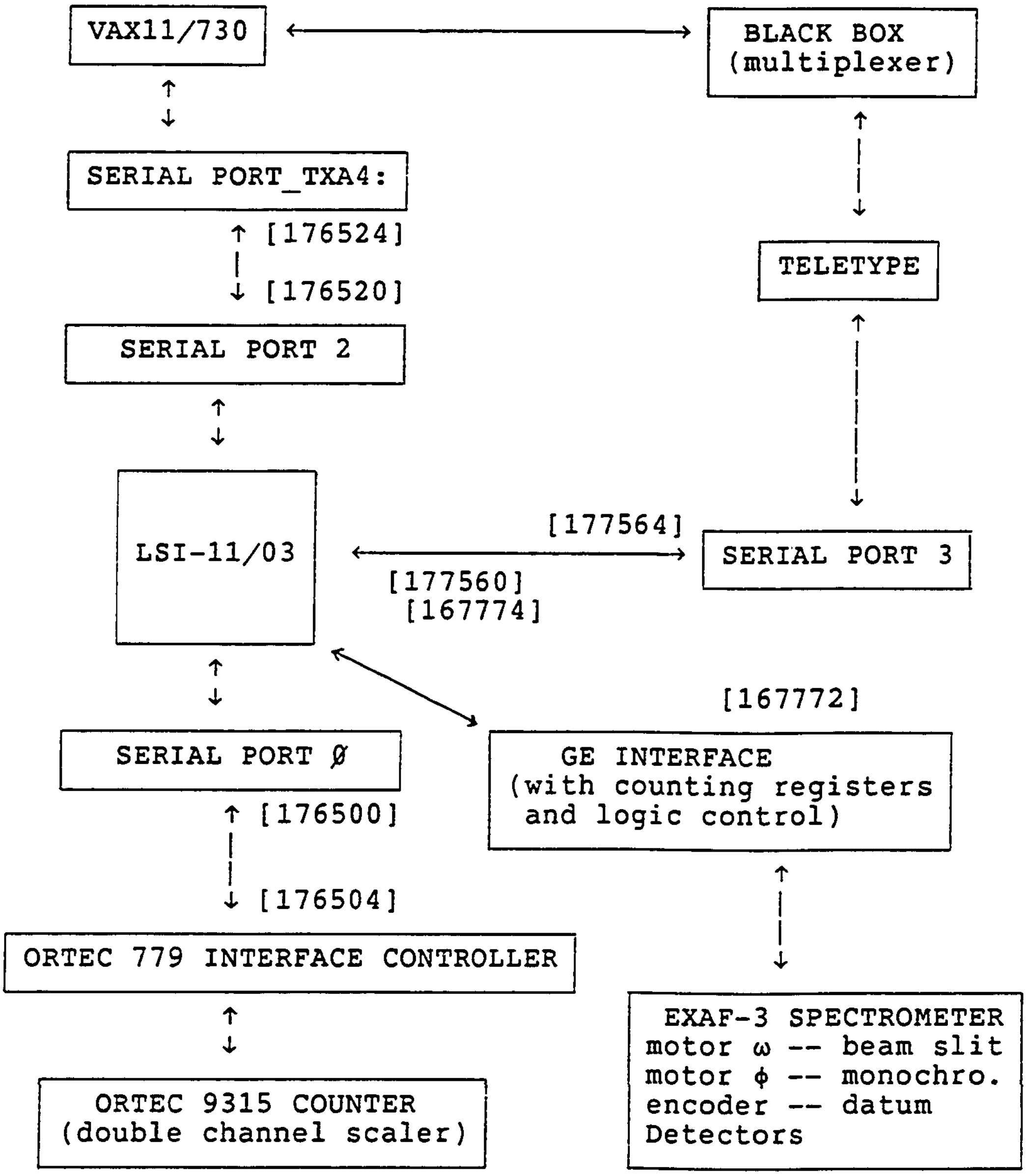

Fig. B-8. Schematic diagram computer hardware system. The communication line numbers are in [].

Computer software

The software for the real time control of the spectrometer (or the monochromator, essentially), the beam slit[31] and the counting electronics have been developed. Since the LSI computer has no compiler, this software was written on LSI using PDP-11 machine language.

Both the monochromating crystal and the beam slit are driven by a stepping motor. These motors are operated in a single-step manner[32] so that their speeds are slow and constant. Backlash is taken care of by overshooting 50 motor steps whenever the motor moves away from the source (i.e., from low angle to high angle). Thus, the motor is always driven in the same direction when it approaches the destination.

The controlling of the external ORTEC dual A/B counter can be achieved by two means. In preset-count counting, the dual counter must be set on a "Master" mode. When the LSI computer issues a command to the ORTEC interface controller, it in turn informs the counter to start to count. The counter continues counting until the B counter reaches a preset number (which was manually set on the counter panel) and then acknowledges the interface controller with the number of counts executed in both A and B counters. In preset-time counting, the counter must be set on a "Slave" mode and the control of the counter is then transferred to the GE interface. The LSI computer first issues a command to the

Table B-2. EXAFS spectrometer's I/O commands

I/O Command	Function	Location
1	Send current ϕ shaft (beam slit) position	6650-6670
2	Set ϕ shaft position	6750-6770
8	Move ω shaft (monochromator) from current posn. to a given final posn.	1776-2236
16	Check datum	4500-4616
64	Preset-time counting (time is controlled by the real time clock)	3200-3430
128	Send current ω shaft position	6600-6620
256	Set ω shaft position	6700-6720
512	Preset-count counting	10000-10204
1024	Move ϕ shaft	3500-3654

interface to set up the 8th bit in the status word at location 167772 to start counting. Time is monitored by a real-time clock with a 1/60 second of resolution. When the time is up, the LSI computer sends out a "print" command directly to the ORTEC interface controller so that the number of photons counted in both A and B counters can be retrieved.

All types of commands which operate on the LSI computer and locations of these programs are listed in Table B-2.

Detector Linearity Tests

For accurate measurement of X-ray intensities, it is essential to be working in the linear range of the counting system; if not, at least one must be able to correct accurately for counting losses. The capability of a detection system to respond linearly to the signal is dependent on the intrinsic properties of both the detector and its associated electronics. Thus, the overall dead time of a detection system is the sum of the detector dead time and electronic circuitry dead time.

Since the electronic circuitry dead time of the proportional counting channel (see Fig. B-9) was estimated at about 1 μs, which is longer than the dead time of the proportional counter itself (refer to Table B-1), a counting rate $2.0\text{x}10^5$ is considered as an upper limit of this detection system's linear range. For the scintillation counting channel

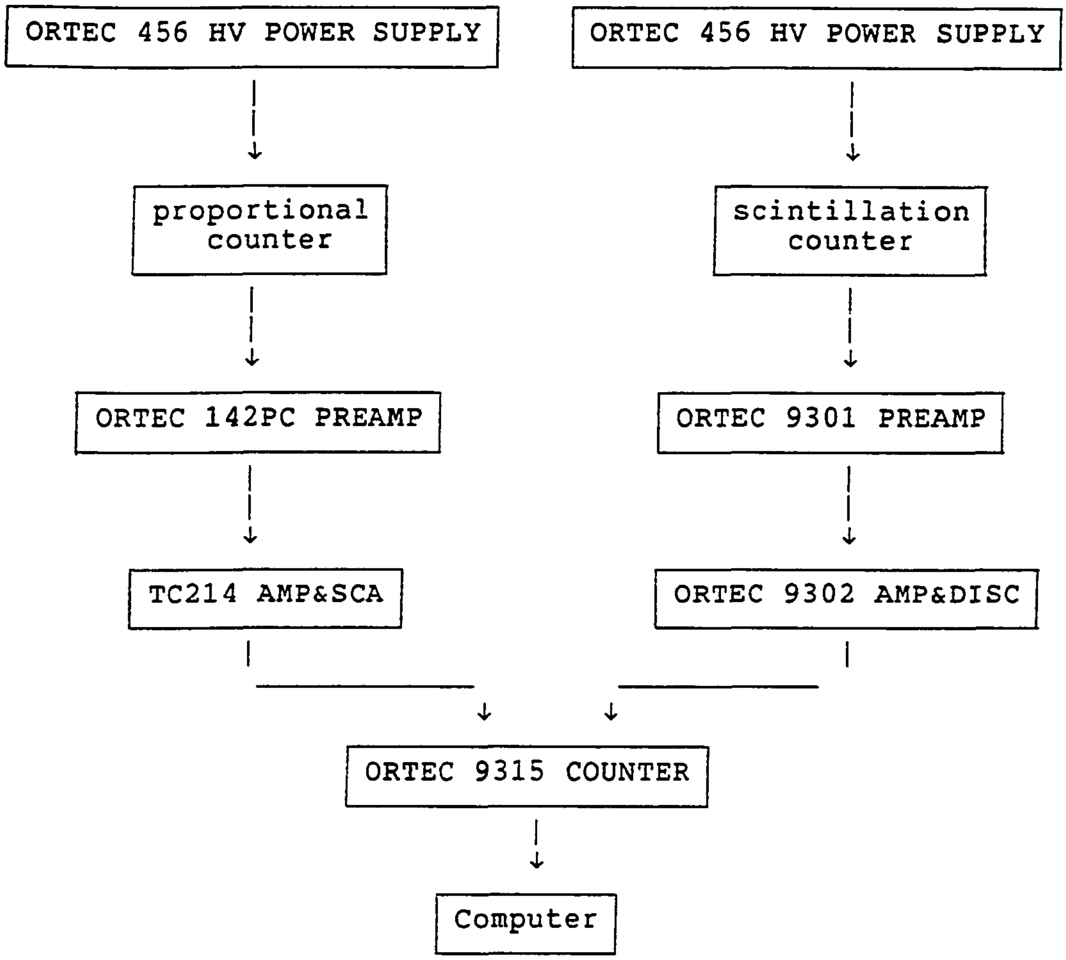

Fig. B-9 Schematic diagram detection system without the use of a single channel analyzer (also see Fig. B-9) the electronic circuitry dead time is estimated at much less than 1 μs. Thus the upper limit of the linear range could not be defined by this electronic dead time information.

Measurements of the linear ranges for both the proportional and scintillation counting channels have been performed using two methods, the multiple-foil method[33] and absorption factor method.[34] Principles of these methods along with experimental results are described in the following sections.

Multiple foil method

The procedure consists, basically, of interposing a steadily increasing number of identical foils in a monochromatic X-ray beam so that the observed counting rate is steadily decreased. A plot of the number of foils interposed vs. the logarithm of the counting rate should be a straight line over the region for which the detector has a linear response. The slope of the line is $-\mu t$, where μ is the mass absorption coefficient and t is the thickness of the foil.

In this experiment, four different kinds of foils were used: nickel, vanadic oxide, iron oxide and aluminum. The first three are standard X-ray filter materials. The aluminum foil with various thickness was made of ordinary kitchen aluminum sheets.

Proportional channel This counter was tested under the following conditions: (a) detector operating voltage at 1000 volts, (b) filling gas (P-10) pressure at 1 Psi and (c) photon energy at 8 KeV from a Si(400) monochromating crystal. Observed counting rate and their logarithms for each of the foils used are listed in Table B-3a. The corresponding plots (# foils vs. $\ln I_n$) are shown in Fig. B-10.

The slopes of the calibration lines in Fig. B-10 were all calculated by a least-squares fit.[35] The calibration curves and estimated linear ranges are listed in Table B-3b. It can be seen that for vanadic oxide, all the counting rates in the test were so small that no upper limit of the linear range could be drawn from the result. However, it did show that a counting rate of 4×10^4 is still within the linear range of the proportional counting channel.

The data from iron oxide suggested that a counting rate of 1.36×10^5 had exceeded the linear range and the aluminum foil data indicated that the counting rate of 1.0×10^5 might still be in the linear range. Combining these results, we conclude that the upper limit of the linear range for the proportional counting channel is about 10^5 cps which is consistent with the 1 μs dead time of the electronics.

Scintillation channel This channel was tested under the condition of (a) detector operating voltage at 1600 volts and (b) an X-ray energy at 8 KeV from a Si(400) monochromating crystal. The results are listed in Table B-4a and Fig. B-11.

Table B-3. The results of multiple-foil method for proportional counting channel

(a) observed counting rate and their logarithm values

#	vanadic oxide		iron oxide		Al foil	
	I_n[a]	$\ln I_n$	I_n	$\ln I_n$	I_n	$\ln I_n$
0	41694	10.638	180832	12.105	232508	12.357
1	20813	9.943	136513	11.824	101015	11.523
2	10080	9.218	74680	11.221	32541	10.390
3	4695	8.454	29647	10.297	9269	9.134
4	1981	7.591	9066	9.112	2807	7.940
5	1003	6.911	3240	8.083	1024	6.931
6			945[b]	6.851	406	6.006
7			119[b]	4.779	123	4.812

[a] I_n is a net intensity obtained by subtracting both background and electronic noise from observed intensity.

[b] These data were not used in the calculation of the slope.

(b) estimated linear ranges

type of foil	linear range	calibration curve
vanadic oxide	$>4\times10^4$ cps	$\ln I_n = 10.738 - 0.7715*n$
iron oxide	$\leq1.3\times10^5$ cps	$\ln I_n = 13.668 - 1.1305*n$
aluminum foil	$\geq1.0\times10^5$ cps	$\ln I_n = 12.458 - 1.0938*n$

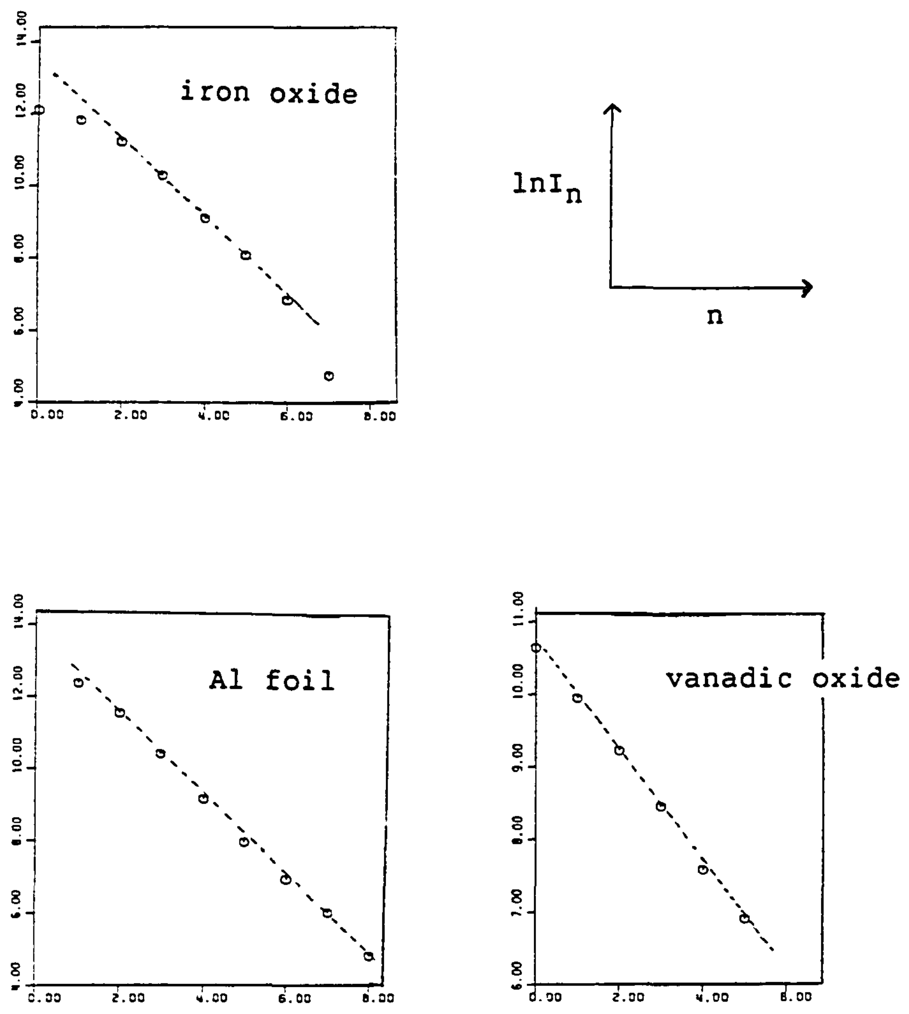

Fig. B-10 Multiple foil method: The number of foils (n) vs. the logarithm of the counting rate ($\ln I_n$) (proportional counter). See text for detail

Table B-4. The results of multiple-foil method for scintillation counting channel

(a) observed counting rates and their logarithms

#	vanadic oxide		Ni foil		Al foil	
foil	I_n	$\ln I_n$	I_n	$\ln I_n$	I_n	ln_n
0	172542	12.058	2361954	14.675	1764769	14.384
1	85830	11.360	931918	13.745	1063300	13.877
2	29486	10.290	99708	11.51	429636	12.971
3	14221	9.559	8604	9.06	227865	12.337
4	8542	9.047	2018	7.61	156143	11.959
5	4387	8.375	854	6.75	96345(n=6)	11.476
6	2503	7.805	572	6.35	66002(n=8)	11.097
7	1209	7.055			46408(n=10)	10.745
					30942(n=12)	10.340
					21410(n=14)	9.972
					14953(n=16)	9.613
					10697(n=18)	9.278
					7786(n=20)	8.960
					4920(n=22)	8.501
					3740(n=24)	8.227
					2680(n=26)	7.894
					1829(n=28)	7.512

(b) Estimated linear ranges

type of foil	linear range	calibration curve
vanadic oxide	$>10^5$ cps	$\ln I_n = 11.531 - 0.63169*n$
aluminum foil	$>2.5\mathrm{x}10^5$ cps	$\ln I_n = 12.498 - 0.17849*n$
nickel foil	$>2.5\mathrm{x}10^5$ cps	$\ln I_n = 12.427 - 1.1550*n$

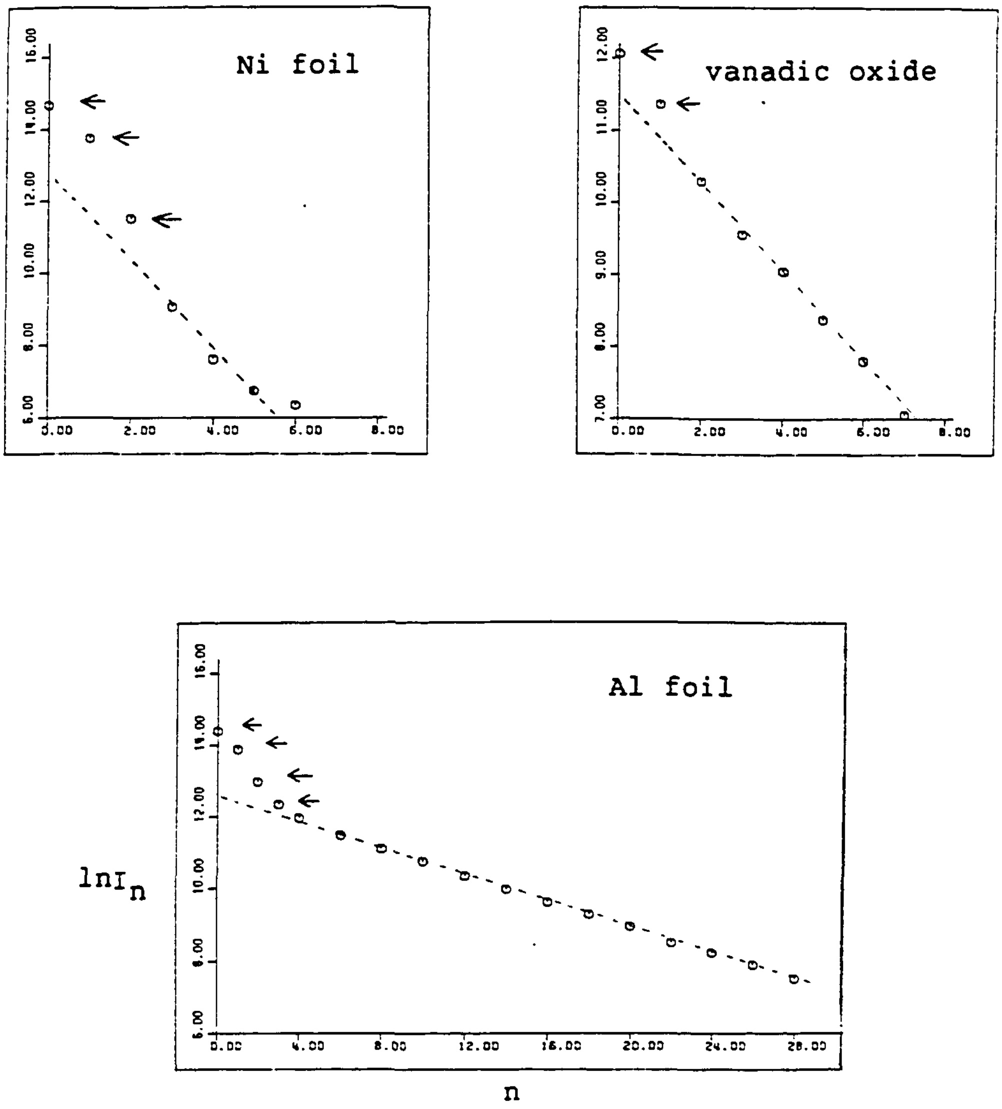

Fig. B-11 Multiple foil method: The number of foils (n) vs. the logarithm of the counting rate ($\ln I_n$) (scintillation counter). See text for detail

By examining these plots, we found that all of them behaved abnormally at high counting rates (see those marked by an arrow sign in Fig. B-11). No explanation has been advanced for this strange behavior of the scintillation detector as yet.

By ignoring the data of high counting rate, the linear range could be found for each foil and these are shown in Table B-4b. The results indicate that the scintillation counting channel could respond linearly to at least 2.5×10^5 cps.

Absorption factor method

In this method, only one piece of foil is required. The apparent absorption factor of a suitable metal foil of uniform thickness is measured at various counting rates by measuring the beam intensity with and without the foil in place. A plot of this factor vs. the observed counting rate, preferably on a logarithmic scale, for the direct beam should give a straight line if the detector is responding linearly. A rapid change in the absorption factor occurs as the detector becomes increasing nonlinear. Some relevant mathematics are briefly described here.

At all counting rate, one can write, assuming the sample thickness is unity, that

$$I_o = I_{o,d} e^{-\mu_o} \qquad (3.1)$$

and

$$I_t = I_d e^{-\mu t} \tag{3.2}$$

Where:

I_t -- true count rate for transmitted beam
I_o -- observed count rate for transmitted beam
I_d -- true count rate for direct beam
$I_{o,d}$- observed count rate for direct beam
μ_t -- true absorption factor
μ_o -- apparent absorption factor

At low direct beam counting rates the relation $I_t = I_o$ holds, and a constant value is obtained for the absorption factor of the foil. As the counting rate is increased, at some point the detector responds nonlinearly and the apparent absorption factor starts to change, i.e. the condition that $I_t = I_o$ no longer holds for the direct beam but still holds for the transmitted beam, i.e.,

$$I_t = I_o \tag{3.3}$$

but

$$I_d \neq I_{o,d} \tag{3.4}$$

Eliminating I_t and I_o from equations (3.1), (3.2) and (3.3), we can obtain

$$I_d = I_{o,d} e^{(\mu_t - \mu_o)} \tag{3.5}$$

After rearranging and divided by $I_{o,d}$, we have

$$(I_d - I_{o,d})/I_{o,d} = e^{(\mu_t - \mu_o)} - 1 \tag{3.6}$$

Since $I_d-I_{o,d}$ is the correction to be applied to the observed direct beam counting rate, equation (3.6) is simply the fraction of this correction. A percentage correction graph can be obtained by plotting $100(I_d-I_{o,d})/I_{o,d}$ vs $I_{o,d}$.

Proportional channel This channel was tested under the following conditions: (a) detector operating voltage at 1000 volts, (b) filling gas (P-10) pressure at 1 psi and (c) photon energy ~7 KeV from a Ge(311) crystal. Measurements took place on two different metal foils, zirconium and copper. Various numbers of X-ray photons were obtained by applying different tube current. The experimental results are shown in Table B-5.

It is evident from a cursory examination of the data in Table B-5 that the detector started to depart from linearity at a counting rate in the range of approximately $2.4-4.8*10^4$ cps. One can also observed this onset in nonlinearity on the graphs which were obtained by plotting $\ln I_{o,d}$ vs μ_o for both Cu and Zr foils (see Fig. B-12). These two curves showed an agreement in nonlinearity which occurred within the range mentioned above. The true absorption factor μ_t was calculated by taking the average value of the first eleven μ_o's which were measured at different tube currents ranging from 2 to 12 mA. They are 1.1328 and 3.0664 for Cu and Zr, respectively. The amount of departure from linearity can be calculated from the difference between μ_o and μ_t. The amount of corrections

Table B-5. The results of absorption-factor method for the proportional counting channel

tube current	$I_{o,d}$	Cu foil I_o	Cu foil $\ln(I_{o,d}/I_o)$ (μ_o)	Zr foil I_o	Zr foil $\ln(I_{o,d}/I_o)$ (μ_o)
1mA	774	251	1.1261	40	2.9627
2mA	2478	794	1.1381	119	3.0360
3mA	4141	1329	1.1365	196	3.0506
4mA	5827	1884	1.1291	274	3.0571
5mA	7513	2422	1.1320	352	3.0608
6mA	9220	2960	1.1362	430	3.0653
7mA	10873	3470	1.1421	505	3.0695
8mA	12500	4006	1.1380	569	3.0896
9mA	14121	4592	1.1234	642	3.0908
10mA	15807	5131	1.1252	725	3.0820
11mA	17442	5654	1.1265	804	3.0770
12mA	19129	6156	1.1338	896	3.0610
15mA	24101	7774	1.1315	1133	3.0574
30mA	48048	15904	1.1056	2327	3.0276
60mA	94064	32330	1.0680	4708	2.9947
90mA	135550	47994	1.0382	7054	2.9557

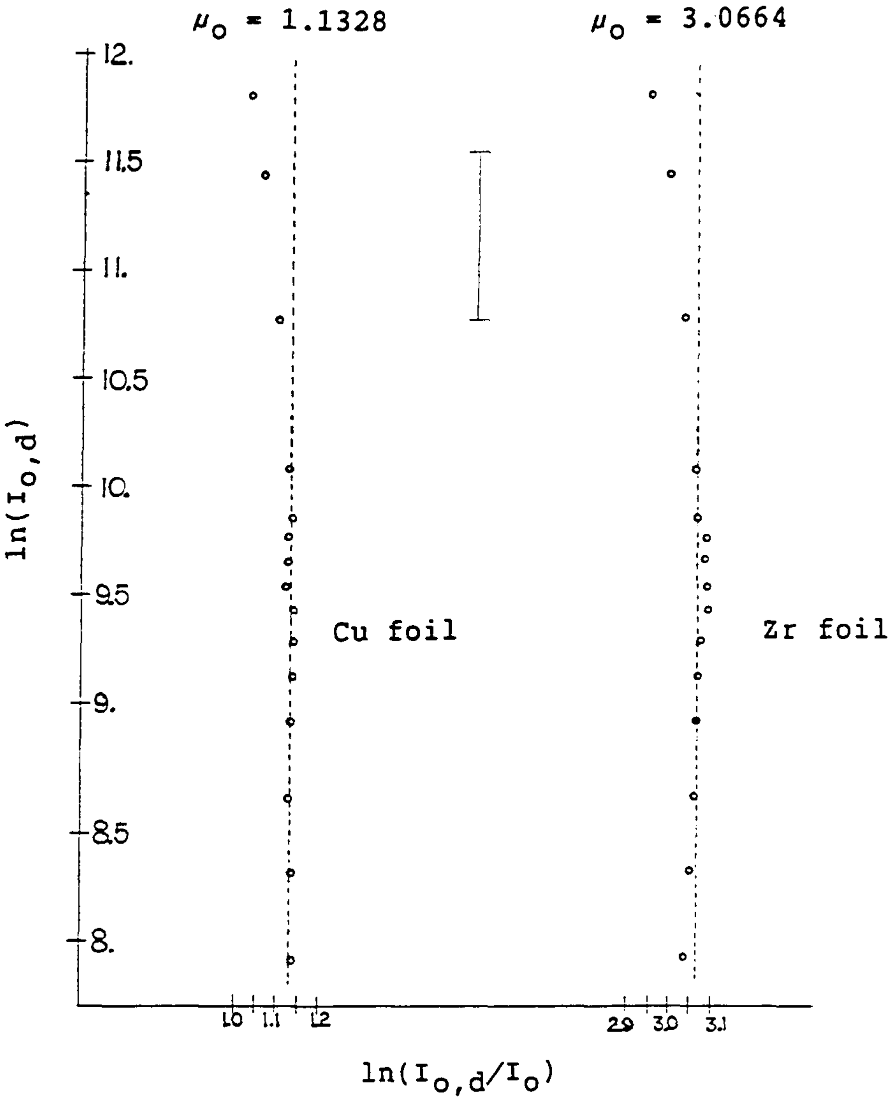

Fig. B-12 Absorption factor method: Apparent absorption factor (μ_o) vs. $\ln I_{o,d}$ (proportional counter). See text for detail

$I_{o,d}$	$\mu_t-\mu_o$		$100\%*(I_d-I_{o,d})/I_{o,d}$	
	Cu	Zr	Cu	Zr
14121	0.0094	--	0.94%	--
15807	0.0076	--	0.76%	--
17442	0.0073	--	0.73%	--
19129	--	0.0054	--	0.54%
24101	0.0013	0.0090	0.13%	0.90%
48048	0.0272	0.0388	2.76%	3.95%
94064	0.0648	0.0679	6.69%	7.03%
135550	0.0946	0.1107	9.92%	11.71%

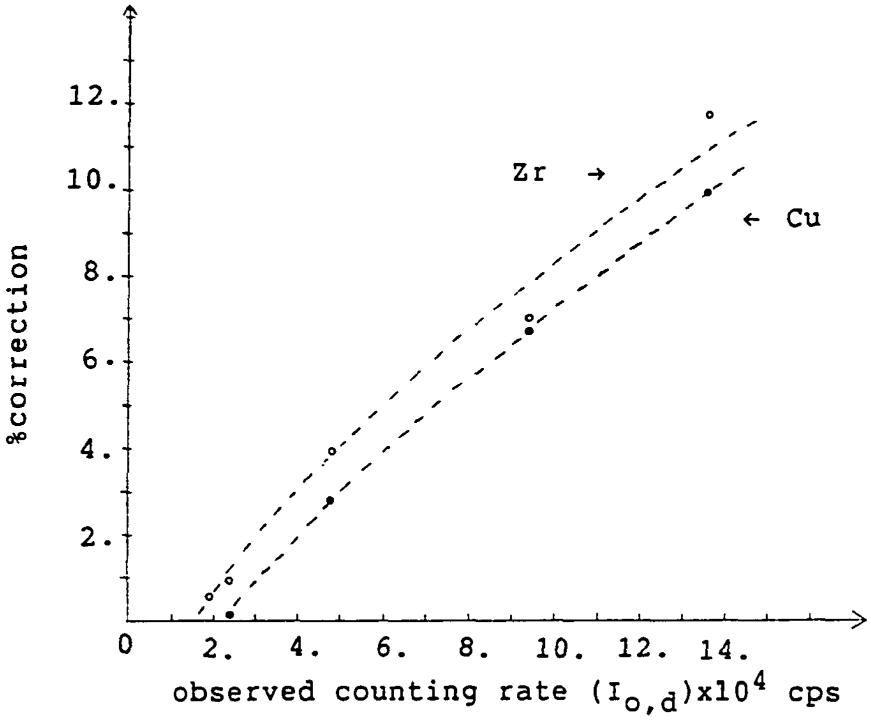

Fig. B-13 Correction curves for proportional counter. See text for detail to be made and the two corresponding correction curves are shown in Fig. B-13.

Since the experimental conditions for both samples were the same, it was expected that the same correction should be obtained for a specific counting rate. It is true that the two curves in Fig. B-13 are very close to each other. Comparing these correction curves, one can see that the results obtained from the Zr sample were very poor since the standard deviation associated with each point was large. This large standard deviation was perhaps due to the fact that Zr sample absorbed so much (~90%) that it leads to the introduction of serious statistical inaccuracies in measuring the transmitted beam. It would be better to use a sample which only absorbs a reasonable fraction, say 1/2 to 2/3, of the incident radiation. Cu absorbed less than 3/4 of the beam, and gave a better result than Zr.

Scintillation channel This channel was tested under the conditions of: (a) detector operating voltage at 1500 KV and (b) photon energy at 7 KeV from a Ge(311) monochromating crystal. The foil used was a piece of standard manganese oxide filter. Experimental data are shown in Table B-6 and Fig. B-14.

It can be seen in this figure that the values of the absorption coefficients which were obtained at counting rates less than 10^5 cps spread around $\mu_0 = 0.8440$ with a standard

Table B-6. Results of absorption-factor method for the scintillation counting channel[a]

$I_{o,d}$	I_o	$\ln(I_{o,d}/I_o)$
1962	820	0.87242
3908	1675	0.84721
5944	2763	0.76607
7950	3463	0.83104
10251	4578	0.80611
12833	5530	0.84183
15886	7302	0.77729
18543	8501	0.77991
24187	11735	0.72324
30710	12562	0.89391
35945	15806	0.82160
45354	18681	0.88699
56688	22181	0.93883
65528	26755	0.89576
73197	30037	0.89073
81225	33135	0.89663
89303	37084	0.87885
98186	43459	0.81505
107377	47894	0.80736
115570	51556	0.80721
123894	57450	0.76924
130843	61899	0.74849
137413	65524	0.74057
144430	68170	0.75079
153197	75083	0.71313
162753	81556	0.69094
170413	82258	0.72836
178472	89734	0.68758
187322	97629	0.65165
195966	99750	0.67527
202336	103495	0.67041
217525	116123	0.62766
226592	122951	0.61137
233098	126499	0.61122
241640	136163	0.57360
250700	141848	0.56950
258415	145649	0.57337

[a] A single channel analyzer was included in the counting system when this test was performed.

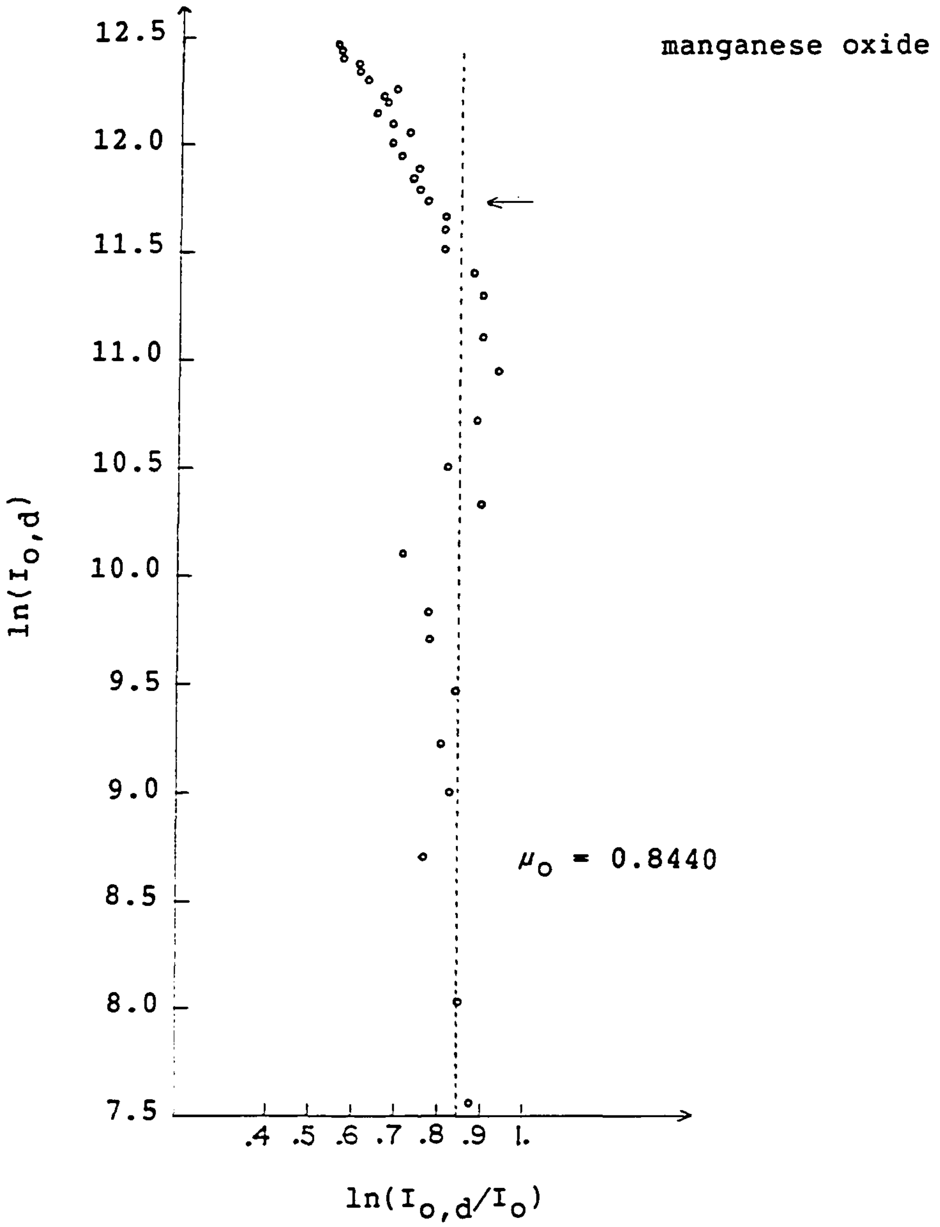

Fig. B-14 Absorption factor method: Apparent absorption factor (μ_o) vs. $\ln I_{o,d}$ (scintillation counter). See text for detail deviation of 0.06. Nonetheless, it is quite obvious that the detector started to depart from linearity at counting rate about 1.25×10^5 cps (see arrow sign marked in the figure).

Energy Resolution

Two types of single crystals, Ge and Si, are currently used on the EXAF-3 spectrometer. The allowed 2θ angle on the spectrometer is mechanically restricted to the range of 48° - 144°. Their interplanar spacings and detectable energy ranges are listed in Table B-7.

The two crystals, Ge(311) and Si(400), were tentatively used in the investigation of the energy resolution of the spectrometer. These two crystals were carefully bent using a procedure described in the "Alignment" section. A second level of alignment for both crystals could usually result in high diffracting power with energy resolution better than 25 eV at ~7.4 KeV. Two examples are shown in Fig. B-15.

Better energy resolutions can be achieved by a further adjustment of the angular position of the crystal without too much loss in the diffraction power. This adjustment employs steps (7), (8) and (9) in the second level alignment (refer to page 188) except that the Oreil stage must now be driven to the ends of the desired energy range instead of driven to the extreme ends of the angle limit. Using this method, the energy resolution could be improved to be less than 18 eV with

Table B-7. Interplanar spacings and effective energy ranges for five different crystals

Crystal	d spacing (Å)	E^a (KeV) (long beam line)[b]	E (KeV) (short beam line)[c]
Si(111)	3.1353	2.68 - 4.80	5.10 - 6.33
Ge(311)	1.7060	4.93 - 8.81	9.38 - 11.63
Si(400)	1.3576	6.19 - 11.07	11.79 - 14.61
Si(511)	1.0452	8.04 - 14.38	15.31 - 18.98
Si(840)	0.6072	13.85 - 24.75	26.35 - 32.67

[a] The energy is obtained from the equation E =12.4 x R/(Ld), where R is the Rowland circle radius, L is the source-to-crystal distance and d is the interplanar spacing of the crystal.

[b] The energy range is obtained when the long beam-line is used. This beam-line allows the source-to-crystal distance to change within the range of 16.5 cm - 29.5 cm.

[c] The energy range is obtained when the short beam-line is used. This beam-line allows the source-to-crystal distance to change within the range of 12.5 cm - 15.5 cm.

Fig. B-15 The tungsten L_1 excitation line in the first order of reflection with Ge(311): (a) The curve denoted by "A" is obtained using the signals from the scintillation counter, (b) The curve denoted by "A" is obtained using the signals from the scintillation counter and the curve denoted by "B" is obtained using the signals from the proportional counter. The numbers on top of the curves are the intensities of A and B, respectively. In both (a) and (b), the numbers shown underneath the curves are energies in the unit of eV.

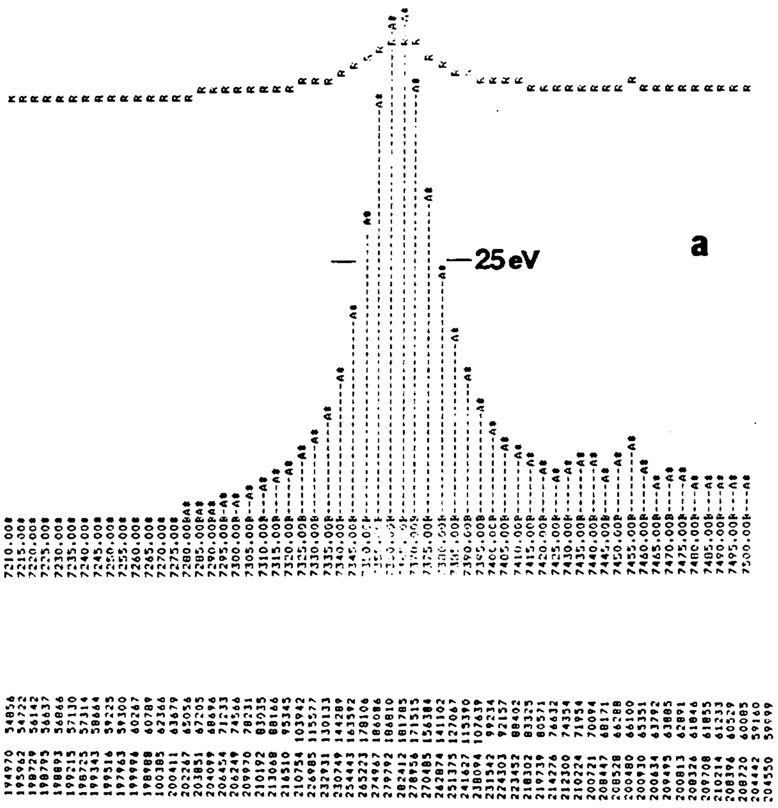
a
25eV

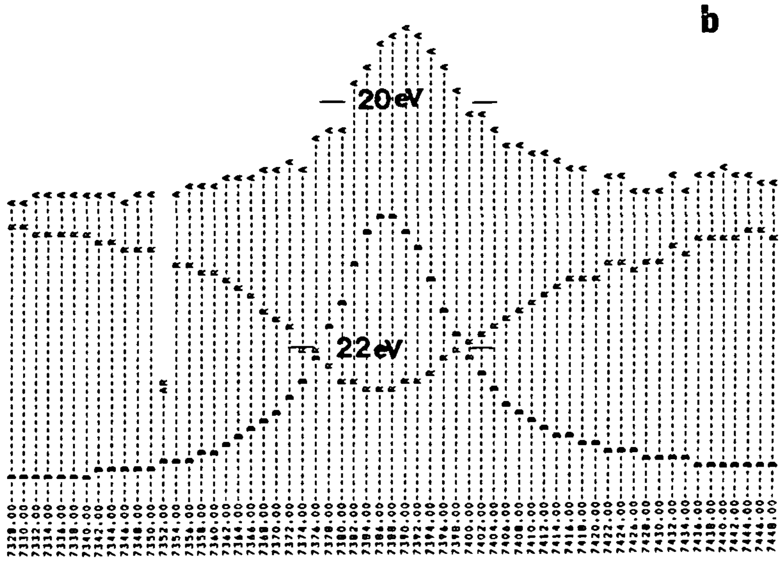
b
20eV
22eV

Fig. B-16 Energy resolutions improved by a further adjustment of the angular position of the crystal (proportional counter): (a) Tungsten L_1 excitation line in the first order of reflection with Ge(311). The numbers on the bottom of the curve are energies in the unit of eV. (b) Tungsten $L\alpha_1$ excitation line in the first order of reflection with Si(400). The numbers underneath the curve are the intensity (integer) and the source-to-crystal distance (in 0.1 mm).

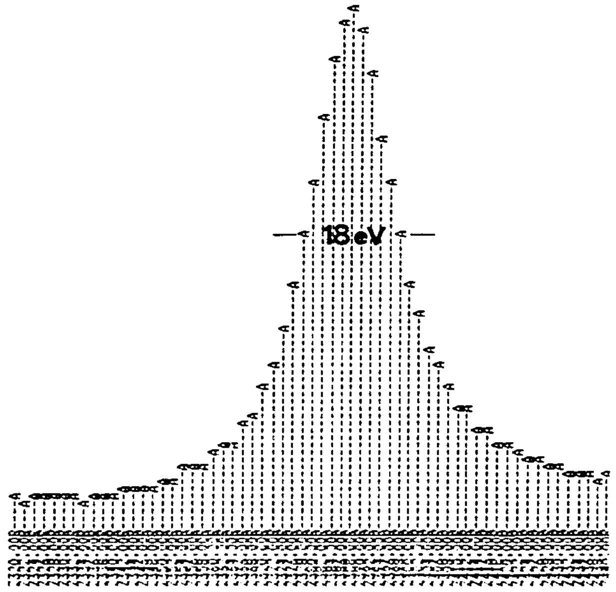

a

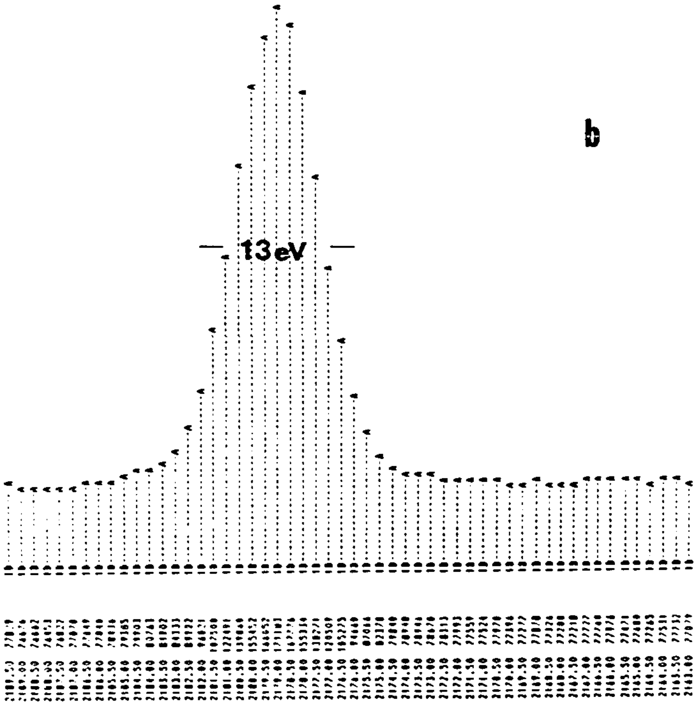

b

Ge(311) crystal at 7 KeV and 13 eV with Si(400) crystal at 8.4 KeV. These are shown in Fig. B-16.

The highest energy resolutions may be achieved by using the higher order reflection with a crystal of larger interplanar distance. For example, the fourth order of reflection with a Si(111) crystal may give better than 5 eV of energy resolution at 8 KeV.[36] However, the scattering power of this higher order reflection is so weak that it is not very useful in the EXAFS measurements.

Maximum diffraction power and energy resolution cannot be obtained simultaneously. Two rocking curves of a Si(400) crystal were measured at the position of $L\alpha_1$ characteristic line of the tungsten anode and were used to look into the differences in diffraction power and the resolution from this crystal whose angular position was tuned at different energies. The data and plots of the curves are shown in Table B-8 and Fig. B-17, respectively. The zero point of the θ angle in this figure is arbitrarily chosen on the high energy side of the tungsten $L\alpha_1$ line. The positions of Bragg angle for the two rocking curves are identical and are not shown in the figure.

By examining these two curves, it can be seen that curve (b) has a better energy resolution (0.05° vs. 0.032° or 7 eV vs. 11 eV) while curve (a) shows higher diffraction power (peak height ratio is 2:1). This suggests that for EXAFS measurements which do not require too much resolution, the

Table B-8. The diffraction power as a function of θ of a Si(400) monochromating crystal tuned at different energies

tuned at ~7.7 KeV (curve a)		tuned at ~6.9 KeV (curve b)	
θ[a](°)	Intensity (x10^3)	θ(°)[a]	Intensity (x10^3)
0.000	10.0	0.000	3.5
0.012	13.7	0.008	4.2
0.016	29.5	0.012	13.3
0.020	60.5	0.0176	38.3
0.024	83.7	0.020	46.3
0.028	95.4	0.024	50.3
0.032	100.0	0.028	49.0
0.036	101.0	0.0336	44.0
0.040	97.0	0.036	35.7
0.044	88.5	0.040	31.5
0.048	79.0	0.048	26.2
0.056	60.0	0.056	23.2
0.064	53.0	0.064	18.3
0.072	47.6	0.080	5.4
0.080	44.0	0.096	3.8
0.096	36.7	0.112	3.8
0.112	30.5		
0.128	23.0		
0.144	11.7		

[a] The zero point of this θ angle is arbitrarily chosen on the high energy side of the tungsten Lα$_1$ line.

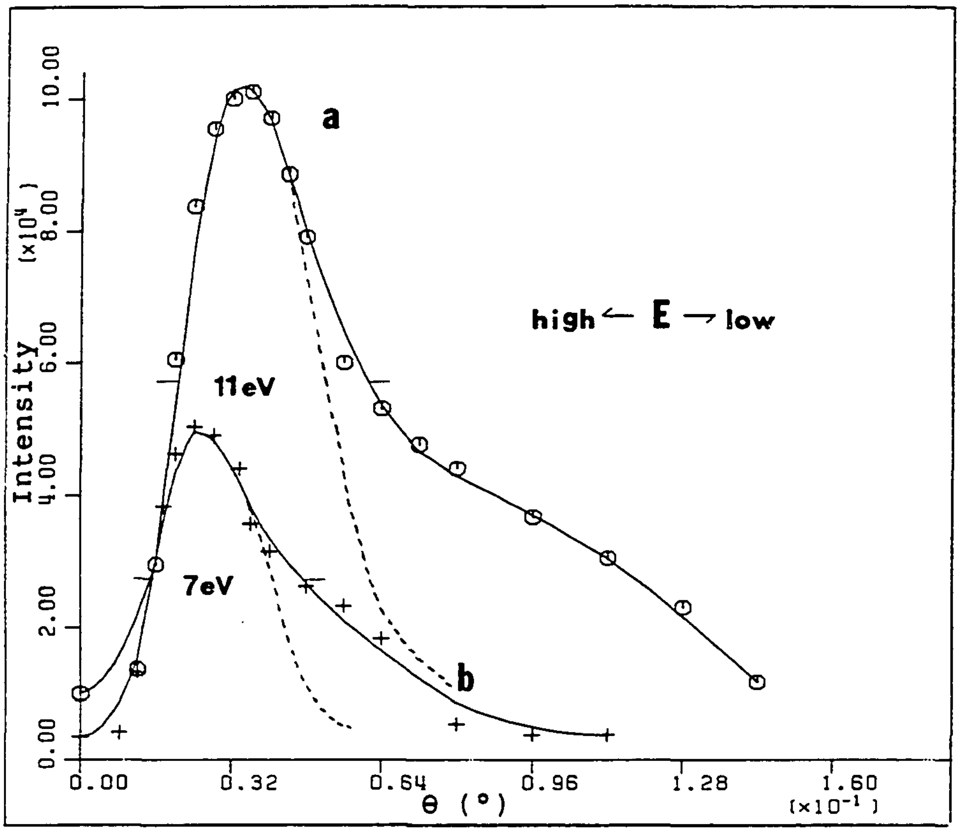

Fig. B-17 Rocking curves measured at tungsten Lα_1 excitation line (~8.4 KeV). See text for detail monochromating crystal should be aligned to give maximum diffraction power. However, when a high energy resolution measurement is required, for instance for edge structures, the monochromating crystal should be carefully aligned at an extremely high angle side.

It may be noticed that the profiles of the two curves in Fig. B-17 were broadened on the right side (low energy side). This is due to near-surface strains which was introduced into the silicon crystal in the bending process. The normal Bragg scattering profiles are indicated by the dashed curves.

Data Acquisition Software

A program package, ALEXS, has been designed to operate the EXAF-3 EXAFS spectrometer. This package contains a main program, ALEXS, and 22 subroutines. In the first part of ALEXS, three major pieces of information are requested: monochromator code (there are five different crystals), type of the beam line (two beam lines are available, one is short and one is long) and the current spectrometer setting (where the crystal is at in terms of source-to-crystal distance). In the second part of ALEXS, it sets up all the instrumental constants and initializes parameters. In the last part, ALEXS provides five different options--alignment, spectrometer calibration, detector linearity test, resolution measurement, and data collection (these subjects are not necessarily selected in sequence). After a particular option has completed excution, ALEXS will restart the third part so that the user can repeat the same subject or proceed to another.

Every option is composed of several subroutine calls. Among the 22 subroutines, XFSCOM is the only one which directly communicates with LSI-11 computer and in turn controls the spectrometer and counting systems. Therefore, when a certain type of spectrometer action is requested, an XFSCOM call is always made. Brief descriptions of some major subroutines are given below.

ALIGN This routine is designed for fine adjustment in alignment and "tuning" resolutions of the spectrometer. It may be used under the following conditions: (a) To perform standard alignment, (b) to check the focusing condition each time after the anode has been replaced, (c) to switch monochromators, (d) to recheck alignment after changing receiving slits and (e) to tune to obtain maximum energy resolution.

RXCAN This routine is useful whenever a scan in steps of 2θ angle(or distance) is needed. The primary usage of the routine is to calibrate the distance setting of the spectrometer.

EMLSN This routine provides characteristic line information for tungsten X-ray radiation. This is useful for calibrating the spectrometer, measuring the energy resolution and selecting an appropriate scan range.

SEREM This routine searches for emission lines that fall in a specified energy range and prints out their energies and corresponding monochromator positions. It also sets up default values of the energy ranges for scans over a certain emission line.

LNRTST This routine is designed for the purpose of testing the upper limit of detector linearity and determining the counting correction for a detector running in a nonlinear condition. It is useful when the detection system is replaced or modified and no established data are available. Procedures of performing the absorption factor method are provided in the routine.

THICK In this routine the user has to supply the atomic number of the absorbing atom in the system. It will do a quick scan over the edge region to estimate the value of μt of the sample. It is very useful in selecting appropriate samples to give good EXAFS spectra.

EDGEE This subroutine stores both empirical and theoretical threshold energy information for 84 elements with atomic numbers ranging from 17 to 100. For elements of Z from 20 to 45 only K-edge energies are stored. Elements of Z from 46 to 50 are provided with both K-edge and L_{III}-edge energies. For elements of Z from 51 to 100 only L_{III}-edge energies are provided.

COUNTING This routine takes care of both preset-time and preset-count counting. In the preset-time counting mode, an XFSCOM (64) call is made. A real time clock having a resolution of 1/60 second is utilized to monitor the "time". In preset-count counting mode, an XFSCOM (512) call is used. The total count which is going to be accumulated on the counter(s) can not be set automatically by the computer, but via a manual switch on the B counter control panel. Counter B can also be used as a clock with a resolution of one thousandth of a second. The most important feature of this routine is that it monitors the detector's count rate and automatically adjusts the beam slit width.[37]

EXCAN This routine is utilized to make scans in a unit of energy (eV). Scan range and step size in units of eV must be input and the computer calculates the corresponding monochromator steps and then moves the ϕ shaft.

EXFDATA This is an essential data collection routine. Multiple scan ranges with different step size can be specified. EXAFS measurements can be made by means of two methods,[38] one is called a direct method and the other is called a ratio method. In the direct method, only one detector is used, the EXAFS spectrum being obtained from two scans over the same energy range. In the ratio method, both the scintillation and proportional detectors are required and only one scan is performed.

Data Reduction

Programs which includes three major subroutines, EXA, EXB, and EXC, for EXAFS data reduction have been developed. EXA is a polynomial least-squares fitting routine which does a least-squares fit to the pre-edge spectrum, extrapolation to post edge and the subtraction of the resulting non-K edge background absorption in E space. EXB is a smoothing subroutine which includes a smoothing procedure using either a five-point averaging method[39] or a cubic-spline function[40] to calculate values of μ_0's in E space. EXC converts the EXAFS signal χ in E space into the momentum κ space. An example of the pre-edge background fitting using the program EXA is shown in Fig. B-18. This X-ray absorption spectrum was measured at the manganese edge in a manganese oxide sample. In (a), the pre-edge background was obtained by fitting the pre-edge spectrum and extrapolating to the post-edge with Victoreen's function.[41] The resulting absorption spectrum which is free of non-K edge background is shown in (b).

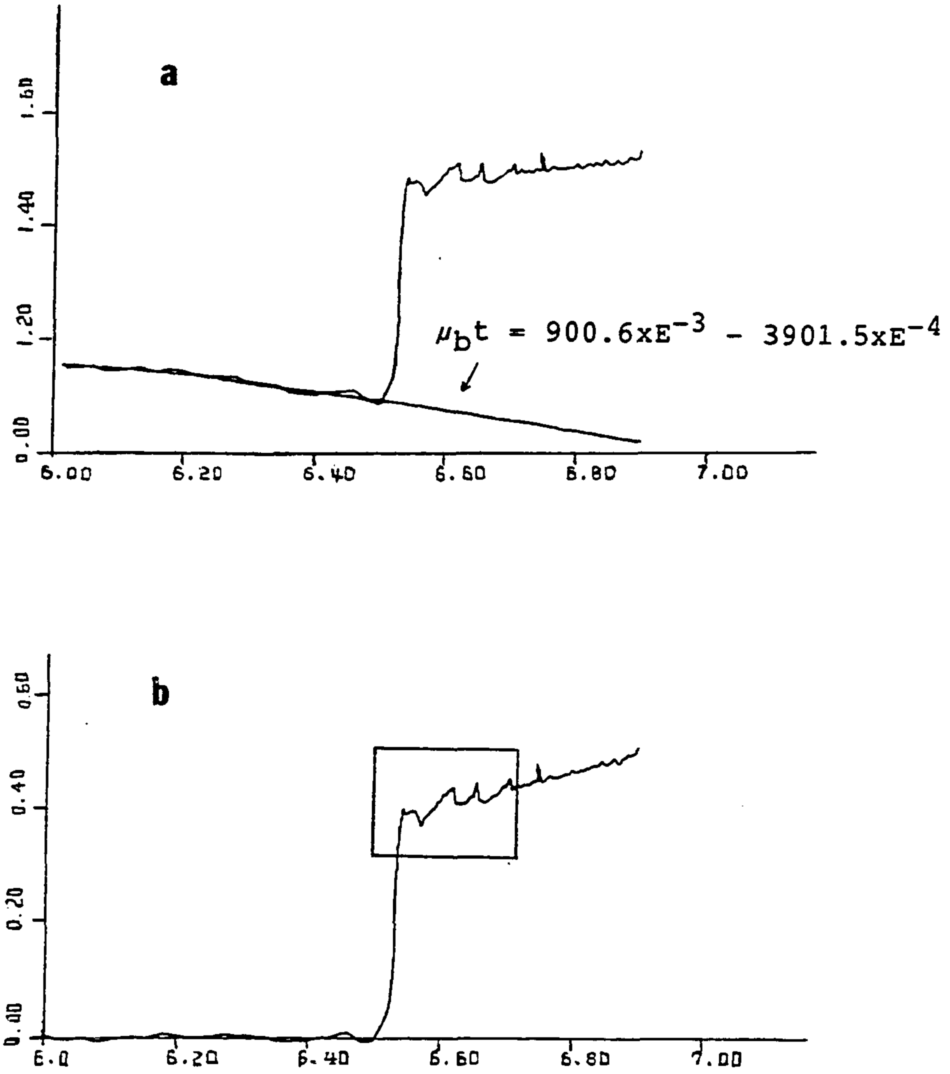

Fig. B-18 Background subtraction using Victoreen's function in a manganese EXAFS spectrum. See text for detail

CHAPTER 4. SUMMARY

The development of our in-lab EXAFS facility has been almost completed. The spectrometer is well aligned on the stage of the GX-21 rotating anode X-ray generator. Finer adjustment in the alignment can be routinely done with the help of the computer program "ALIGN". The computer software for interfacing the EXAF-3 spectrometer to the LSI-11/03 microcomputer has been developed and successfully tested. It includes the controlling of an ORTEC dual A/B counter and three shafts which in turn govern the beam slit, the monochromator (along with the sample stage and detectors) and a sample disk[42] on the spectrometer. The A and B counters process signals from the scintillation detector and the proportional counter, respectively.

The vital and most complicated parts of the EXAFS facility are the detectors and their electronic systems. Their performances have been tested. Typical photon flux of 2×10^6 cps can be obtained by using a bent silicon crystal (see Table B-4). In EXAFS measurements, both the I_o and I_1 detectors are supposed to absorb about 15% of these X-ray photons,[43] i.e. 3×10^5 cps. But, both the scintillation and proportional detectors can only respond linearly to no more than 1×10^5 cps. The counting loss may be corrected by a calibration curve as shown in Fig. B-13, but this means cannot always provide a correction which is accurate enough to avoid distorting the data. The response of the detection systems can be significantly slowed down by the use of shaping circuitries which are imposed on the systems for the purpose of energy discrimination. For example, the scintillation counter could respond linearly at least to $2x10^5$ cps (refer to Table B-4b) before a single channel analyzer was added to the counting channel.

Although the energy resolution requirement for EXAFS measurements are not too severe, it is still necessary to have a reasonably high resolution to get useful EXAFS signals. At the present time, the energy resolution less than 13 eV (experimental value) at 8.4 KeV can be obtained from our EXAF-3 spectrometer with a bent silicon crystal. This resolution can be further improved by employing crystals which are thinner and are as perfect as possible.[44]

The computer programs for data acquisition and data reduction have been written using FORTRAN 77 computer language. Owing to the presence of strong characteristic lines in the X-ray spectrum of the tungsten anode, many efforts were devoted to solve this problem in the data collection scheme. EXAFS spectra of only a few elements (see Fig. B-19) will not be contaminated by tungsten lines when measured on our EXAF-3 spectrometer.

A few manganese EXAFS spectra have been measured on the EXAF-3 spectrometer and one of them is shown in Fig. B-18. This spectrum was measured using the direct method (sample-in

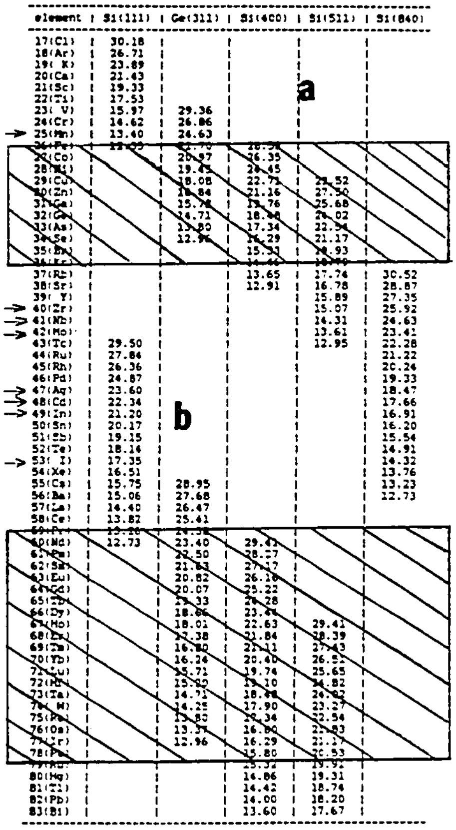

element	Si(111)	Ge(311)	Si(400)	Si(511)	Si(840)
17(Cl)	30.18				
18(Ar)	26.71				
19(K)	23.89				
20(Ca)	21.43				
21(Sc)	19.33				
22(Ti)	17.53				
23(V)	15.97	29.36			
24(Cr)	14.62	26.86			
→ 25(Mn)	13.40	24.63			
26(Fe)	[illegible]	[illegible]	[illegible]		
27(Co)		20.97	26.35		
28(Ni)		19.45	24.45		
29(Cu)		18.08	22.71	29.52	
30(Zn)		16.84	21.16	27.50	
31(Ga)		15.78	19.76	25.68	
32(Ge)		14.71	18.48	24.02	
33(As)		13.80	17.34	22.54	
34(Se)		12.96	16.29	21.17	
35(Br)			15.33	19.93	
36(Kr)			14.46	[illegible]	
37(Rb)			13.65	17.74	30.52
38(Sr)			12.91	16.78	28.87
39(Y)				15.89	27.35
→ 40(Zr)				15.07	25.92
→ 41(Nb)				14.31	24.63
→ 42(Mo)				13.61	23.41
43(Tc)	29.50			12.95	22.28
44(Ru)	27.84				21.22
45(Rh)	26.36				20.24
46(Pd)	24.87				19.33
→ 47(Ag)	23.60				18.47
→ 48(Cd)	22.34				17.66
→ 49(In)	21.20				16.91
50(Sn)	20.17				16.20
51(Sb)	19.15				15.54
52(Te)	18.16				14.91
→ 53(I)	17.35				14.32
54(Xe)	16.51				13.76
55(Cs)	15.75	28.95			13.23
56(Ba)	15.06	27.68			12.73
57(La)	14.40	26.47			
58(Ce)	13.82	25.41			
59(Pr)	[illegible]	[illegible]			
60(Nd)	12.73	23.40	29.41		
61(Pm)		22.50	28.27		
62(Sm)		21.63	27.17		
63(Eu)		20.82	26.16		
64(Gd)		20.07	25.22		
65(Tb)		19.33	24.28		
66(Dy)		18.66	[illegible]		
67(Ho)		18.01	22.63	29.41	
68(Er)		17.38	21.84	28.39	
69(Tm)		16.80	21.11	27.43	
70(Yb)		16.24	20.40	26.52	
71(Lu)		15.71	19.74	25.65	
72(Hf)		15.20	19.10	24.82	
73(Ta)		14.71	18.48	24.02	
74(W)		14.25	17.90	23.27	
75(Re)		13.80	17.34	22.54	
76(Os)		13.37	16.80	21.83	
77(Ir)		12.96	16.29	21.17	
78(Pt)			15.80	20.53	
79(Au)			15.32	19.92	
80(Hg)			14.86	19.31	
81(Tl)			14.42	18.74	
82(Pb)			14.00	18.20	
83(Bi)			13.60	17.67	

Fig. B-19 Lists of elements which are measuable on EXAF-3 spectrometer: (a) K-edge, (b) L_{III}-edge. The numbers in the columns are source-to-crystal distances. Elements designated by an arrow sign are those which can be free of tungsten lines in their EXAFS spectra. Hatched zones represent elements whose EXAFS spectra can be severely contaminated by tungsten lines.

and sample-out mode). Although most of the edge features which occur within the first 250 eV after the absorption edge (refer to the partial spectrum outlined in a box in Fig. B-18b) are correct, the general trend of the absorption spectrum was not quite right. Instead of the decreasing in absorption coefficient with increasing in energy, the spectrum slightly increasing. No explanation can be advanced thusfar except that doubts have been associated with the correct operation of the detectors. Once the problems associated with the detectors as well as the harmonics can be conquered, our EXAFS system should be able to produce reliable and useful absorption spectra.

REFERENCE

1. E. A. Stern, Phys. Rev. B10, 3027 (1974).
2. D. E. Sayers, E. A. Stern, F. Lytle, Phys. Rev. Lett. 27, 104 (1971).
3. E. A. Stern, ed., "Laboratory EXAFS Facilities-1980," Am. Inst. Phys., New York, 1980.
4. P. A. Lee, P. H. Citrin, P. E. Eisenberger and B. M. Kincaid, Rev. Modern Phys. 53, 769 (1981).
5. K. O. Hodgson, B. Hedam and J. E. Penner-Hahn, ed., "EXAFS and Near Edge Structure III" (Springer-Verlag, New York, 1984).
6. C. A. Ashley and S. Doniach, Phys. Rev. B11, 1279 (1975).
7. P. A. Lee, Phys. Rev. B13, 5261 (1976).
8. B. K. Teo and D. C. Joy, "EXAFS Spectroscopy: Techniques and Applications" (Plenum Press, New York, 1981).
9. P. A. Lee and J. B. Pendry, Phys. Rev. B11, 2795 (1975).
10. F. W. Lytle, D. E. Sayers and E. A. Stern, Phys. Rev. B12, 4825 (1975).
11. J. A. Del Cueto and N. J. Schevchik, J. Phy. C11, 1833 (1978).
12. S. P. Cramer and R. A. Scott, Rev. Sci. Instrum. 53, 395 (1981).
13. J. Stohr, Jpn. J. Appl. Phys. 17, Suppl. 17-2, 217 (1978).
14. E. A. Stern, D. E. Sayers, and F. W. Lytle, Phys.Rev. B11, 4836 (1976).
15. B. K. Teo, Acc. Chem. Res. 13, 412 (1980).
16. S. P. Cramer, T. K. Eccles, F. Kutzler, K. O. Hodgson and S. Doniach, J. Am. Chem. Soc. 98, 8059 (1978).
17. S. P. Cramer, K. O. Hodgson, E. I. Stiefel and W. E. Newton, J. Am. Chem. Soc. 98, 2748 (1978).

18. B. K. Teo and P. A. Lee, J. Am. Chem. Soc. 99, 2815 (1979).

19. G. S. Brown, P. Eisenberger, and P. Schmidt, Solid State Commun. 24, 201 (1977).

20. E. A. Stern and K. Lu, Nuclear Instrum. Method, 195, 415 (1982).

21. The characteristic line problem can also be eliminated by using detectors which are highly linear over a wide dynamic-range such as ionization chambers. Also see reference 20.

22. G. S. Knapp, Haydn Chen, and T. E. Klippert, Rev. Sci. Instrum. 49, 1658 (1978).

23. S. Khalid, R. Emrich, R. Dujari, J. Shultz and J. R. Katzer, Rev. Sci. Instrum. 53, 22 (1982).

24. P. Georgopoulos and G. S. Knapp, J. Appl. Crystallogr. 14, 3 (1981).

25. G. G. Eichholz and J. W. Poston, "Principles of Nuclear Radiation Detection" (Ann Arbor Science Publishers, Inc., 1979).

26. F. Comin, L. Incoccia and S. Mobilio, J. Phys. E. Sci. Instrum. 10, 83 (1983).

27. J. A. Del Cueto and N. J. Chevchik, J. Phys. E: Sci. Instrum. 11, 616 (1978).

28. G. G. Cohen, D. A. Fisher, J. Corbert, N. J. Shevchik, Rev. Sci. Instrum. 51, 273 (1980).

29. (a) A. Williams, Rev. Sci. Instrum. 54, 193 (1983).

(b) W. Thulke, R. Haensel, and P. Rabe, Rev. Sci. Instrum. 54, 277 (1983).

(c) K. Tohji and Y. Udagawa, Rev. Sci. Instrum. 54, 1482 (1983).

30. One may look into the crystal to find the shape of the eyes for judging the radius.

31. The slit is installed on the X-ray window for the control of beam intensity.

32. The motor interrupt was not able to be used due to malfunction occurred in the GE interface.

33. M. A. Short, 1966, Proc. 5th Conference on X-ray Analytical Methods.

34. M. A. Short, Rev. Sci. Instrum. 31, 618 (1960).

35. P. R. Bevington, "Data Reduction and Error Analysis for the Physical Sciences" (New York, McGraw-Hill, 1969).

36. A. A. Bahgat and K. D. Gupta, Rev. Sci. Instrum. 50, 1020 (1979).

37. This adjustment is not desirable since the energy resolution might be changed. But, before the access of automatic control of tube-current is obtained, the beam slit is needed to cut down the strong intensities of the tungsten lines.

38. The ratio method is better than the direct method if the two detectors used for detecting I_0 and I_1 are linear.

39. P. Marchand and L. Marmet, Rev. Sci. Instrum. 54, 1034 (1983).

40. J. H. Ahlberg, E. N. Nilson, and J. L. Walsh, "The theory of Splines and Their Applications" (Academic, New York, 1967).

41. International Tables for X-ray Crystallography III. edited by K. Lonsdale et al. (Kynoch, Birmingham, England, 1962), Sec. 3.2.

42. The sample disk is designed and made so that it could be installed either in front of the first detector (usually the proportional counter) or between the I_0 and I_1 detectors. Appropriate filters can be mounted on the disk to cut down X-ray flux either before or after the I_0 detector. This disk is also employed whenever the direct mehtod is used to obtain the absorption spectrum.

43. The sample should absorb ~90% of the incident beam, I_{in} (refered to Fig. B-1).

44. R. Jenkins and J. L. de Vries, "Practical X-ray Spectrometry" (N. V. Philips' Gloeilampenfabrieken, The Netherlands, 1967).

SUMMARY

In the first part of this thesis, a hybrid approach which combines both Patterson-superposition techniques and direct methods has been developed and discussed. The basic theory of this hybrid approach as well as the probability theory of the triple-phase structure invariants in which the pseudo-normalized structure factors G participate have been derived. The validity of the Σ_2-like relation was proven to be very effective in both centrosymmetric and noncentrosymmetric structures and the use of this relation in real structure solutions were also very successful.

In the second part of this thesis, an in-lab EXAFS technique which utilizes a rotating anode X-ray source has been described and discussed. The EXAF-3 EXAFS spectrometer has been successfully aligned and automated. Interface software which was developed on a LSI-11/03 microcomputer using PDP-11 machine language were outlined. Both energy resolution and performance of the current detection systems were carefully investigated and presented in detail. Softwares for data acquisition and data reduction which were developed on VAX-11/730 and VAX-11/780 computers, respectively, using FORTRAN 77 language, were also briefly described.

ACKNOWLEDGEMENTS

I am grateful to Dr. Robert A. Jacobson for his guidance through the course of this work. His patience and understanding during my graduate years have been a constant source of encouragement.

I would like to thank James Richardson, Lance Miller, and Sangsoo Kim for the discussion and the exchange of ideas on both crystallography and computer programming.

I also want to thank Brenda Smith, Barb Helland, Marlene Frisk and Jim Benson for their companionship and assistance. They have made this place warmer and amiable.

I wish to thank Bill Thomas and Harold Skank for their assistance in the interface and detector electronics.

Special thanks are due to Judy Spencer and Lance Miller for their memorable friendship. I speak better English due to a lot of "chatting" with them, plus their patient corrections.

I am indebted to my mother and sister for their infinite love and support. I wish to dedicate this dissertation to my past father and brother. They loved me so much.

The most thanks and appreciation should go to my dear and wise husband, Kwang-Hwa. He has made my life full of intellect, adventure, and happiness.